DSPACE

https://dspace.org/

Synthesis and the investigation of structural, electronic and magnetic properties of and c

Magoda, Nyawasedza

2022
https://hdl.handle.net/10539/36975

Downloaded from a DSpace repository. https://dspace.org/

UNIVERSITY OF THE WITWATERSRAND, JOHANNESBURG



Synthesis and the Investigation of Structural, Electronic and Magnetic Properties of $RuFe_3Si$ and $RhFe_3C$

Nyawasedza Magoda

A dissertation submitted to the Faculty of Science, University of the Witwatersrand, Johannesburg, in fulfilment of the requirements for the degree of Master of Science

Johannesburg

August 2022

Declaration

The experiments described in this dissertation were performed at the University of the Witwatersrand with the exception of high temperature vibrating sample magnetometer measurements which were performed at Saha Institute of Nuclear Physics, India and at Iowa State University, USA.

The data analysis and interpretation was done under the supervision of Professor Deena Naidoo and Dr Abhishek Pandey.

I declare that this dissertation has not been submitted before for any degree or examination at any other University.



(Nyawasedza Magoda)

10th August 2022

Abstract

Iron-based novel materials have been generating enormous interest within the scientific community for a number of decades. The efforts on such materials have intensified after the discovery of the fascinating iron-pnictide superconductors. This intriguing discovery also provides added evidence to the significance of the structure-property relationship in establishing certain functional properties. This study is expected to lead to potential exciting and tuneable properties and might open a new direction for future investigations.

The focus of this research is on the synthesis and physical property characterization of novel metallic compounds, $RuFe_3Si$ and $RhFe_3C$. In this study, the compounds under investigation were synthesized using arc-melting, the properties of these materials were explored using various experimental techniques such as X-ray diffraction, Mössbauer Spectroscopy both performed at room temperature, magnetic susceptibility (χ), electrical resistivity (ρ) and heat capacity (C_P) measurements.

The results from wavelength-dispersive spectroscopy confirmed the ratio of each of the elements relative to each other of Ru:Fe:Si and Rh:Fe:C as 1:3:1. No impurities were detected for both compounds, but patches of unreacted carbon were identified in $RhFe_3C$. Rietveld refinement of data collected from powder X-ray diffraction experiments established that both compounds crystallized in a cubic structure with $Fm\bar{3}m$ (225) space group symmetry. $RuFe_3Si$ is a single phase compound whereas $RhFe_3C$ had a secondary phase of unreacted carbon.

Transmission Mössbauer spectroscopy performed at room temperature show that $RuFe_3Si$ has four different Fe sites within its structure where one of the sites has similar environment as α-Fe. $RhFe_3C$ has three distinct Fe sites which are characterized by high magnetic internal fields.

The $\chi(T)$ data of $RuFe_3Si$ measured at H = 1000 Oe between 2 to 950 K was analyzed and revealed a high transition temperature T_c = 773(5) K. Subsequent measurements performed at H = 100 Oe resulted in an increase in the magnitude of the Curie temperature, T_c = 873(3) K. The $\chi^{-1}(T)$ data was found to obey the Curie-Wiess law which resulted in θ = 828(17) K and an effective magnetic moment μ_{eff} = 3.4(2) μ_B/Fe . The positive sign of the Weiss temperature, θ demonstrates the presence of ferromagnetic (FM) interactions within the sample. Isothermal magnetization measurements as a function of the applied field were performed at various temperatures ranging from 2 K to 900 K for the compound $RuFe_3Si$. A very

narrow hysteresis loop is observed with small values of the coercive field and the remnant magnetization, which is indicative of a soft ferromagnet.
The $\chi(T)$ data of $RhFe_3C$ measured at H = 1000 Oe between 300 to 1000 K showed no magnetic phase transitions within this temperature range.

The $\rho(T)$ measurements performed on both samples revealed a positive temperature coefficient indicating that they are metallic. Experimental $C_P(T)$ and $\rho(T)$ data for $RuFe_3Si$ was analyzed using Padé approximants representing the Debye model and Bloch-Grüneisen model which resulted in the following Debye temperatures Θ_{D} (all T) = 430(1) K. and Θ_R = 404(1)K.
The $C_V(T)$ data for $RhFe_3C$ was fitted with the Debye model with an added Einstein lattice contribution which resulted in $\Theta_{\mathrm{D}}(\text{all T}) = 784(14)$ and $\Theta_{\mathrm{E}}(\text{all T}) = 237(3)$ K . Fitting the low temperature data with a linear equation yielded a calculated value of $\Theta_{\mathrm{D}} = 453(2)$ K. The $\rho(T)$ data followed a quadratic trend which obeyed $\rho(T) = \rho_0 + AT^2$.

This study confirmed the stoichiometric ratio of the constituent elements Ru:Fe:Si and Rh:Fe:C as 1:3:1 as expected. Secondary electron images collected over the polished surfaces of $RuFe_3Si$ revealed a homogeneous structure with no detectable impurities whereas in the case of $RhFe_3C$ traces of unreacted carbon along with the main phase were observed. Both are ferromagnetic compounds that crystalize within the $Fm\bar{3}m$ (225) space group symmetry and have a very high Curie ordering temperature.

Dedication

In memory of my grandmother:

Muofhe Magoda

and my aunt:

Thinavhuyo Nancy Magoda

List of Publications and Presentation

1. List of publications (Under preparation):
   - Magoda N, Naidoo D, Pandey A, Observation of soft ferromagnetic behaviour in novel cubic compound $RuFe_3Si$.

2. National Conference Presentation:
   - Magoda N, Naidoo D, Pandey A, Investigation of a novel Iron based cubic compound $RhFe_3C$, 2021.
     Annual conference of South African Institute of Physics (SAIP), 22-27 July 2021, North-West University.
   - Best MSc oral presentation award.

Acknowledgements

Working on this dissertation has been a challenging but worthwhile experience. Throughout this entire journey, I've learnt a lot, not only has my knowledge about the field of material science expanded but I've also learnt a lot about myself. With this said, I would like to thank the following individuals/groups for their contributions towards the completion of this work:

Professor Deena Naidoo who is my supervisor for giving me an opportunity to be part of this remarkable project. Thank you for the suggestions, comments and assistance you provided towards the Mössbauer data analysis and writing this dissertation. I appreciate the remarkable supervision, support and encouragement you gave during the course of my degree.

Dr Abhishek Pandey, my co-supervisor who was immensely involved in facilitating and overseeing my experiments (both at Wits university and abroad). Thank you for your patience, advice and going out of your way to assist me with my work whenever I was facing difficulties. I am highly grateful for the time you gave and the effort you made towards helping me with the data analysis and making sure I understand.

Professor Daniel Wamwangi for assisting me with PPMS measurements and for providing valuable insight and suggestions with the data interpretation. I would also like to thank you for your patience and understanding.

Mr.Gerrard Peters for his assistance with sample preparation and Mössbauer experiment & data analysis and Mr Adam Shnier for his assistance with performing XRD measurements.

Professor Chandan Mazumdar and his team from Condensed Matter Physics Division at Saha Institute of Nuclear Physics, India for performing High-Temperature VSM measurements and for providing valuable suggestions towards the data interpretation.

Dr. Santanu Pakhira from Iowa State University, USA for performing high-temperature magnetization measurements.

The NRF for funding me throughout my degree and the Wits financial aid for their Post-graduate Merit Award (PMA). The funds gave me an opportunity to further my studies and I'll forever be grateful.

Last but not least, I would like to thank my family and friends for their support, encouragement and most importantly, for their prayers.

Table of Contents

Declaration II

Abstract III

Dedication V

List of Publications and Presentation VI

Acknowledgements VII

Table of Contents VIII

List of Figures XII

List of Tables XVII

Chapter 1 1

Introduction 1

1.1. Background 1

1.2. Application in electronic devices 1

1.3. Properties and characterization of materials 2

1.4. Literature Review 3

1.4.1. Properties of $RhFe_3N$ 3

1.4.2. Properties of α-Fe 6

1.4.3. Properties of Fe_3C 6

1.4.4. Properties of Fe_3Si 8

1.5. Motivation 10

1.6. Aims and Objectives 10

1.7. Dissertation Outline 11

Chapter 2 12

Theory 12

2.1. X-Ray Diffraction 12

2.1.1. Principles of Diffraction 13

2.1.1.1. Crystal lattice and the unit cell in three dimensions 13

2.1.1.2. Scattering from a crystal 14

2.2. Mössbauer spectroscopy 17

2.2.1. Principles of the Mössbauer Effect 17

2.2.2. Recoil-free Fraction 20

2.2.3. Hyperfine Interactions 21

2.3. Magnetism 27

2.3.1. Diamagnetism 28

2.3.2. Paramagnetism 28

2.3.3. Ferromagnetism 30

2.3.4. Ferrimagnetism 33

2.4. Specific Heat of metals 33

2.4.1. Theory of heat capacities 33

2.5. Electrical Resistivity and Magnetoresistance 38

Chapter 3 41

Experimental Techniques 41

3.1. Sample Preparation 41

3.1.1. Sample Synthesis and Annealing 41

3.1.2. Cutting 43

3.1.3. Grinding 45

3.2. Structural and Compositional Characterization Techniques 45

3.2.1. Electron Probe Micro-Analysis (EPMA) 45

3.2.2. Beam-Sample interactions 46

3.2.3. Sample Preparation 47

3.3. Instrumentation 48

3.3.1. Electron Probe Micro-analyser and its main components 48

3.3.2. Powder X-Ray diffraction 49

3.3.3. Transmission Mössbauer Spectroscopy 52

3.3.4. Magnetic and Physical Properties Measurements 55

3.3.4.1. Magnetic measurements using VSM option 57

3.3.4.2. Resistivity and Magnetoresistance measurements 58

3.3.4.3. Heat capacity measurements 60

Chapter 4 62

Results, Analysis and Discussion 62

4.1. Introduction 62

4.2. Chemical compositional, structural, magnetic, thermal and electrical transport properties of $RuFe_3Si$ 63

4.2.1. Chemical Composition 63

4.2.2. Structural Properties 64

4.2.3. Mössbauer Analysis 66

4.2.4. Magnetic Properties 68

4.2.5. Specific Heat 76

4.2.6. Electrical Resistivity 78

4.2.7. Magnetoresistance 81

4.3. Chemical compositional, structural, magnetic, thermal and electrical transport properties of $RhFe_3C$ 82

4.3.1. Chemical Composition 83

4.3.2. Structural Properties 83

4.3.3. Mössbauer Analysis 85

4.3.4. Magnetic Properties 87

4.3.5. Specific Heat 90

4.3.6. Electrical Resistivity 92

4.3.7. Magnetoresistance 93

Chapter 5 95

5.1. Conclusion and Future Work 95

5.2. Appendix A: XRD Profiles 98

5.3. References 101

List of Figures

Figure 1: Arrangement of atoms in the cubic perovskite crystal structure of $RhFe_3N$ [17]..... 3
Figure 2: Powder X-ray diffraction pattern and Rietveld refinement of $RhFe_3N$ showing the presence of two phases. The vertical green lines indicate the position of the Bragg reflection and the blue curve is the difference profile between the experimental and calculated data [16]..... 4
Figure 3: Room temperature Mössbauer spectra of $RhFe_3N$ [18]. 5
Figure 4: Isothermal magnetization of $RhFe_3N$ as a function of applied field measured at 5 K [16]..... 6
Figure 5: Mössbauer spectrum of Fe_3C collected at room temperature [14]..... 7
Figure 6: Magnetization of Fe_3C as a function of temperature. The red dash line indicates the Curie temperature [28]..... 8
Figure 7: Cubic unit cell of Fe_3Si showing two different Fe sites as well as the Si site [10]..... 8
Figure 8: Mössbauer spectrum of Fe_3Si at room temperature [30]. 9
Figure 9: (a) Magnetization versus temperature plot of Fe_3Si. (b) Magnetic moment as a function of the magnetic field measured at 6.5 K [31, 32] 10
Figure 10: A simple cubic three-dimensional lattice with three primitive vectors represented by a, b, c..... 13
Figure 11: An illustration of a lattice plane intercepting the primary axis on points x, y and z [42]..... 14
Figure 12: Geometric illustration of Bragg's law. The incoming and scattered X-rays are indicated in red. The atoms are arranged periodically as shown by the blue dots. d_{hkl} and θ represents the spacing between two adjacent layers and the incident angle, respectively. 15
Figure 13: a) Recoil of a free nuclei during emission and absorption of a γ-ray and b) elimination of recoil effect when the emitter and absorber are embedded in a solid [54]..... 17
Figure 14: Representation of nuclear resonant absorption, emission and resonance fluorescence [58]..... 18
Figure 15: Plot of the statistical energy distribution of emitted gamma rays versus transition energy [63]..... 20
Figure 16: Isomer shift in nuclear energy level due to electric monopole interactions (left) and the corresponding shift, δ as seen on the Mössbauer spectrum (right) [57]..... 23
Figure 17: Spin and oxidation states with the corresponding range of isomer shifts in Fe compounds [67]. 23

Figure 18: The electric quadrupole splitting of ^{57}Fe nuclear energy levels (left) and its characteristic view of the Mössbauer spectrum (right) [55]. 26
Figure 19: Magnetic structure of ^{57}Fe nuclear energy levels (left) and the magnetic hyperfine splitting as illustrated on the Mössbauer spectrum (right). B_{hf} is the magnitude of the hyperfine magnetic field of the nucleus [70]. 27
Figure 20: Atomic dipole representation in the presence of a magnetic field (left) and the magnetic field dependence of a diamagnetic material (right) [76]. 28
Figure 21: Atomic dipole arrangement in paramagnetic materials: a) disordered arrangement when no field is applied and b) when an external field is applied. c) shows the magnetic field dependence of a paramagnetic material indicating that an increase in temperature causes the dependence of magnetization on the applied field to become linear [78, 80]. 30
Figure 22: Atomic dipole arrangement in the absence a) and presence b) of a magnetic field. The direction of red arrows indicates the direction of the induced field and size reflects strength. [80]. 31
Figure 23: Hysteresis curve showing the variation of the magnetization of ferromagnetic materials with magnetic field [83]. 32
Figure 24: Spin dipole interaction of a ferrimagnetic material in the presence of a magnetic field (left) and the dependence of magnetization (M) on the magnetic field strength (H). 33
Figure 25: Picture showing the tube sealing unit consisting of a vacuum pump, a tank with argon gas and gas inlet pipes. 42
Figure 26: Sealed quartz tubes placed on ceramic crucibles before being placed in the furnace for annealing. 43
Figure 27: Picture showing the main components of a wire saw used to cut the samples. 44
Figure 28: Pestle and mortar used to grind the samples to powder. 45
Figure 29: An illustration of different interactions of electrons with matter. 46
Figure 30: $RuFe_3Si$ and $RhFe_3C$ with exposed sample surface mounted in epoxy. 47
Figure 31: Schematic of an Electron Probe Micro-analyser and its main components [103]. 48
Figure 32: D8-Advance BRUKER diffractometer with its main components. 50
Figure 33: Picture showing the arrangement of the main components of a diffractometer with a Lynxeye detector in the Bragg Brentano configuration [111]. 51
Figure 34: Illustration of a typical diffraction pattern obtained from ZnO nanoparticles, the peaks are indexed with Miller indices [112]. 51

Figure 35: Block diagram of a Mössbauer spectrometer arranged in transmission geometry [116]. 53
Figure 36: Nuclear decay scheme of ^{57}Fe from ^{57}Co which provides the 14.4 keV gamma radiation necessary for the Mössbauer effect [117]..... 54
Figure 37: Electronics used in data acquisition (left) and Mössbauer spectroscopy configuration in transmission geometry (right) used for this study 55
Figure 38: Quantum Design Physical Property Measurement System (PPMS) at Wits University Physics Department. 56
Figure 39: Mounting kit with sample holder. 57
Figure 40: A simplified schematic of a (VSM) [122]. 58
Figure 41: Top view of a resistivity sample puck showing samples mounted for four-wire resistance measurement. $RhFe_3C$ is connected to channel 1 and $RuFe_3Si$ is connected to channel 3. 59
Figure 42: Picture of the heat capacity sample mounting station..... 60
Figure 43: Illustration of a heat capacity sample puck with the sample mounted on the platform [124]..... 61
Figure 44: Picture of a contact baffle assembly. 61
Figure 45: Backscattered electron images of $RuFe_3Si$ showing the topography from the polished surface with a scale magnification of 500 μm taken with a beam acceleration voltage of 15 kV.63
Figure 46: Room temperature powder X-ray diffraction data collected using a Mo source. The solid red curve is the Rietveld refinement profile, the blue curve is the difference profile between the experimental data and the calculated intensities and the green vertical bars mark the Bragg positions. The two asterisks indicate the peaks that likely originate from a slight anti-site disorder present in the compound..... 64
Figure 47: Cubic crystal structure of $RuFe_3Si$. The red and blue spheres indicate a shared occupancy between Fe and Ru, each with 50% site occupancy. Si occupies only $1/6^{th}$ of its site, the remaining space is indicated in white. 66
Figure 48: TMS spectra for $RuFe_3Si$ ground powder taken at room temperature..... 67
Figure 49: Magnetic susceptibility of $RuFe_3Si$ measured at $H = 100\ Oe$. Inset: first derivative of data showing the temperature at which the magnetic phase transition temperature is observed. 69
Figure 50: Temperature variation of magnetic susceptibility χ(T) of $RuFe_3Si$ measured between 2 to 950 K at 1000 Oe. The blue data points (low-T data) were collected using the PPMS at Wits University which does not have the capacity to measure at temperatures above 300 K while the

red data points (high-T data) were collected using the PPMS at Iowa State University. Both experiments were performed on the same sample under the same conditions. 70
Figure 51: First derivative of susceptibility data where the blue dotted line passing through the minimum value of the curve indicates the phase transition temperature. 71
Figure 52: Inverse susceptibility χ^{-1} data at applied magnetic field H = 1000 Oe are plotted as a function of temperature T. The data were fitted using equation (4.1). 72
Figure 53: Isothermal magnetization M of $RuFe_3Si$ as a function of an applied magnetic field H measured at six different temperatures between 2 and 900 K. 73
Figure 54: Isothermal magnetization M versus applied magnetic field H data collected at 900 K showing a linear behaviour. 74
Figure 55: Hysteresis plot of isothermal magnetization, M versus applied magnetic field, H at T = 2 and 300 K. Inset: an expanded plot at 2 K. 75
Figure 56: Plots showing the relationship of (a) coercive field H_c and (b) saturation moment M_{sat} as a function of temperature. 76
Figure 57: Specific heat C_p versus temperature T data of $RuFe_3Si$ along with the Debye fit (black line). Inset shows a plot of $C_p(T)/T$ versus T^2 plot at low temperature (below 10 K). The red solid line a linear fit. 77
Figure 58: Temperature T variation of the electrical resistivity ρ of $RuFe_3Si$ at H = 0 T. The black solid curve is the fit by the Bloch-Gr*u*neisen (B-G) model. Inset shows the low-temperature resistivity data with a linear fit. 80
Figure 59: The standard Kadowaki-Woods plot. The position of $RuFe_3Si$ is indicated by a red dot [133]. 81
Figure 60: Temperature T dependence of electrical resistivity ρ at H = 0 T and H = 1 T. 82
Figure 61: Backscattered electron images of $RhFe_3C$ showing the topography from the polished surface with a scale magnification of 100 μm taken with a beam acceleration voltage of 15 kV. The dark areas and needle-like structures and patches observed contain unreacted carbon. 83
Figure 62: Room temperature Powder X-ray diffraction data of $RhFe_3C$ collected using Mo source. Two-phase Rietveld refinement, difference profiles and Bragg positions for $RhFe_3C$ (orange) as well as for unreacted carbon (green) are shown. The magnified section of the diffraction pattern clearly shows data and fitting around the carbon peak. 84
Figure 63: Cubic crystal structure of $RhFe_3C$. The purple and red spheres indicate a shared site between Fe and Rh. C occupies 1/6th of the 24d site. 85

Figure 64: Transmission Mössbauer spectroscopy spectrum of $RhFe_3C$ powder measured at room temperature. 86
Figure 65: Magnetic susceptibility $\chi(T)$ of $RhFe_3C$ measured in a field-cooled mode at 0.1 T. . 88
Figure 66: Magnetization versus applied magnetic field of $RhFe_3C$. 89
Figure 67: The saturation moment of $RhFe_3C$ as a function of temperature. 89
Figure 68: Specific heat data, $C_p(T)$ of $RhFe_3C$ with Debye + Einstein fit (black curve). Inset: plot of $C_p(T)/T$ vs at low temperature with a linear fit. 90
Figure 69: Resistivity ρ as a function of temperature T for $2\ K \leq T \leq 300\ K$. the solid black curve is the fit to the experimental data using $\rho(T) = \rho_0 + AT^2$. The inset exhibits ρ as a function of T^2 for $2\ K \leq T \leq 10\ K$. The solid black line is a linear fit to the data. 92
Figure 70: The Kadowaki-Woods plot. The position of $RhFe_3C$ is indicated by a red dot [133]. 93
Figure 71: Magnetoresistance $\Delta\rho/\rho$ as a function of temperature T between 2 to 300K. 94

List of Tables

Table 1: Mössbauer parameters extracted from the analysis of the $RhFe_3N$ spectrum measured at room temperature [18]. 5
Table 2: Summary of the magnetic measurements carried out on $RhFe_3N$ [16, 18] 6
Table 3: Hyperfine parameters of Fe_3C obtained at room temperature [24, 25] 7
Table 4: Magnetic moment, isomer shift and magnetic field values derived from the Mössbauer measurement on Fe_3Si performed at room temperature [23, 31, 32] 9
Table 5: A list of samples synthesized by arc melting. 42
Table 6: Atomic positions, and site occupancy summary of $RuFe_3Si$ results obtained from full Rietveld refinement of the XRD data. 65
Table 7: Room temperature hyperfine parameters obtained for the $RuFe_3Si$ powder. 68
Table 8: Variation in the magnetic phase transition temperature T_c of $RuFe_3Si$ with the applied magnetic field. 71
Table 9: Table showing a summary of magnetic parameters obtained from $M(H)$ experiment performed at different temperatures. 75
Table 10: Atomic positions and site occupancies obtained from Rietveld refinement of the room temperature powder XRD data of $RhFe_3C$. 84
Table 11: Room temperature hyperfine parameters for the compound $RhFe_3C$. 87

Chapter 1

Introduction

1.1. Background

It is well-known that the crystal structure of a crystalline material plays a major role in determining its properties by controlling the electronic and magnetic structures as well as the resultant interactions. One of the most famous and well-studied cubic structure classes is perovskite. The compounds crystallizing in this structure class have a general formula of ABX_3. [1]. Their oxygen-containing members have been reported to exhibit outstanding properties such as colossal magnetoresistance, charge-ordering and multiferroic properties [2]. On the other hand, iron is one of the most significant elements of the periodic table that exhibits outstanding properties in its pure form as well as in various compounds as a constituent element [3]. Thus, it is prudent and intuitive to explore the properties of novel iron-based cubic materials that have the general chemical formula of ABX_3 of perovskite compounds. This study aims to synthesize, explore and model the properties of novel soft ferromagnetic (FM) cubic compounds based on iron. The project goals to synthesize and systematically investigate the properties of $M\text{Fe}_3X$ (M = Rh, Ru and Pd; X = B, C and Si) compounds by a number of characterization techniques.

1.2. Application in electronic devices

Materials with advanced and desirable applied properties play an important role in a world that is shaped by technological devices. Recent developments in electronic and data storage devices have been dependent mostly on miniaturization as well as optimization of their electronic and magnetic components. This poses a need for continuous improvement of such materials as well as search for new materials that might be suitable candidates for the next generation devices [4].

Magnetism forms the basis of spintronics otherwise known as magneto electronics. This is an emerging and fast-growing technology that exploits the intrinsic spin of an electron together with its magnetic moment in solid-state device systems to achieve improved data processing, transfer and storage capabilities [5, 6]. In other words, scientists are trying to make use of the

spin of an electron rather than its charge to carry information and create devices that are more robust with increased efficiency [7].

Additionally, soft ferromagnetic materials have possible applications in the fabrication of magnetic recording devices. Such devices store/preserve data in the form of electrical signals through the magnetization of portions on a magnetic material [8]. The capacity of magnetic data storage devices has increased over the years from the production of the first disk drive, RAMAC from IBM in 1956 and this is due to developments in the study of nano-engineered composite magnetic materials and quantum mechanical processes [9]. Research in such fields may enable the fabrication of data storage devices with larger storage capacities at lower costs.

Previous studies on FM materials such as Fe_3Si has shown that such materials have excellent magnetic properties and are corrosion and oxidation resistant. In addition, iron-silicon alloys are known for their high-temperature stability, high conductivity, their soft ferromagnetism and rich electronic properties which allows them to be used in thermoelectric, spintronic and photoelectric devices [10]

1.3. Properties and characterization of materials

Solid materials can be classified according to their atomic arrangement as being crystalline or amorphous. Crystalline solids have a regular ordered array of atoms that are held together by strong interatomic forces, forming a repeating three-dimensional structure called a lattice. Amorphous solids are those that exhibit short-range order in their nearest neighbour bonds, but the local environment e.g. the number of neighbouring atoms and the distance between two neighbouring atoms varies throughout the solid [11, 12]. The degree of periodicity is smaller in an amorphous solid than in its crystalline counterpart.

To investigate the properties of our novel crystalline materials, non-destructive methods such as powder X-ray diffraction (XRD), Mössbauer spectroscopy, electrical, magnetic and thermal measurements will be utilized. Powder XRD provides information on the underlying crystal structure of the material and is also utilised to identify and quantify impurity phases [13]. Mössbauer spectroscopy, directly or indirectly, allows for the determination of structural, electronic, magnetic and chemical information of materials through hyperfine parameters extracted from fits of the spectra [14]. The magnetic properties and ordering type

can be extracted from magnetic and thermal measurements. Electrical and magnetotransport measurements allows for the determination of the ground state of materials as well information on electronic correlations and interactions between charge carriers and magnetic spins [15].

1.4. Literature Review

1.4.1. Properties of $RhFe_3N$

In 2005, Houben *et al.* [16] investigated the structural and magnetic properties of a new FM ternary nitride compound $RhFe_3N$. The study was influenced by the previous study of iron nitride γ'-Fe_4N, which crystallizes in a simple cubic structure within the space group $Pm\bar{3}m$. This investigation was motivated by the material's interesting magnetic properties which made it a suitable candidate to produce high-performance magnetic recording heads. The ternary $RhFe_3N$ compound was found to crystalize in a perovskite structure where the Rh, Fe and N atoms occupied the cube corner, face centre and body centre positions, respectively (Figure 1). High-resolution X-ray powder diffraction was used to determine the phase and structure of $RhFe_3N$ (Figure 2).

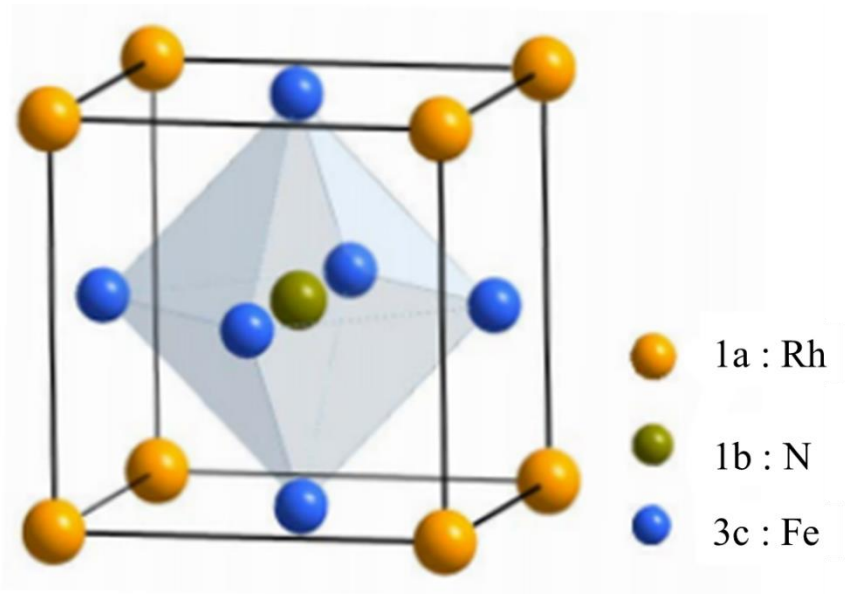


Figure 1: Arrangement of atoms in the cubic perovskite crystal structure of $RhFe_3N$ *[17]*.

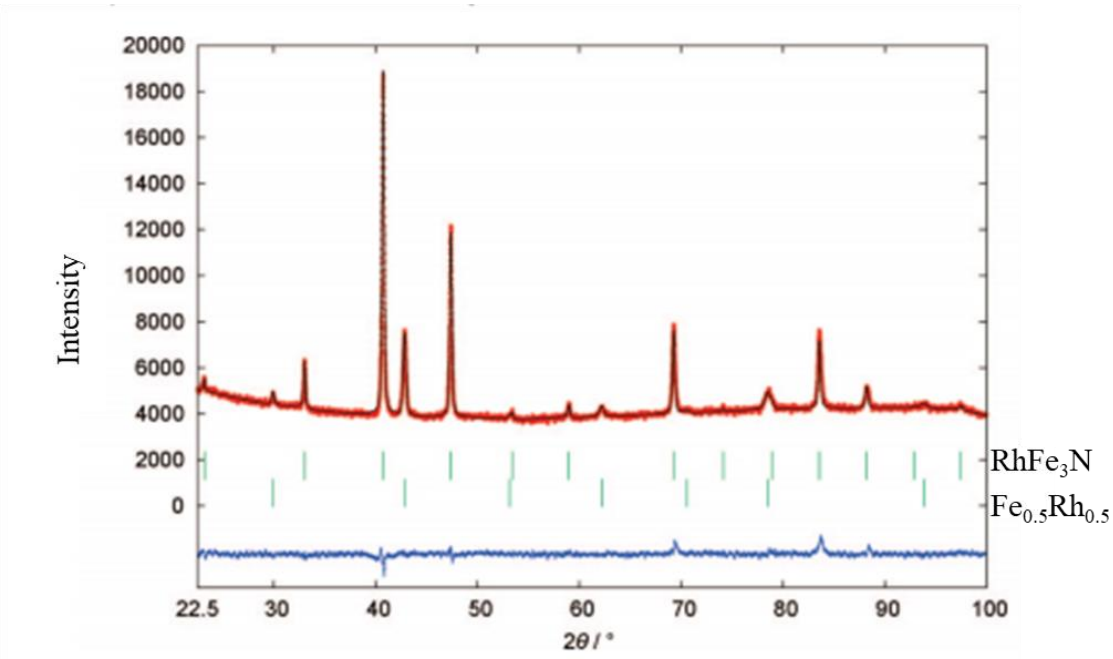


Figure 2: Powder X-ray diffraction pattern and Rietveld refinement of $RhFe_3N$ showing the presence of two phases. The vertical green lines indicate the position of the Bragg reflection and the blue curve is the difference profile between the experimental and calculated data [16]

A few years later, Houben *et al.* [18] further investigated $RhFe_3N$ using Mössbauer Spectroscopy. This study was conducted at room temperature in transmission geometry. The resulting spectrum shown in Figure 3 was dominated by two spectral components assigned to iron phases Fe(I) and Fe (II), occupying Wyckoff position 3*c* in $RhFe_3N$ and Rh was found to be occupying the 1*a* site. A list of Mössbauer parameters for the identified iron phases are summarised in Table 1

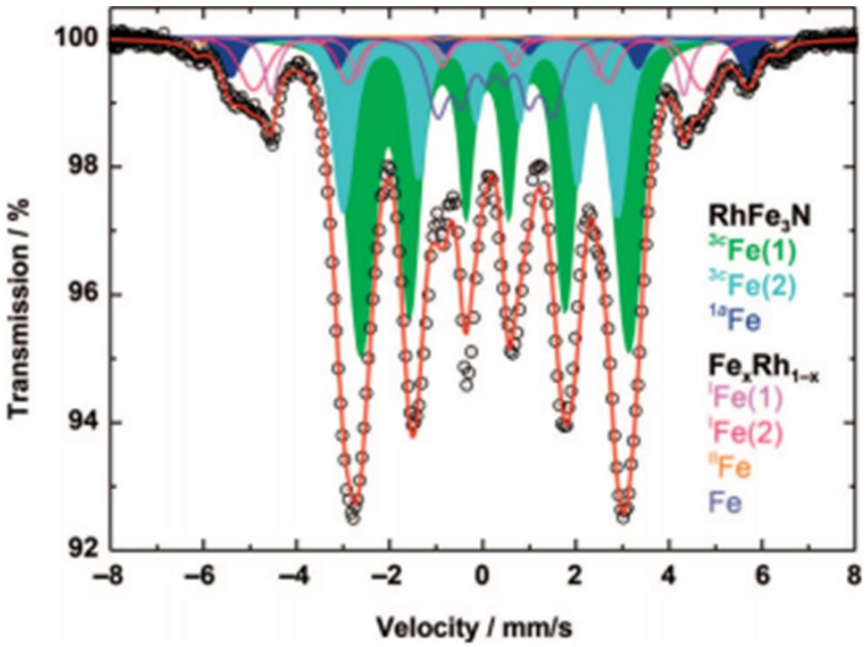


Figure 3: Room temperature Mössbauer spectra of $RhFe_3N$ *[18]*.

Table 1: Mössbauer parameters extracted from the analysis of the $RhFe_3N$ spectrum measured at room temperature *[18]*.

	^{3c}Fe(I)	**^{3c}Fe(II)**	**^{1a}Fe**
Isomer Shift (mm/s)	0.29(2)	0.25(3)	0.24(2)
Quadrupole Splitting (mm/s)	0.08(2)	-0.19(4)	0.01(1)
Magnetic Field (T)	17.93(2)	18.33(5)	34.01(2)

It was reported that the magnetic properties of this material can be influenced by substituting the iron atoms at either the face or the corner positions of the unit cell [18]. The introduced Fe atoms control crystal growth. The analytical techniques (i.e. powder X-ray diffraction and Mössbauer analysis) proved that the Rh atom occupies the corner position of the unit cell.

An investigation of the magnetic properties shows that the compound is a semihard itinerant ferromagnet. The hysteresis loop measured at 5 K is shown in Figure 4 and the summary of the magnetization data is given in Table 2.

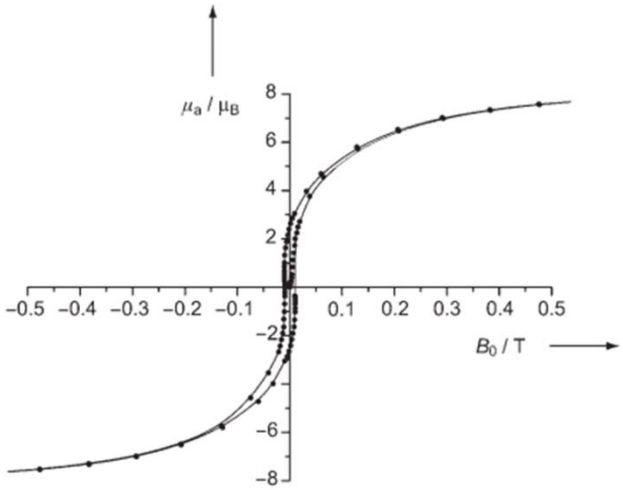


Figure 4: Isothermal magnetization of $RhFe_3N$ as a function of applied field measured at 5 K [16]**.**

Table 2: Summary of the magnetic measurements carried out on $RhFe_3N$ *[16, 18]*

Magnetization property	**Value**
Saturation magnetization	8.3 μ_B per formula unit
Coercive field	5.8 Oe
Curie temperature	505 K

1.4.2. Properties of α-Fe

α-Fe crystallizes in a body-centred cubic structure and is known to be FM. Magnetization measurements performed on pure Fe at room temperature show that it has a saturation moment of ~2.217(1) μ_B/Fe and has a Curie temperature of 1043 K [19, 20]. The Debye temperature Θ_D and the Sommerfeld coefficient γ were reported to be 465(3) K and 4.9(1) mJ/mol K^2, respectively. These values have been obtained from low-temperature heat capacity measurements [21].

1.4.3. Properties of Fe_3C

Binary Fe_3C is reported to have an orthorhombic unit cell with 16 atoms and belongs to space group Pnma (62) with the iron atoms occupying two different sites [22]. The compound is

reported to have a Θ_D of 394 K [23]. Figure 5 shows the Mössbauer spectrum obtained using ^{57}Co embedded in Rh matrix as a source at room temperature. The spectrum contains Lorentzian line fits for Fe_3C which consists of two sextets and a doublet. The derived parameters are reported in Table 3.

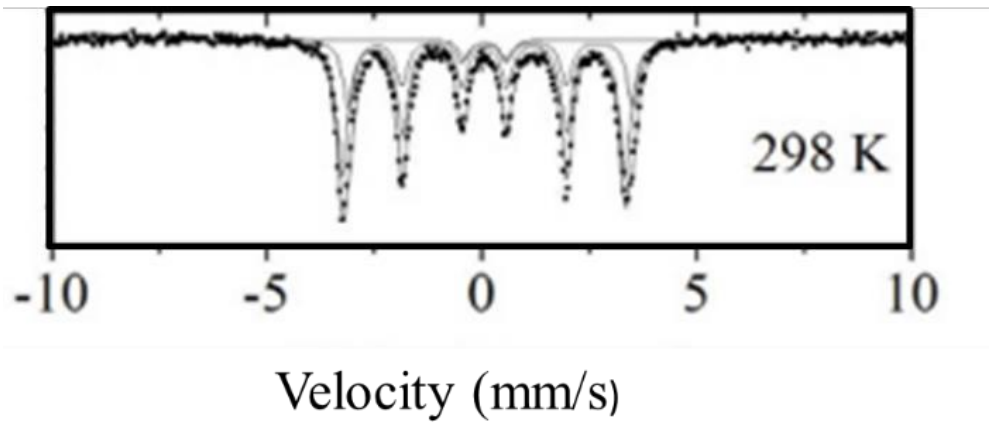


Figure 5: Mössbauer spectrum of Fe_3C collected at room temperature *[14]*.

Table 3: Hyperfine parameters of Fe_3C obtained at room temperature *[14, 24]*

Parameter	Fe(I)	Fe(II)
Magnetic moment (μ_B)	1.98	1.74
Isomer shift (mm/s)	0.17 $\pm$0.02	0.17 $\pm$0.02
Magnetic hyperfine field (T)	20.5 - 20.9	19.4 – 20.7

Isothermal magnetization studies performed on Fe_3C show that the saturation magnetic moment lies between 5.34 and 5.77 μ_B/f.u. (1.79 and 1.92 μ_B/Fe) with an effective magnetic moment μ_{eff} of 3.89 μ_B/Fe [22, 25]. Magnetization measurements performed as a function of temperature (Figure 6) reveal that the compound's Curie temperature ranges from 459 to 483 K [24, 26].

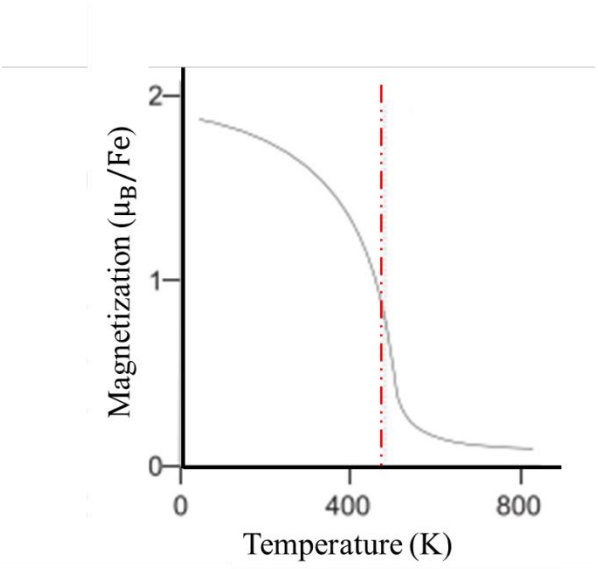


Figure 6: Magnetization of Fe_3C as a function of temperature. The red dash line indicates the Curie temperature *[26]***.**

1.4.4. Properties of Fe_3Si

Rausch *et al.* [27] synthesized Fe_3Si by arc melting the stoichiometric amounts of iron and silicon and annealing the resultant compound at 1000 °C for 3 days. The binary Fe_3Si crystalizes in the cubic DO_3 structure as shown in Figure 7. The unit cell has two different Fe sites, represented by Fe(I) and Fe(II). The site Fe(I) has eight Fe(II) nearest neighbours while Fe(II) has four Si and four Fe(I) as nearest neighbours.

.

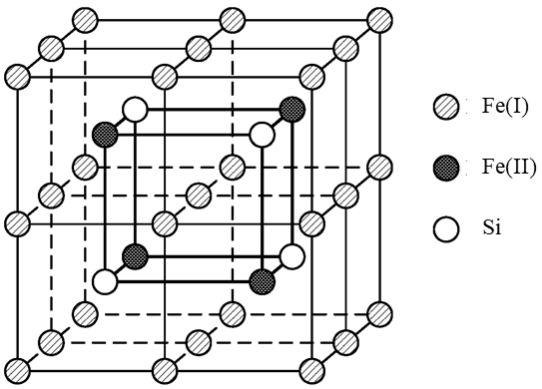


Figure 7: Cubic unit cell of Fe_3Si showing two different Fe sites as well as the Si site *[10]***.**

Gustavo [28] conducted studies to investigate the Mössbauer and magnetic properties of Fe_3Si which was prepared by arc melting its constituent elements (with 99.99% purity) in argon atmosphere. ^{57}Fe Mössbauer measurements were performed at room temperature in transmission geometry using ^{57}Co embedded in Cr matrix. The resulting spectrum is shown in Figure 8 and consists of two sextets. Parameters obtained from fitting the spectra with the two components are listed in Table 4.

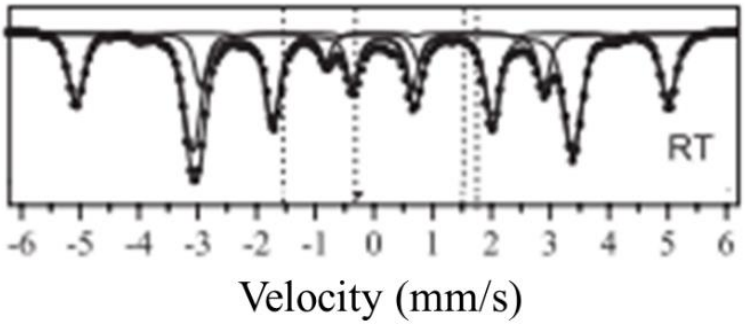


Figure 8: Mössbauer spectrum of Fe_3Si at room temperature *[28]*.

Table 4: Magnetic moment, isomer shift and magnetic field values derived from the Mössbauer measurement on Fe_3Si performed at room temperature *[23, 29, 30]*.

Parameter	**Fe(I)**	**Fe(II)**
Magnetic moment (μ_B)	1.98 – 2.2	1.15 – 1.74
Isomer shift (mm/s)	0.25 $\pm$0.1	0.5$\pm$0.1
Magnetic splitting (kOe)	305 $\pm$10	195 $\pm$10

A study was conducted by Liang *et al.* [31]to determine the thermodynamic properties of Fe_3Si, where the phonon approach and Debye model were used to predict the vibrational thermodynamic contributions for Fe-Si systems. The Θ_D was reported as 458 K, which is greater than the value of 394 K reported by Haglund and Grimvall [23]. The γ was found to lie in the range 5.4 to 6.25 mJ/mol K^2 [23].

The cubic binary Fe_3Si is an FM compound and magnetization measurements show that the compound has a Curie temperature in the range 800 to 853 K (Figure 9(a)) [29, 30]. The measured saturation magnetization at 6.5 K was reported to be ~4.8 μ_B/f.u. [30].

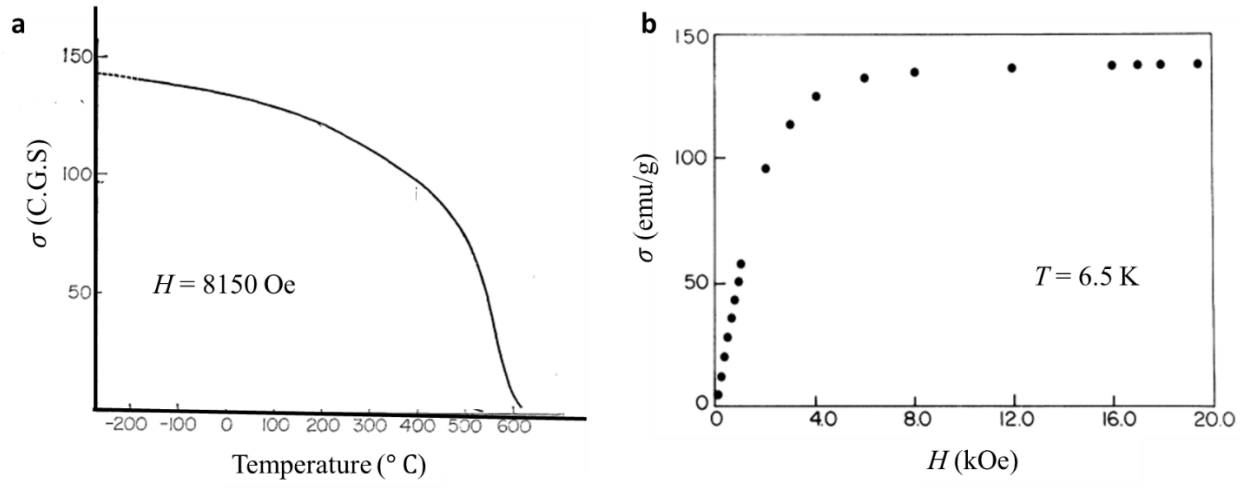


Figure 9: (a) Magnetization versus temperature plot of Fe_3Si. (b) Magnetic moment as a function of the magnetic field measured at 6.5 K [29, 30]

1.5. Motivation

Magnetism is known to be one of the most essential class of physical attributes in condensed matter physics. Magnetic materials are an important integral part of our lives and play a very significant role in the fabrication of almost all electronic devices. Additionally, magnetic materials with tunable properties play a vital role in the emerging field of spintronics [32]. A previous study of magnetic itinerant FM material $RhFe_3N$ showed that this compound crystallizes in a cubic perovskite structure and exhibits properties that are suitable for magnetic recording devices. The potential of such materials to contribute to the improvement of data storage or recording devices has not been fully explored. In this study, the plan is to synthesize and comprehensively investigate novel cubic materials based on the framework of Fe atoms that are stoichiometrically related to $RhFe_3N$. This project intends to realise exciting and tunable properties within these systems. Specifically, the cubic materials $RuFe_3Si$ and $RhFe_3C$ have the potential to be used in high-performance magnetic and storage devices [18].

1.6. Aims and Objectives

The purpose of this research is to synthesize and investigate the properties of novel ternary compounds $RuFe_3Si$ and $RhFe_3C$ using various experimental techniques.

The objectives are to:

- synthesize novel soft-FM materials using a high-yield synthesis technique.
- investigate the crystal structure of the materials by analysing data obtained from powder X-Ray diffraction.
- study the electronic, chemical and magnetic structure of the samples using transmission Mössbauer spectroscopy.
- thoroughly examine the structural, magnetic, thermal and electrical transport properties of the novel materials.
- analyse and model the data collected from the different techniques and establish the correlation between them.

1.7. Dissertation Outline

This dissertation consists of five main chapters, the first chapter serves as an introduction to perovskite structures and give background information on ferromagnetic materials and their importance in electronics. We briefly introduced the analytical techniques used to investigate materials and what information we can obtain from them to assist in characterizing compounds. The chapter also includes a literature survey on the properties of some compounds that are related to the materials we were investigating.

In the second chapter we explored the theoretical background and underlying physics that govern the techniques used for this study. Chapter 3 gives a detailed description of the experimental methods that were used. This is followed by chapter 4 where results are presented and interpreted. The final chapter gives us the conclusion and some recommendations for future work. Appendices containing XRD profiles from other compounds that were initially suggested is presented at the end of the dissertation.

Chapter 2

Theory

This chapter gives a brief introduction and background on the techniques used in this study. Section 1 includes basic X-ray diffraction concepts such as unit cell, crystal lattice and fundamental concepts of diffraction. Section 2 provides information about Mössbauer spectroscopy and a discussion of hyperfine interactions. Lastly, the theory of physical properties of the materials being investigated is explained in detail. For this study, more attention was given to magnetism, resistivity and heat capacity.

2.1. X-Ray Diffraction

In 1912, the physicist Von Laue postulated that crystals were made up of regularly spaced atoms that could serve as scattering centres for incoming X-ray beams. Given that the wavelength of X-rays is approximately the size of the interatomic distance of the crystals, it is possible to diffract X-rays through the crystals [33, 34]. Since the atoms are systematically ordered, the scattered X-rays give us information about the type of atoms present and how these atoms are arranged in the periodic lattice. XRD is a non-destructive technique used to identify crystalline phases, orientation and to characterize structural properties [35].

All crystalline materials are composed of atoms that are arranged in a specific pattern on a lattice which is periodic in all three dimensions [33]. Crystals can either be identified as a single crystal (consists of one crystal) or polycrystalline (consists of many crystals orientated along different directions with well-defined boundaries). Single crystals consist of a periodic atomic structure and each atom is related to every other atom by some translational and rotational symmetry while polycrystalline materials are an assembly of a large collection of small crystallites.

In total, fourteen Bravais lattice systems are grouped into seven crystal systems. These systems are triclinic, monoclinic, orthorhombic, tetragonal, cubic, hexagonal and trigonal [36].

2.1.1. Principles of Diffraction

The three-dimensional structure of crystalline materials is defined by repeating planes of atoms, forming a lattice. If a focused X-Ray beam is incident on these planes made of atoms, it can either be transmitted, absorbed, scattered or diffracted [37]. When an X-Ray beam is diffracted after interacting with an atom, the distance between the planes of atoms can be determined by applying Bragg's law [37].

2.1.1.1. Crystal lattice and the unit cell in three dimensions

The lattice of a crystal is described by a right-handed coordinate system and the smallest component that contains all important structural and chemical information to define a material is referred to as a unit cell [38]. To fully describe a three-dimensional lattice (a unit cell), three non-coplanar vectors are required, the length (given by a, b and c with angle α, β and γ between them) of the primary vectors are referred to as lattice constants [34, 39]. Lattice points on the crystal can be described by the vector $\vec{r} = u\vec{a} + v\vec{b} + w\vec{c}$ where u, v and w are integers.

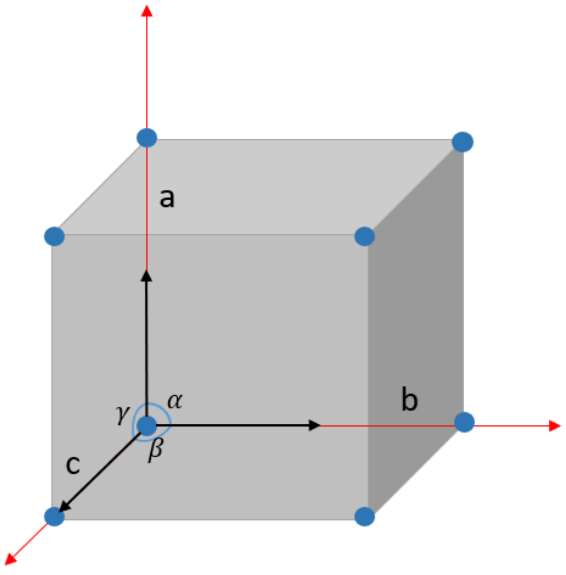


Figure 10: A simple cubic three-dimensional lattice with three primitive vectors represented by a, b, *c*.

Crystal structures play an important role in the determination of properties of materials. For instance, the atoms in a FCC unit cell are more closely packed than the BCC unit cell and hence the density of materials with a FCC structure is higher compared to that of materials with a BCC structure [40].

The orientation of a plane in a lattice is identified by its Miller indices (*h,k,l*), which are reciprocals of the intercept made by the planes on the primary axes of the crystal [36, 41]. As shown in Figure 11, the Miller indices of a plane which intercepts the axis at points *x, y , z* makes fractional intercept of $\frac{1}{x},\frac{1}{y},\frac{1}{z}$ [33]:

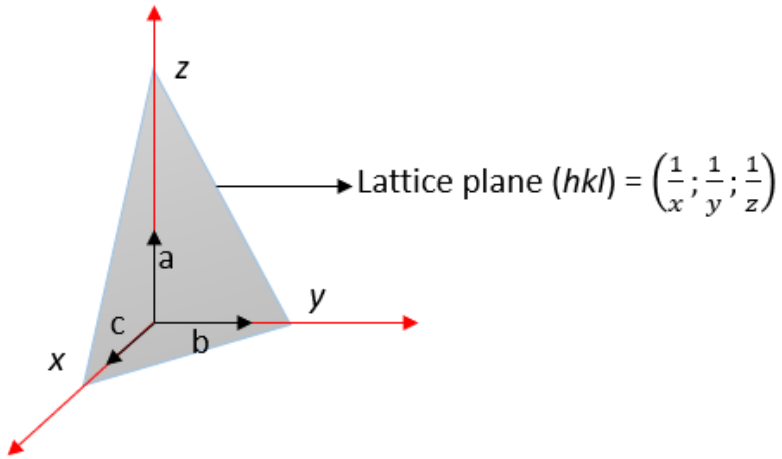


Figure 11: An illustration of a lattice plane intercepting the primary axis on points *x, y* and z *[39]*.

2.1.1.2. Scattering from a crystal

Diffraction occurs when a wave is incident on atoms arranged in a regular pattern and causes the wave to scatter given that the spacing between these atoms are comparable with the wavelength of the wave. In theory, an electron in an alternating electromagnetic field will oscillate with the same frequency as the field, the same phenomenon is observed when an X-ray beam is incident on an atom [42]. When this occurs, electrons can either be ejected from the atom (if the energy is sufficient for excitation to occur) or X-rays could scatter from the atom within the target material.

The diffraction of X-rays in crystals is dependent on the phase of the diffracted waves and is governed by Bragg's law [40]. Two parallel incoming rays with wavelength λ strike a set of

crystal planes separated by a distance d. Diffraction is observed when the extra distance that the wave has to travel is equal to an integer multiple of the wavelength i.e. $n\lambda$ (see Figure 12). The geometrical analysis of the crystal structure results in Bragg's law:

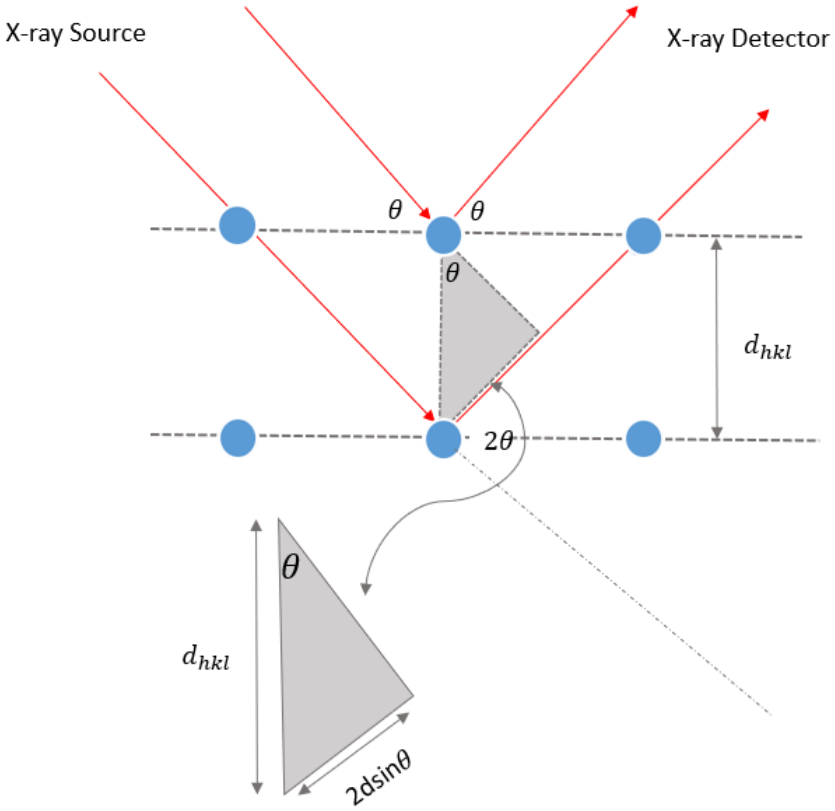


Figure 12: Geometric illustration of Bragg's law. The incoming and scattered X-rays are indicated in red. The atoms are arranged periodically as shown by the blue dots. d_{hkl} and θ represents the spacing between two adjacent layers and the incident angle, respectively.

By applying trigonometric rules, the difference in path length can be determined as $d\,sin\,\theta$ and

$$n\lambda = 2d_{hkl}\,sin\,\theta \qquad n = 1, 2, 3, \ldots \tag{2.1}$$

where n corresponds to the number of wavelengths in path difference between the diffracted X-rays from adjacent planes within the crystal lattice and θ is the angle between the incoming X-rays and the horizontal plane of the lattice [43]. The interplanar spacing, d_{hkl} for any set of planes is given by [44]:

$$\frac{1}{{d_{hkl}}^2} = \frac{h^2}{a^2} + \frac{k^2}{b^2} + \frac{l^2}{c^2} \tag{2.2}$$

For a cubic system where $a = b = c$, the above equation reduces to:

$$d_{hkl} = \frac{a}{\sqrt{h^2 + k^2 + l^2}} \tag{2.3}$$

where $'a'$ is the lattice constant and *h, k* and *l* are the Miller indices.

The resulting diffraction pattern plots show peak diffraction intensities as a function of diffraction angles, which indicate the position of atoms within the unit cell [45]. These plots are characterized by different components i.e. the peak position, peak intensity and peak shape [34]. The peaks represent locations where the incident X-ray beam has been diffracted by the lattice [37].

The peak intensities occur at specific planes within the crystal and these are characterized by the Miller indices *h,k,l*. The phase and amplitude of the wave diffracted from these planes is described by a mathematical function known as the structure factor F_{hkl} which is dependent on the type of crystal system involved. The structure factor is used to describe the amplitude and phase $\phi(hkl)$of a diffracted beam [46]. The structure factor is expressed as (in Euler form):

$$F_{hkl} = \sum_{j=1}^{n} f_j e^{2\pi i[hx+ky+lz]} \tag{2.4}$$

where *f* is the atomic form factor which is a measure for the ability of an atom to scatter X-rays and x, y, z are the atomic coordinates and represent the positions of atoms inside the unit cells [47]. The structure factor thus depends on the position of atoms in the unit cell, the Miller indices of the reflection and the atomic scattering factor [48]. The intensity is equivalent to the square of the structure factor [49]:

$$I_{hkl} \sim |F_{hkl}|^2$$

The peak intensity hence vanishes in certain directions and only exists when the structure factor is non-zero [36].

2.2. Mössbauer spectroscopy

Mössbauer spectroscopy is based on the theory of the Mössbauer effect which was discovered by Rudolf Mössbauer for which he was awarded the Nobel Prize in Physics in 1961. This phenomenon is based on the recoilless emission and absorption of gamma radiation and is known for its ability to produce monochromatic electromagnetic radiation with a narrow energy spectrum hence allowing it to resolve minute energy differences [50].

2.2.1. Principles of the Mössbauer Effect

During radiation emission, the gamma radiation has momentum $p_\gamma = E_\gamma / c$ where c is the speed of light Considering the conservation of momentum, an isolated atom emitting radiation must recoil with momentum $p_{nucleus} = -p_\gamma$ resulting in a decrease in energy of the emitted γ –radiation [51, 52].

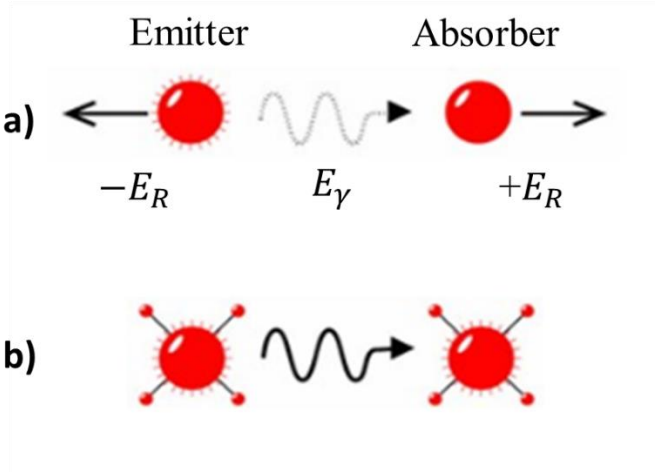


Figure 13: a) Recoil of a free nuclei during emission and absorption of a γ-ray and b) elimination of recoil effect when the emitter and absorber are embedded in a solid *[52]***.**

The recoil energy is given by:

$$E_R = \frac{(p_{nucleus})^2}{2m} = \frac{(-p_\gamma)^2}{2m} = \frac{{E_\gamma}^2}{2mc^2} \tag{2.5}$$

However, if both atoms under investigation are embedded in a crystal, the mass *'m'* in equation (2.5) becomes the mass of the whole crystal then the recoil effects become negligible. During the Mössbauer effect, a nucleus in its excited state with energy E_e transitions to its ground state by releasing gamma radiation with energy $\Delta E = E_e - E_g$ [53], this radiation may be absorbed (under certain conditions) by another nucleus, in its ground state of the same kind (same number of protons and neutrons). The absorbing nucleus excites and re-emits the energy of the photon either as another photon of the same energy or conversion electrons [54, 55]. Figure 14 shows a schematic representation of nuclear resonant absorption and emission.

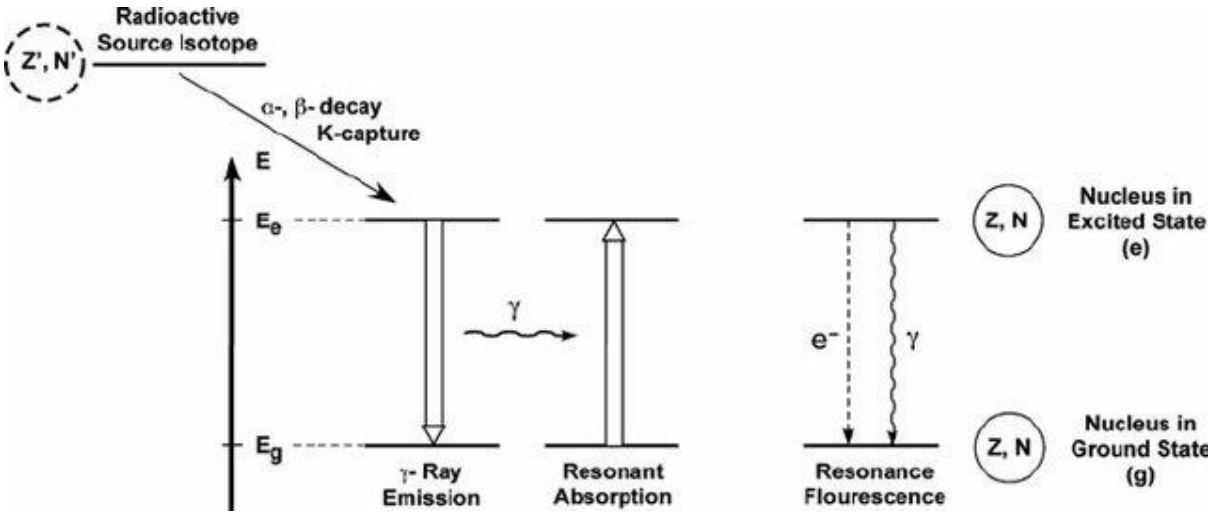


Figure 14: Representation of nuclear resonant absorption, emission and resonance fluorescence [53]**.**

A source moving relative to the absorber with velocity *v* introduces a Doppler shift in the energy of the gamma radiation released,

$$\Delta E_\gamma = E_\gamma \frac{v}{c} \tag{2.6}$$

where E_γ is the gamma-ray energy, v is a known velocity and c is the speed of light [56]. This is achieved by moving the absorber relative to the source (sample) thus modulating the γ −ray energy arriving at the absorber by the Doppler effect. By varying the velocity and thus the energy shift, it is possible to scan through a range of energies which fall within the order of those for natural line width in nuclear processes and hyperfine structure in the energy levels. The amount of resonant nuclear γ −absorption is determined by the overlap of the shifted emission and the absorption line [57] . Maximum resonance occurs at complete overlap of emission and absorption lines.

The energy of the emitted gamma rays is not monoenergetic but instead exhibit an energy distribution which follows a Lorentzian profile around E_0 as shown in Figure 15 [57, 58]. The dependence of the intensity of emitted photons on energy E is given by the Breit-Wigner equation [59]. E_0 is the centre of the emission line:

$$I(E) = \frac{\left(\Gamma/2\right)^2}{(E - E_0)^2 + \left(\Gamma/2\right)^2} \tag{2.7}$$

Figure 15 illustrates the transition energy intensity as a function of transition energy for emitted gamma radiation. The width at half maximum of the spectral line, Γ is the natural linewidth which is defined by the expression below according to the Heisenberg uncertainty principle where τ is the mean lifetime of the excited state h is the Planck constant and $t_{1/2}$ is the half-life of the radioactive element [53, 59]:

$$\Gamma = \frac{h}{2\pi\tau} = \frac{\hbar ln2}{t_{1/2}} \tag{2.8}$$

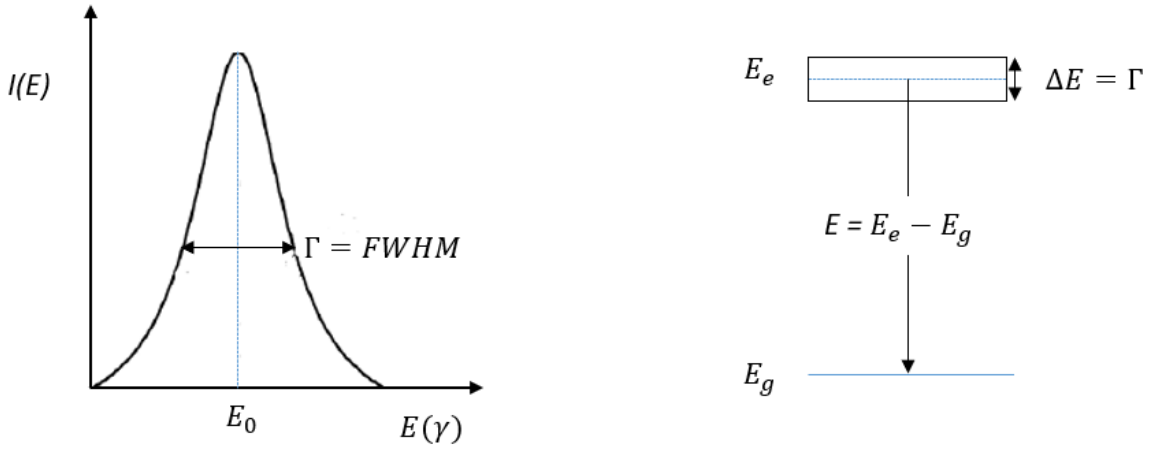


Figure 15: Plot of the statistical energy distribution of emitted gamma rays versus transition energy *[60]*.

2.2.2. Recoil-free Fraction

The recoil-free fraction of the source/absorber denotes the fraction of gamma radiation that is emitted/absorbed without recoil and is related to the vibrational properties of the crystal lattice [53, 61]. Since recoilless processes occur when the recoil energy is absorbed by the entire lattice, the recoil-free fraction depends on the structure of the lattice and the strength of the interatomic forces between the Mössbauer atoms and the crystal it is situated in [61]. During the Mössbauer Effect, the nucleus is rigidly bound in its environment and cannot move freely but it can vibrate around their positions with a well-defined frequency and amplitude which is dependent on the crystal structure of the material and temperature [59]. These lattice vibrations are quantized in the form of packets called phonons.

The expression of the recoil-free fraction, f can be expressed in terms of the gamma-ray energy E_γ and the mean square vibrational amplitude $\langle x^2 \rangle$ in the direction of the gamma radiation:

$$f = exp\left[\frac{-\langle x^2 \rangle {E_\gamma}^2}{(\hbar c)^2}\right] \tag{2.9}$$

In cases where the Debye model is used to represent the vibrational frequency spectrum of the lattice, the Debye-Weller factor takes the following form:

$$f = exp\left[\frac{-3E_R}{2k_B\Theta_{\mathrm{D}}}\left\{1 + 4\left(\frac{T}{\Theta_{\mathrm{D}}}\right)^2 \int_0^{\frac{\Theta_{\mathrm{D}}}{T}} \frac{x}{e^x - 1}\,dx\right\}\right] \tag{2.10}$$

where E_R is the recoil energy, k_B is the Boltzmann constant, Θ_{D} is the Debye temperature and T is the absolute temperature of the solid.

At low temperatures where $T \ll \Theta_{\mathrm{D}}$ expression (2.10) reduces to:

$$f = exp\left[\frac{-3\,E_R}{2k_B\Theta_{\mathrm{D}}}\right] \tag{2.11}$$

and

$$f = exp\left(-\frac{6\,E_R T}{k_B {\Theta_{\mathrm{D}}}^2}\right) \text{ for } T > \Theta_{\mathrm{D}} \tag{2.12}$$

By inspecting the equations (2.11) and (2.12), the following observations can be made:

- The recoil-free fraction will be large for small values of E_γ and tightly bound atoms (i.e. atoms with a high Debye temperature, Θ_{D}). This is because tightly bound atoms will have a smaller value of $\langle x^2 \rangle$, reducing the value of f and hence a smaller resonance effect will be observed [55].
- *f* increases with decreasing temperature *T*, this is because higher temperatures lead to larger mean square displacement $\langle x^2 \rangle$ which according to equation (2.9) decreases the value of the recoil-free fraction [53].

2.2.3. Hyperfine Interactions

By studying the Mössbauer spectra, one can obtain quantitative information on hyperfine interactions, which are minute interactions between the nucleus of the Mössbauer atom and

its surrounding electrons [62]. The energy levels in the absorbing nucleus can be modified by their environment in three main ways: by the electric monopole interaction, electric quadrupole interaction and the magnetic dipole interaction.

2.2.3.1. Electric Monopole Interaction: Isomer shift

The electric monopole interaction is the Coulomb interaction between protons of the nucleus and electrons (mainly *s*-electrons) penetrating the nuclear field [63]. This results in the shift in energy observed in the Mössbauer spectrum when the atom is in different materials and is related to the electron density of the nucleus [62]. A Mössbauer experiment measures the difference in energies between the emitting and the absorbing nuclei δ, this is referred to as the isomer shift.

The volume of the nucleus in its ground state is different from the volume in its excited state and the *s*-electrons are affected by the chemical environment. The relationship between the *s*-electron density and the nuclear radius is given by:

$$\delta = \frac{2}{3}\pi Z e^2 [|\psi_s(0)_E|^2 - |\psi_s(0)_A|^2]\left(\langle {R_e}^2 \rangle - \langle {R_g}^2 \rangle\right) \tag{2.13}$$

where

- $\langle {R_g}^2 \rangle$ and $\langle {R_e}^2 \rangle$ are the mean square radii of the nuclear ground and excited states, respectively.
- $|\psi_s(0)_E|^2$ and $|\psi_s(0)_A|^2$ are the electron densities of the emitting and absorbing nucleus, respectively.
- e is the electron charge.
- Z is the atomic number of the nucleus.

On the spectrum, the isomer shift is represented by the shift from 0 source velocity to a certain value of $v(\mathrm{mm/s})$ (the shift can either be positive or negative). This implies that resonance occurs at speed $v \neq 0$, i.e. at an offset from 0 velocity in the spectrum.

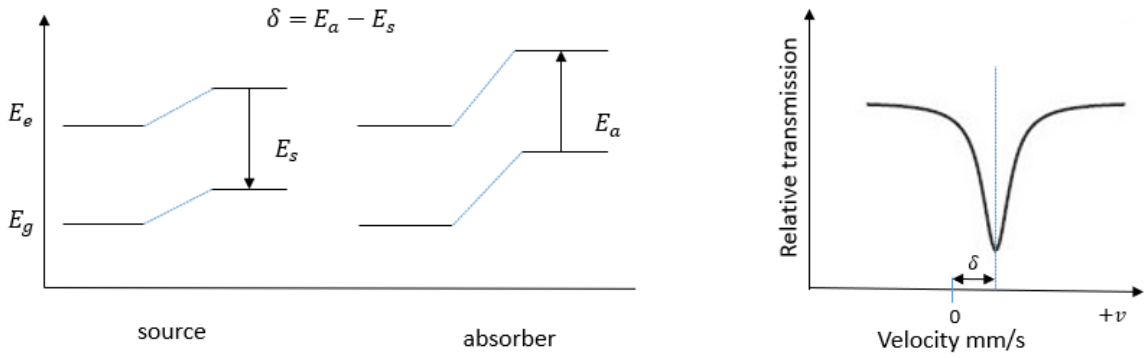


Figure 16: Isomer shift in nuclear energy level due to electric monopole interactions (left) and the corresponding shift, δ as seen on the Mössbauer spectrum (right) *[55]*.

Figure 17 shows a range of isomer shift values which is useful in determining the valence and spin state of Fe ions.

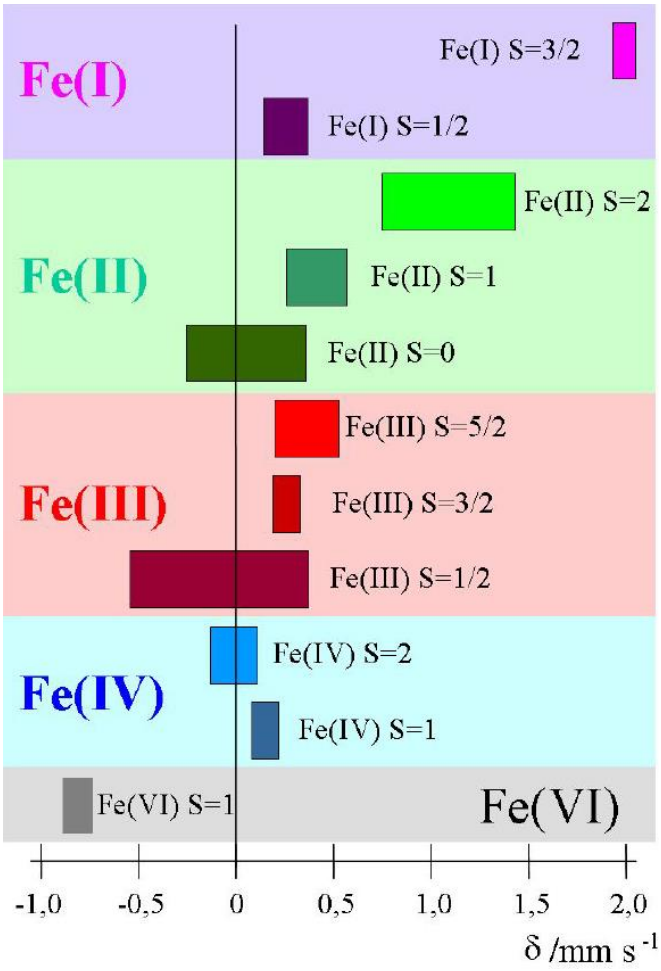


Figure 17: Spin and oxidation states with the corresponding range of isomer shifts in Fe compounds *[64]*.

2.2.3.2. Electric Quadrupole Interaction: Quadrupole Splitting/Shift.

Electric quadrupole splitting occurs if at least one of the nuclear states involved possesses a quadrupole moment *eQ* (nuclear state with spin $I > \frac{1}{2}$) and if the electric field at the nucleus is inhomogeneous. The nucleus has an electric quadrupole moment that originates with its asymmetrical shape which depends on its spin [62]. It is a measure of the crystallographic site distortion, valence and spin state of the absorber nucleus. This interaction is induced by the electric quadrupole moment *(Q)* of the nucleus and the presence of an electric field gradient (EFG), which is caused by electron interactions.

The spin of the nucleus in its ground state differs from that in its excited state and a separation corresponding to the transition between two substates is observed. ΔE_Q is known as the quadrupole splitting and is defined as:

$$\Delta E_Q = \frac{e^2 q Q}{2}\left(1 + \frac{\eta^2}{3}\right)^{1/2} \tag{2.14}$$

and occurs in nuclei with charge distributions that are not spherical (i.e. in nuclei with spin quantum numbers that are greater than $1/2$). The sign of *Q* depends on the shape of the deformation, a negative quadrupole moment indicates an oblate nucleus whereas a positive moment indicates a prolate nucleus.

The quadrupole moment and the EFG are given by:

$$Q = \int \rho(r)[3z^2 - r^2]d^3r \tag{2.15}$$

where the resultant sign of *Q* provides us with information about the shape of deformation of the nucleus.

$$\Delta E = -\frac{\partial^2 V}{\partial x_i \partial x_j} \tag{2.16}$$

where *V* is the electrostatic potential

Contributions to the EFG are [65]:

- Lattice contributions from charges on distant ions.
- Valence contributions due to incompletely filled electron shells

If a suitable coordinate system is chosen, then the EFG can be represented by three principal axes: V_{xx}, V_{yy} and V_{zz} and an asymmetry parameter given by:

$$\eta = \frac{V_{xx} - V_{yy}}{V_{zz}} \tag{2.17}$$

where:

$$V_{xx} = \frac{\partial^2 V}{\partial x^2}, V_{yy} = \frac{\partial^2 V}{\partial y^2} \; and \; V_{zz} = \frac{\partial^2 V}{\partial z^2}$$

The value of η lies between 0 and 1 ($0 \leq \eta \leq 1$) and the direction of the main axes x, y, z are chosen in such a way that the tensor components satisfy the following relation:

$$|V_{zz}| > |V_{xx}| \geq |V_{yy}|$$

The transition between the ground state with spin $I = 1/2$ which has no quadrupole moment and hence remains unsplit and the first excited state with spin $I = 3/2$ which is split into two energy levels, $m_l = \pm 3/2$ and $m_I = \pm 1/2$ (see Figure 18). This type of interaction gives information regarding the symmetry of the charge around the nuclei.

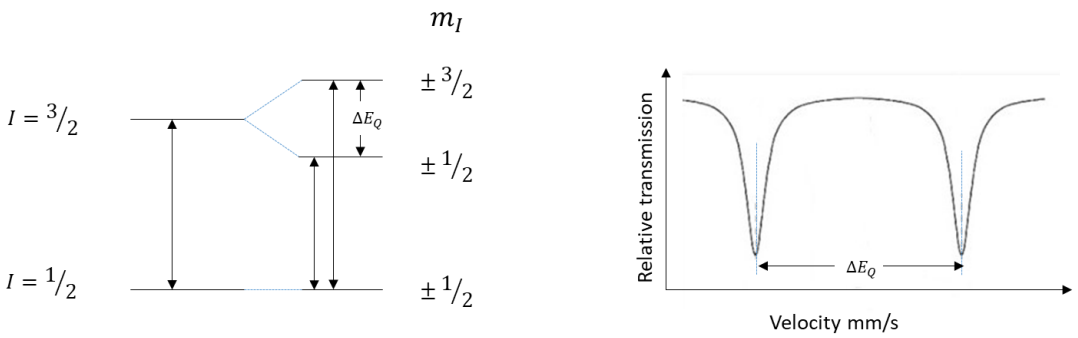


Figure 18: The electric quadrupole splitting of ^{57}Fe nuclear energy levels (left) and its characteristic view of the Mössbauer spectrum (right) *[53]*.

2.2.3.3. Magnetic Dipole Interaction: Magnetic Splitting

This is caused by the interaction of the magnetic dipole moment, μ of a nucleus with a magnetic field. The effective magnetic field experienced by the nucleus is a combination of fields from the atom itself, from within the crystal via exchange interaction and from externally applied magnetic fields which will be considered as a single field, $\vec{H}$ in this regard [66, 50]. The Hamiltonian for the magnetic hyperfine interaction is given by the equation below, where μ_N is the nuclear magneton, g is the nuclear *g*-factor, $\vec{I}$ is the nuclear spin.

$$H = -\mu \cdot \vec{H} = -g\mu_N \vec{I} \cdot \vec{H} \tag{2.18}$$

The allowed transitions between the sub-energy levels of the excited state and the ground state are governed by the following selection rule; $\Delta I = \pm 1$ and $\Delta m = 0, \pm 1$.

The excited state with $I = 3/2$ splits into four substates and ground state with $I = 1/2$ splits to two states (see Figure 19). In total, six possible transitions are possible, corresponding to six peaks on the Mössbauer spectrum with an intensity ratio of $3:2:1:1:2:3$ [67]. The magnetic splitting gives information about the magnetic properties of the material that is under investigation.

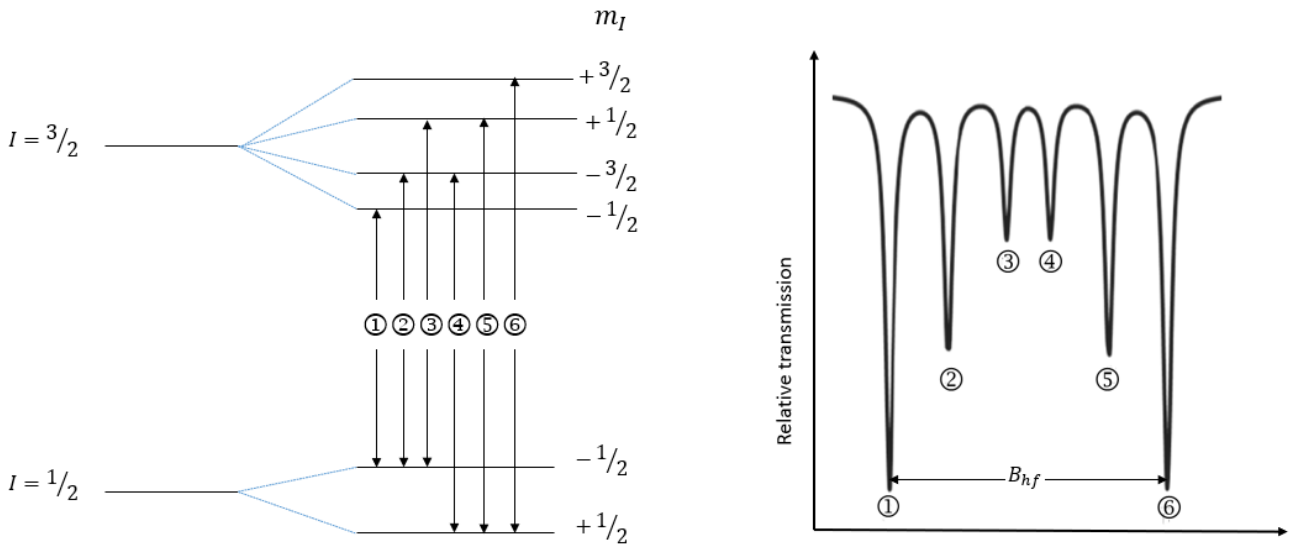


Figure 19: Magnetic structure of ^{57}Fe nuclear energy levels (left) and the magnetic hyperfine splitting as illustrated on the Mössbauer spectrum (right). B_{hf} is the magnitude of the hyperfine magnetic field of the nucleus *[67]*.

2.3. Magnetism

The magnetic properties of materials originate from the underlying magnetic moments, interaction between the moments and the resultant magnetic spin structure. The magnetic behaviour of materials can be usually characterized by magnetic susceptibility (χ), which is the relative strength of the induced magnetization (M) to the strength of the applied magnetic field (H) [68].

$$\chi = \frac{M}{H} \tag{2.19}$$

where M is a measure of the magnetic moment per unit volume of the material. Materials can be classified into different categories depending on the sign and magnitude of the susceptibility (χ), which is a parameter that measures the degree of magnetization of the material in response to an applied field and aids in determining the type of magnetic material [69]. A description of the basic types of magnetism is given below:

When a material experiences a magnetic field, the magnetic forces of the electrons in the material are affected and its magnetic properties are due to the motion of electrons of the atoms. In most atoms, electrons are arranged in pairs with spins in opposite directions. These paired electrons with opposite spins cause the magnetic field to cancel each other hence no net magnetic field exists. Materials with unpaired electrons have a net magnetic field and can interact with an external field. Materials can be classified based on their magnetic behaviour into one of the following categories:

2.3.1. Diamagnetism

In diamagnetic materials, all atoms have paired electrons hence the net magnetic moment is zero. However, when an external magnetic field acts on atoms, it interacts with their orbiting electrons and creates a small magnetization (*M*) in the opposite direction to that of the magnetic field [70, 71]. These materials have a very weak and negative magnetization and the susceptibility is small, negative (*M* is opposite to *H*) and does not depend on temperature [36, 70, 71]. Figure 20 shows the behaviour of a diamagnetic material when a field is applied on it.

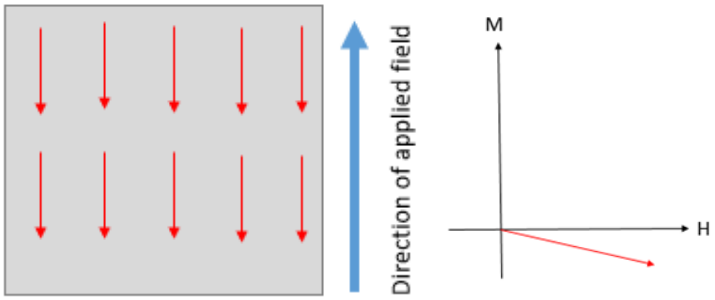


Figure 20: Atomic dipole representation in the presence of a magnetic field (left) and the magnetic field dependence of a diamagnetic material (right) *[72]*.

2.3.2. Paramagnetism

Atoms in a paramagnetic materials are characterized by an intrinsic non-zero magnetic moment and in the absence of an external field, the orientation of magnetic moments in the material are randomly orientated, resulting in a zero net magnetic moment [71, 73]. In the

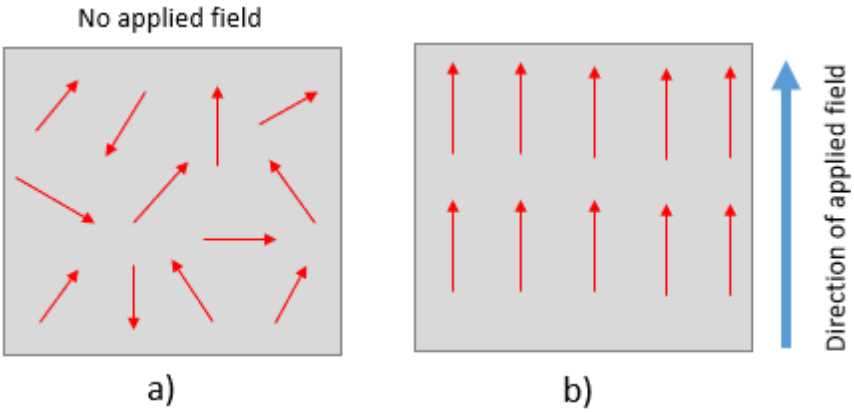
presence of an external magnetic field, magnetic moments try to align in the direction parallel to the applied field as shown in Figure 21 (b) which results in a positive magnetic susceptibility [36, 71].

As the temperature increases, the magnetization of the material decreases as it becomes harder to align the magnetic moments due to thermal agitation and hence the paramagnetic effect and magnetic susceptibility decreases, this is illustrated in Figure 21 (c) [70, 71, 74]. This phenomenon is known as Curie law and is related to the magnetic susceptibility as shown in the equation below,

$$\chi = \frac{C}{T} \tag{2.20}$$

where C (a material-specific constant) is known as the Curie constant.

This law indicates that the magnetic susceptibility of paramagnetic materials is inversely proportional to temperature (magnetism of the material increases with a decrease in temperature) [75].



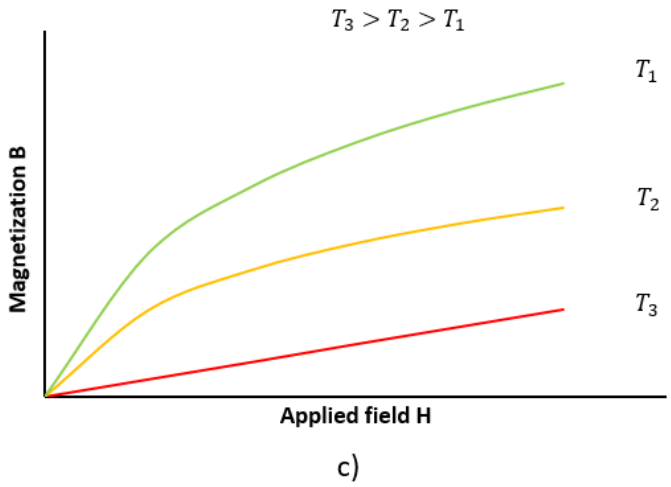


Figure 21: Atomic dipole arrangement in paramagnetic materials: a) disordered arrangement when no field is applied and b) when an external field is applied. c) shows the magnetic field dependence of a paramagnetic material indicating that an increase in temperature causes the dependence of magnetization on the applied field to become linear *[74, 76]***.**

2.3.3. Ferromagnetism

This form of magnetism occurs when materials possess permanent magnetic moments even in the absence of an external field and is only possible when atoms are arranged in a lattice where magnetic moments interact to align parallel to one another, in the same direction creating a permanent magnetic field [70, 71]. When an external field is applied, the magnetization of the material increases until saturation is reached. Below the Curie temperature T_C, the electron spins are aligned and parallel (see Figure 22) [75].

As these materials are heated well above the Curie temperature, the degree of alignment of the magnetic moments decreases and the saturation magnetization also decreases eventually the thermal agitation becomes dominant and the material becomes paramagnetic [70]. These have a high susceptibility and above the Curie temperature the susceptibility varies according to the Curie-Weiss law [71]:

$$\chi = \frac{C}{T - \theta} \tag{2.21}$$

where C is the Curie constant, T is the temperature and θ is the Weiss constant.

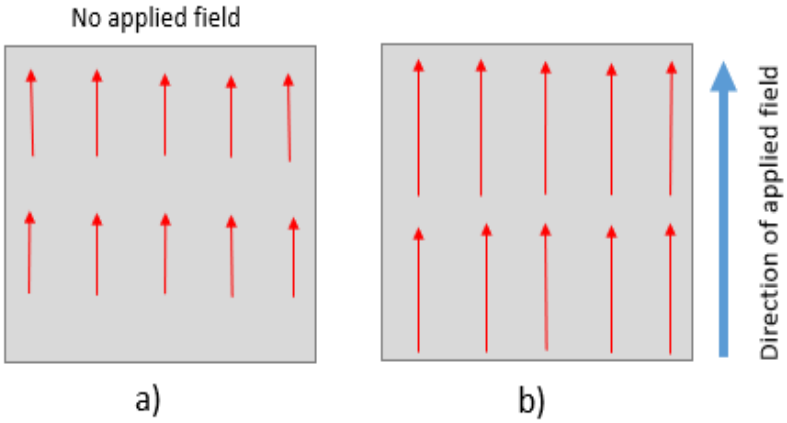


Figure 22: Atomic dipole arrangement in the absence a) and presence b) of a magnetic field. The direction of red arrows indicates the direction of the induced field and size reflects strength. *[76]*.

While studying the magnetization behaviour of ferromagnets under the influence of an applied field it is observed that when the applied magnetic field is increased from zero to a certain value and reduced back to zero again, *M* does not follow the same path. This irreversibility of the magnetization of ferromagnets is known as hysteresis [73]. Hysteresis refers to the lag of magnetization behind the magnetizing field, this is seen in ferromagnetic materials when temperatures are below the Curie temperature [72]. Ferromagnets are capable of retaining a certain amount of magnetization after the applied field has been removed as shown by the model hysteresis loop below [77]. The curve is obtained experimentally and it describes how materials behave when the strength and direction of an applied field is changed [78].

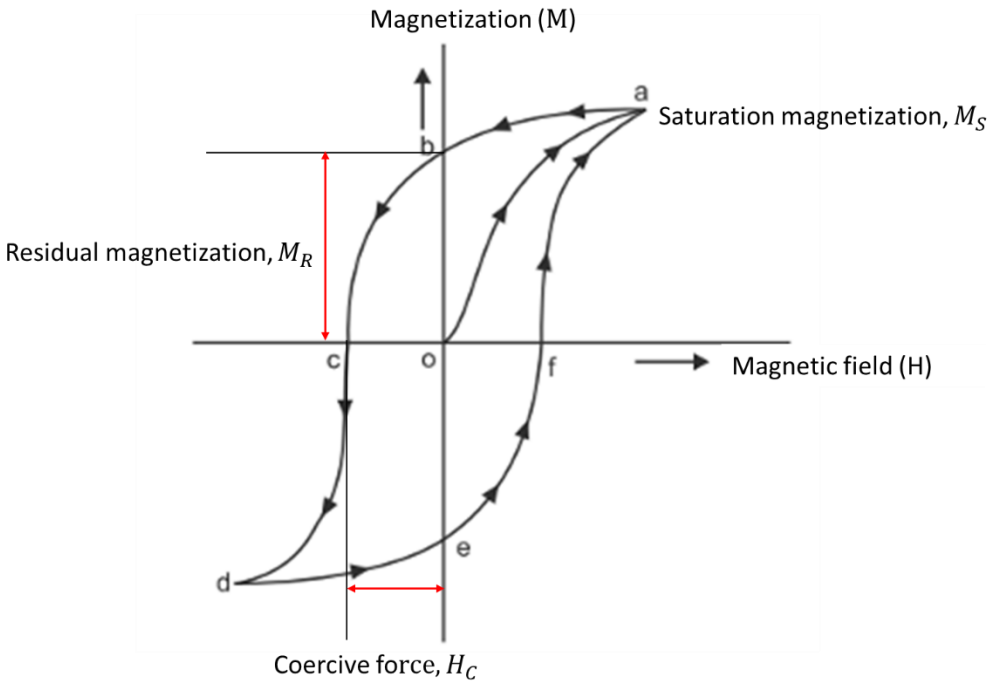


Figure 23: Hysteresis curve showing the variation of the magnetization of ferromagnetic materials with magnetic field *[79]*.

Description of different regions of the hysteresis curve:

o-a: The magnetic material starts at zero in an unmagnetized state. When a magnetizing force is applied and increased in the positive direction, the flux density *B* also increases until a point when magnetic saturation is reached (b) [80]. This is where the graph levels off since all magnetic domains are perfectly aligned.

a-b: When the magnetizing force is reduced to zero, the flux density reduces to a non-zero value (c). The magnitude **ob** represents the retentivity of the material and this is the amount of magnetic field retained in the material after the removal of an external field *[72]*.

b-c: The magnetizing force is increased in the reverse direction; the flux density decreases to zero (d). The magnitude **oc** is called the coercive force and it represents the magnetizing force required to reduce the flux density to zero in a saturated ferromagnetic material [72, 79].

c-d: Further increase in H leads to magnetic saturation (in the reverse direction) of the material [80].

d-f: Reduction of H to zero will decrease the flux density to point (e). Applying the magnetizing force in the original direction will further reduce the flux density to zero.

2.3.4. Ferrimagnetism

Ferrimagnetic materials are magnetic in the absence of a magnetic field and consist of two different ions with magnetic moments that are arranged antiparallel to each other. An atoms' magnetic moment is facing in one direction with a specific magnitude and the other atoms' magnetic moment is directed in the opposite direction with a different magnitude as shown in the Figure 24 [75]. The difference in magnitude of the magnetic moments results in spontaneous magnetization and a net magnetic field is present in the material. When the material is in the presence of a magnetic field, the larger of the two moments in the material will align in the direction of the applied field and the one with a smaller magnitude in magnetic moment will align in the opposite direction [73]. In this case, a large resultant magnetic moment is observed in the direction of the applied field.

Just like ferromagnetic materials, the magnetic susceptibility of these materials is positive and is dependent on temperature [72]. Above the Curie temperature, ferrites become paramagnetic.

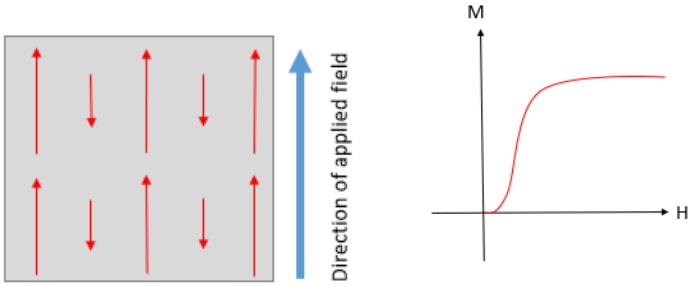


Figure 24: Spin dipole interaction of a ferrimagnetic material in the presence of a magnetic field (left) and the dependence of magnetization (*M*) on the magnetic field strength (*H*).

2.4. Specific heat of metals

2.4.1. Theory of heat capacities

The heat capacity of a material is the amount of heat required to increase the enthalpy of a material by a unit degree of temperature [81, 82]. Physical properties such as heat capacity which involve heat and work are governed by the fundamental laws of thermodynamics. According to the first law of thermodynamic, if a certain amount of heat dQ is supplied to a system, part of this energy is used to increase the internal energy dE of the system and a part is used to perform external work dW [81].

$$dQ = dE + dW \tag{2.22}$$

Heat capacity is an extensive physical property that can be defined for a specific volume C_V or for a constant pressure C_P [83]. C_V represents an increase in internal energy ∂U of the crystal without doing any mechanical work by altering the volume while C_P indicates an increase in enthalpy ∂H of the system per unit increase in temperature.

$$C_V = \left(\frac{\partial U}{\partial T}\right)_V \; and \; C_P = \left(\frac{\partial H}{\partial T}\right)_P \tag{2.23}$$

For solids, C_V and C_P are approximately the same since the rate at which the volume of a material changes per unit increase in temperature is negligible.

The total heat capacity of a system contains the following contributions:

(a) Phonon heat capacity, C_{lat}

The classical theory states that the molar specific heat of solids at room temperature is constant, with a value close to 3R ($\sim 25 \frac{J}{mol}.K$), and this is known as the Dulong-Petite law [84]. This is based on the fact that the average internal energy of a set of vibrating particles is given by:

$$E = 3N_A k_B T \tag{2.24}$$

where N_A is Avogadro's number, k_B is the Boltzmann constant and T is the temperature expressed in Kelvin hence the expression of heat capacity takes the following form:

$$C_P = \frac{\partial E}{\partial T} = 3N_A k_B = 3R \tag{2.25}$$

This expression does not hold at low temperatures and at room temperature, the expression is an overestimation of the system's heat capacity.

Einstein Model

Einstein is suitable for describing optical phonon modes and is considered a very simple model of the lattice vibrations where the nearest neighbour interactions between atoms are neglected and all atoms vibrate independently of one another but with the same frequency ω_E and obtained the following expression for the molar heat capacity [85]:

$$C_P = 3N_A k_B \left(\frac{\Theta_E}{T}\right)^2 \frac{e^{\theta_E/T}}{(e^{\theta_E/T} - 1)^2} \tag{2.26}$$

where N_A is Avogadro's number, $\Theta_E = h\omega_E/k_B$, with the dimension of temperature is called the Einstein temperature and k_B is Boltzmann's constant.

For $T \gg \Theta_E$ ((i.e. $x \ll 1$), the Einstein heat capacity reduces to $C_P = 3Nk_B$ which is the Dulong Petit law. When $T \ll \Theta_E$ ((i.e. $x \gg 1$), $C_P \to 0$ as $T \to 0$, obeying the third law of thermodynamics. This model works well for the optical (high energy) phonons in a system because 8 these are within narrow frequency bands but fails to quantitatively explain the low temperature behaviour [86].

Debye Model

The Debye model is a method of estimating the phonon contribution to the heat capacity in a solid. Atoms in a crystal lattice cannot vibrate independently and at the same frequency, the correction to the Einstein model is explained by the Debye model where oscillators representing vibrating atoms are not identical and each has its own frequency. The Debye model assumes an acoustic type of lattice vibration (similar to that of sound waves) and is

used for fitting experimental heat capacity data obtained at constant pressure. The total energy of a phonon is given by:

$$U = 9N_A k_B T \left(\frac{T}{\Theta_\mathrm{D}}\right)^3 \int_0^{\Theta_\mathrm{D}/T} \frac{x^3}{e^x - 1}\, dx \tag{2.27}$$

The Debye model expresses the heat capacity at constant volume per mole of atoms in the following form:

$$C_P = \frac{\partial U}{\partial T} = 9N_A k_B \left(\frac{T}{\Theta_\mathrm{D}}\right)^3 \int_0^{\Theta_\mathrm{D}/T} \frac{x^4 e^x}{(e^x - 1)^2}\, dx \tag{2.28}$$

where Θ_D is the Debye temperature determined from heat capacity measurements and $x = \hbar\omega_E/k_B T$.

The assumptions of the Debye model are:

- The system is assumed to be at constant volume throughout the temperature change.
- The crystal is isotropic.
- The model only accounts for acoustic lattice vibrations and does not account for optic lattice vibrations which arise from opposing vibrations of atoms with different masses within the unit cell.

The contribution made by the aforementioned factors to the heat capacity of a material are modelled by including an Einstein to the fit function.

The high and low-temperature limits of the integral equation can be assessed in the following form:

- For high temperatures, $T \gg \Theta_D$, x takes up a very small value and applying the approximation $e^x \approx 1 + x$, the equation reduces to:

$$U = 9N_A k_B T \left(\frac{T}{\Theta_\mathrm{D}}\right)^3 \int_0^{\Theta_D/T} x^2\, dx = 3N_A k_B T \tag{2.29}$$

$$C_P = \frac{\partial U}{\partial T} = 3R \tag{2.30}$$

where C_P approaches $3Nk_B = 3R$, as predicted by the Dulong-Petit law.

- For very low temperatures $T \ll \Theta_D$, the integrand in equation 2.28 tends towards zero and upper limit of the integral can be extended to infinity:

$$\int_0^{\infty} \frac{x^3}{e^x - 1}\, dx = \frac{\pi^4}{15} \tag{2.31}$$

$$U = 9N_A k_B T \left(\frac{T}{\Theta_{\mathrm{D}}}\right)^3 \times \frac{\pi^4}{15} \tag{2.32}$$

C_P approximates to:

$$C_P = \frac{12\pi^4}{5} N_A k_B \left(\frac{T}{\Theta_{D,}}\right)^3 \tag{2.33}$$

At low temperatures, the specific heat at constant volume is proportional to the cubic power of the temperature [85]:

$$C_P \propto \beta T^3 \tag{2.34}$$

The Debye model provides higher C_P at lower temperatures than the Einstein model. This is because the Einstein model only uses one frequency which makes excitation of modes at low temperatures difficult. The Debye model is also more accurate than the Einstein model in the low-temperature range where it has been found that C_P is nearly proportional to T^3 [87].

(b) Electronic heat capacity, C_{el}

Conduction electrons in metals are treated with Fermi-Dirac statistics which allows for two electrons with opposite spins at a specific energy level. The contribution of these electrons

is similar to that of the free electron gas where there are no interactions between electrons [88]. The expression for the electronic specific heat is given by:

$$C_{\mathrm{el}} = \gamma T \tag{2.35}$$

where $\gamma = \left(\frac{\pi^2}{3}\right) D(E_F) {k_B}^2$ is known as the Sommerfeld coefficient and $D(E_F)$ is the density of states for both spin directions at the Fermi energy. The electronic contribution is small at room temperature but becomes significant at low temperatures.

Therefore, the total heat capacity of a system is given by the sum of electronic and phononic contributions and obeys the following form [89]:

$$C_P(T)_{T\to 0} = \gamma T + \beta T^3 \tag{2.36}$$

The electronic heat capacity represents the linear part whereas the lattice heat capacity is proportional to T^3. At low temperatures, phononic contributions vanish faster than electronic contributions [90]. By plotting ${C_P(T)}/{T}$ versus T^2 at low temperatures, it is possible to determine the values of β (as the slope) and γ (as the y-intercept) of the resulting straight line. The value of β can subsequently be used to find the value of θ_{D} with the following expression:

$$\Theta_{\mathrm{D}} = \left[\frac{12\pi^4 NR}{5\beta}\right]^{1/3} \tag{2.37}$$

2.5. Electrical Resistivity and Magnetoresistance

Resistivity, ρ describes how strongly a material opposes the flow of charge and is dependent on the size and shape of a material [89]. In a metal, the electrical resistivity decreases as the temperature decreases, in superconductors, the resistance decreases to zero when the material

is cooled below its critical temperature. At room temperature, the resistivity of a material is dominated by the collisions of conduction electrons with phonons but as the temperature is decreased, collisions with lattice imperfections and impurity ions are dominant [91].
A conductor with length, *L* and cross-sectional area, *A* has resistance:

$$R = \frac{L}{A} \times \rho \tag{2.38}$$

The total resistivity of a material consists of resistivity due to:

1. Residual resistivity, ρ_0 which is the resistivity of a metal at absolute zero and is independent of temperature [92]. This results from deformation/impurities in the sample which distort the periodicity of the lattice and serve as scattering centers for conduction electron, hence increasing resistivity within the material [91, 93].
2. Thermal contributions, $\rho(T)$ which is the temperature-dependent resistivity and result from the scattering of conduction electrons from thermally excited lattice vibrations [73].

Bloch-Grüneisen model

The temperature-dependent behaviour of electrical resistivity due to the scattering of conduction electrons by acoustic lattice vibrations (electron-phonon scattering) is described by the Bloch-Grüneisen model:

$$\rho(T) = 4\mathcal{R}\left(\frac{T}{\Theta_R}\right)^5 \int_0^{\Theta_R/T} \frac{x^5}{(e^x-1)(1-e^{-x})}\,dx \tag{2.39}$$

where

$$\mathcal{R} = \frac{\hbar}{e^2}\left[\frac{\pi^3(3\pi^2)^{1/3}\hbar^2}{4n_{cell}^{2/3}aMk_B\Theta_R}\right]$$

is a material dependent scale factor that is independent of *T*, Θ_R is the Debye resistivity temperature, $\hbar$ is Planck's constant divided by 2π, e is the elementary charge, n_{cell} is the

number of conduction electrons per atom, a = (volume/atom)$^{1/3}$, M is the atomic mass and k_B is the Boltzmann constant. These variables map up a monatomic metal with arbitrary crystal structure onto a simple cubic lattice with one atom per unit cell of lattice parameter, a [94]. The effective resistivity of a crystalline metallic specimen is the sum of ρ_0 and (T) and is therefore described by the following expression known as Matthiessen's rule [95]:

$$\rho(T) = \rho_0 + \rho_{BG}(T) \tag{2.40}$$

Scattering among electrons generates a distinct contribution to electrical resistivity that follows a quadratic temperature dependence of T^2. The resistivity of certain metals increase with temperature following $\rho(T) = \rho_0 + AT^2$, where ρ_0 is attributed to impurity scattering while the coefficient of T^2, A (Ω m/K^2) is attributed to electron-electron scattering.

The application of an external magnetic field enables the magnetic force experienced by the moving charges to increase the number of collisions between charges hence increasing the resistance of a material. This dependence of resistance on the magnetic field is referred to as magnetoresistance and is described as the property of a material where it changes the value of its electrical resistance when an external field is applied to it [5]. This is described by the following expression:

$$MR = \frac{\Delta\rho}{\rho_0} = \frac{\rho(T,H) - \rho_0}{\rho_0} \tag{2.41}$$

Chapter 3

Experimental Techniques

This chapter describes how the samples under investigation were synthesized and prepared for analysis. The experimental techniques such as X-Ray diffraction, Mössbauer Spectroscopy (in transmission mode) and the Physical Property Measurement System (PPMS) were used to investigate the materials' structural, magnetic and electrical properties are also discussed. A detailed description of the equipment and apparatus used will also be presented.

3.1. Sample Preparation

3.1.1. Sample Synthesis and Annealing

The samples were synthesized using the arc-melting furnace where an arc plasma was used to melt the pure constituent elements of each compound. With the aid of a vacuum pump, the air inside the chamber was extracted and then flushed with high purity argon gas. This process was repeated several times to create an inert atmosphere. Sufficient heat was supplied to the samples to ensure that those elements with a higher melting temperature reacted with other elements. The melting process was repeated several times to achieve a homogenous single-phase sample. The sample was allowed to cool and then weighed to determine the mass loss during melting. The mass loss expressed as $m_{\text{before}} - m_{\text{after}}/m_{\text{after}}$ (where m_{before} is the mass of the constituent elements before melting and m_{after} is the mass of the sample after annealing) was $\sim 0.15\%$. A complete list of samples synthesized is given in the Table 5.

Table 5: A list of samples synthesized by arc melting.

no	compound
1	$RuFe_3Si$
2	$RuFe_3B$
3	$RuFe_3C$
4	$RhFe_3B$
5	$RhFe_3C$
6	$PdFe_3Si$
7	$PdFe_3B$
8	$PdFe_3C$

The synthesized materials were weighed, inserted into a quartz tube and a constriction was made on the tube. Figure 25 shows the tube sealing unit used to prepare samples for annealing. The air inside the tube was extracted using a vacuum pump and then flushed with high purity argon gas. The constriction made was quickly sealed and the samples were placed in ceramic crucibles before being placed in the furnace as shown in Figure 26. The samples were annealed at 1000 °C for several days. After the annealing process, the samples were left to cool in the furnace. Annealing was done to improve the crystallinity of the sample and also to drive the formation of desired crystal types.

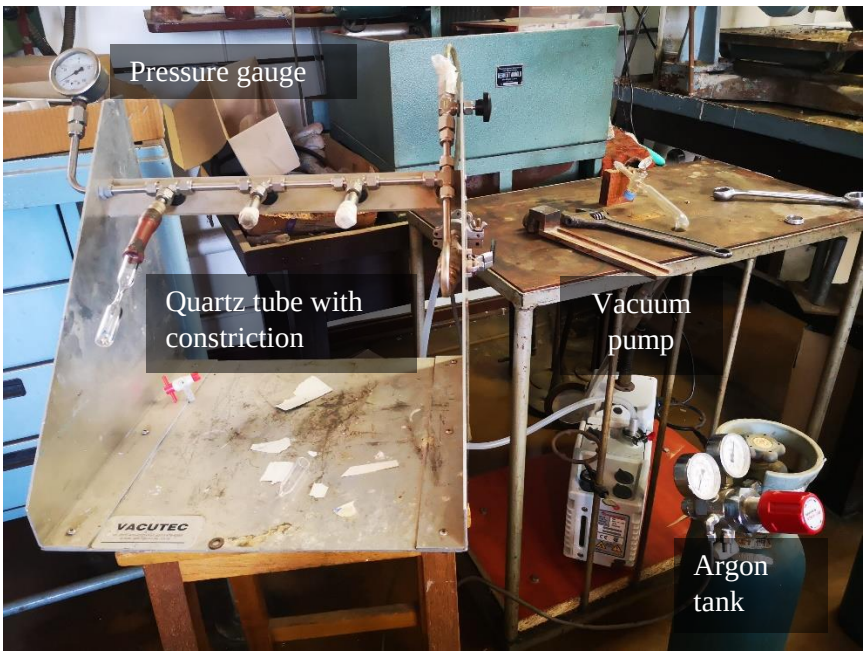


Figure 25: Picture showing the tube sealing unit consisting of a vacuum pump, a tank with argon gas and gas inlet pipes.

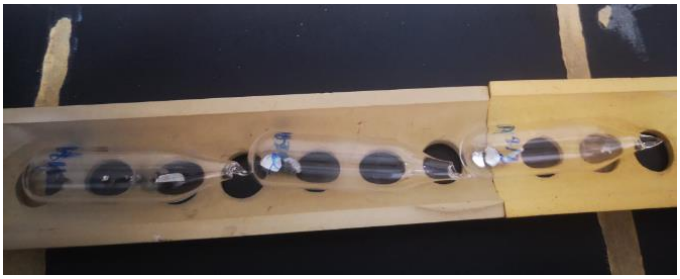


Figure 26: Sealed quartz tubes placed on ceramic crucibles before being placed in the furnace for annealing.

3.1.2. Cutting

A wire saw was used to cut the samples to specific dimensions for the different experiments. The sample was glued on the sample holder with a double-sided tape. A wire saw which uses a continuous loop of wire rotating on two wheels was used to cut the samples. The main components of the saw are shown in Figure 27:

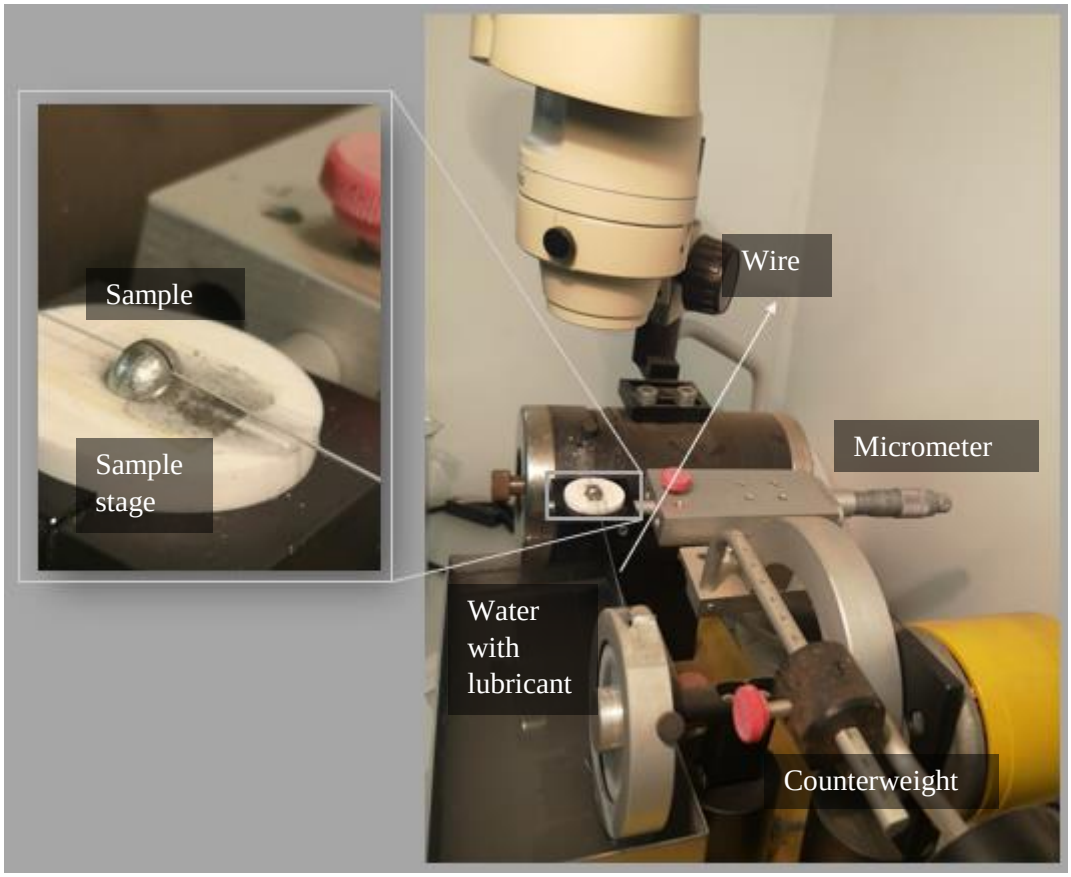


Figure 27: Picture showing the main components of a wire saw used to cut the samples.

1. Sample stage – provides a platform on which the sample is glued using double-sided tape.
2. Counterbalanced arm – has weights that allow for adjustments in cutting pressure [96].
3. Micrometer – used for precise positioning of the sample.
4. Wire – diamond-impregnated to allow for smooth cutting of the sample.
5. Water reservoir – acts as a lubricant and a coolant while the wire cuts the sample.

Following the cutting process, the samples were immersed in acetone and cleaned with an ultrasonic cleaner to dissolve any adhesive residue from the glue and to remove any residue from the saw. One half of the sample was ground for XRD and Mössbauer measurements while the remaining sample was cut into different shapes to be used for the physical property and magnetic measurements.

3.1.3. Grinding

Mössbauer and XRD measurements were performed on powdered samples which were obtained by the grinding process using an agate pestle and mortar as shown in Figure 28. The analysis of samples by powder X-ray diffraction requires fine ground samples to minimize preferred orientation of grains. Grinding also increases the number of particles present in the sample which increases the chance of equal representation for all possible crystal orientations during XRD measurements [97].

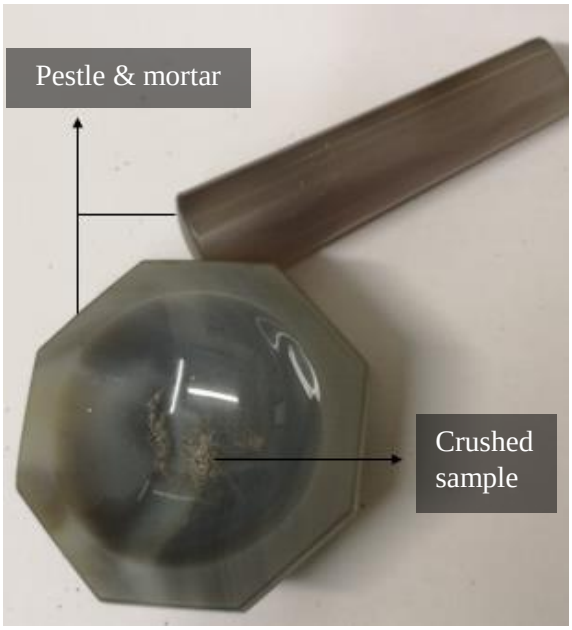


Figure 28: Pestle and mortar used to grind the samples to powder.

3.2. Structural and Compositional Characterization Techniques

3.2.1. Electron Probe Micro-Analysis (EPMA)

To identify and measure the elemental composition on a microscopic level, an electron microscope was used. This method uses an electron beam to excite characteristic X-rays on the surface of a sample and provides information about the distribution and concentration of elements over the surface of the sample [98]. An electron beam is focused on the surface of the sample and interacts with it to generate characteristic X-rays, backscattered electrons and secondary electrons. The characteristic X-rays are detected at specific wavelengths and their

intensities measured to determine their concentrations. All these interactions can be analysed through Wavelength Dispersive Spectroscopy (WDS), Energy Dispersive Spectroscopy (EDS) and Scanning Electron Microscopy (SEM) [98, 99]. Wavelength Dispersive Spectroscopy is based on Bragg's law and used to determine the composition of a sample. WDS has high spectral resolution and provides a more accurate quantitative analysis of light elements, particularly those with atomic numbers lower than oxygen [100].

3.2.2. Beam-Sample interactions

Primary electrons in the incoming beam interact with atoms of the sample, producing signals which are detected by the surrounding detectors (see Figure 29). These signals contain information about the topography, elemental composition and electrical properties of the sample [101].

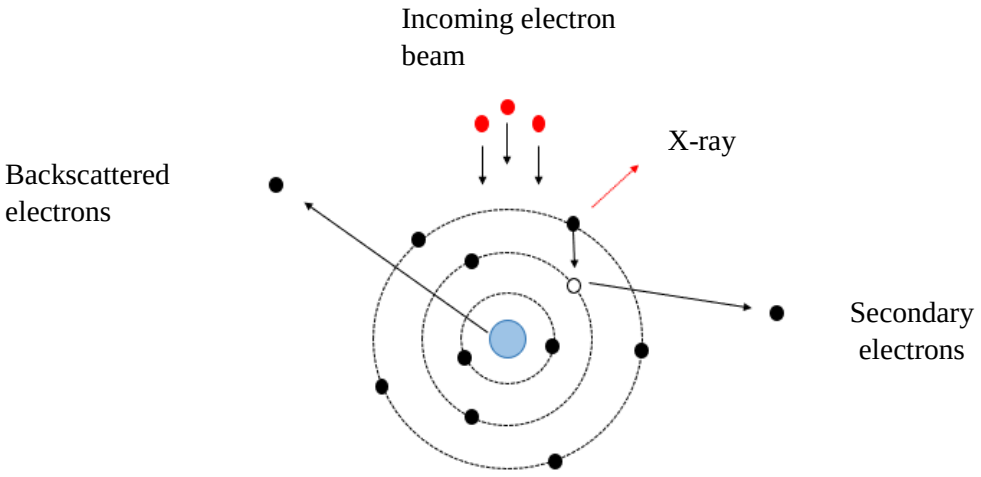


Figure 29: An illustration of different interactions of electrons with matter.

As the electron beam travels down the column, it is focused by electromagnetic lenses to a small spot on the surface of the samples. As the beam impinges on the sample, it penetrates the sample. The depth at which it penetrates depends on the atomic number of the sample (samples with a low atomic number tend to experience a greater depth of penetration) and the acceleration of the incident beam (high accelerating voltage results in greater penetration) [100]. The incoming electron beam can interact with the atoms in the sample in one of the following ways:

1. The incoming electron excites electrons in the sample which are then ejected from the outer (not strongly bound) atoms in the sample. These types of electrons have low energy and are called secondary electrons. Images produced from these electrons give us information about the topography (surface) of the sample [102].
2. Incoming electrons can collide with heavier nuclei of atoms in the sample and bounce back. These are called backscattered electrons. The intensity of the backscattered electrons increases with increasing atomic number, bright portions in images are associated with high atomic number elements while surfaces with lower atomic numbers appear darker [101].
3. The incoming electron can lose some of its kinetic energy while interacting with atoms in the sample. The ejection of a core electrons from the nucleus of an atom leads to the production of characteristic X-rays [99]. This interaction can give information about the types of elements present in specific portions of the sample.

3.2.3. Sample Preparation

The samples ($RuFe_3Si$ and $RhFe_3C$) were embedded in epoxy resin with a 1-inch diameter and were later polished to expose the surface of the samples. To obtain a smooth surface, they were polished on a cloth using an electronic polishing machine with the aid of diamond paste (with 1-micron grains) as an abrasive. The polished samples were subsequently sputter coated to promote conductivity and to prevent electrostatic charging during the WDS measurement.

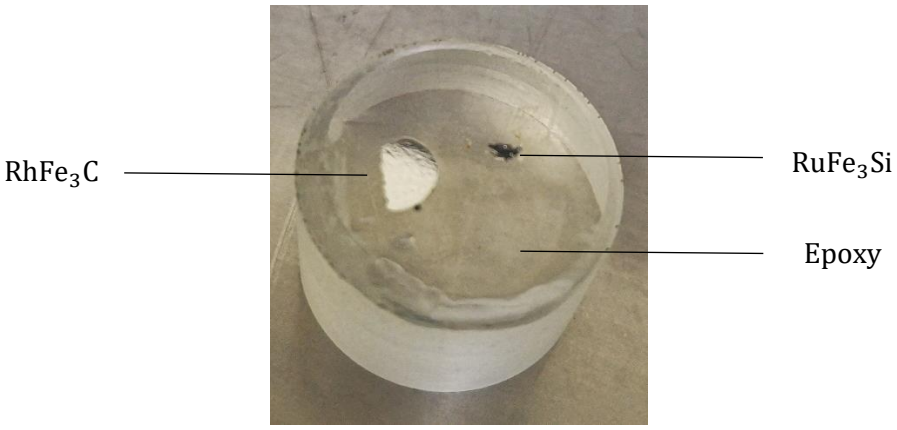


Figure 30: $RuFe_3Si$ and $RhFe_3C$ with exposed sample surface mounted in epoxy.

3.3. Instrumentation

3.3.1. Electron Probe Micro-analyser and its main components

The Wits Microscopy and Micro-Analysis Unit (MMU) has the CAMECA SX5-FE EPMA to be used for qualitative and quantitative analysis of different samples. The analysis was performed with the WDS option. The instrument consists of a column, detectors and a sample stage, shown in Figure 31. The column is kept under vacuum and consists of the following:

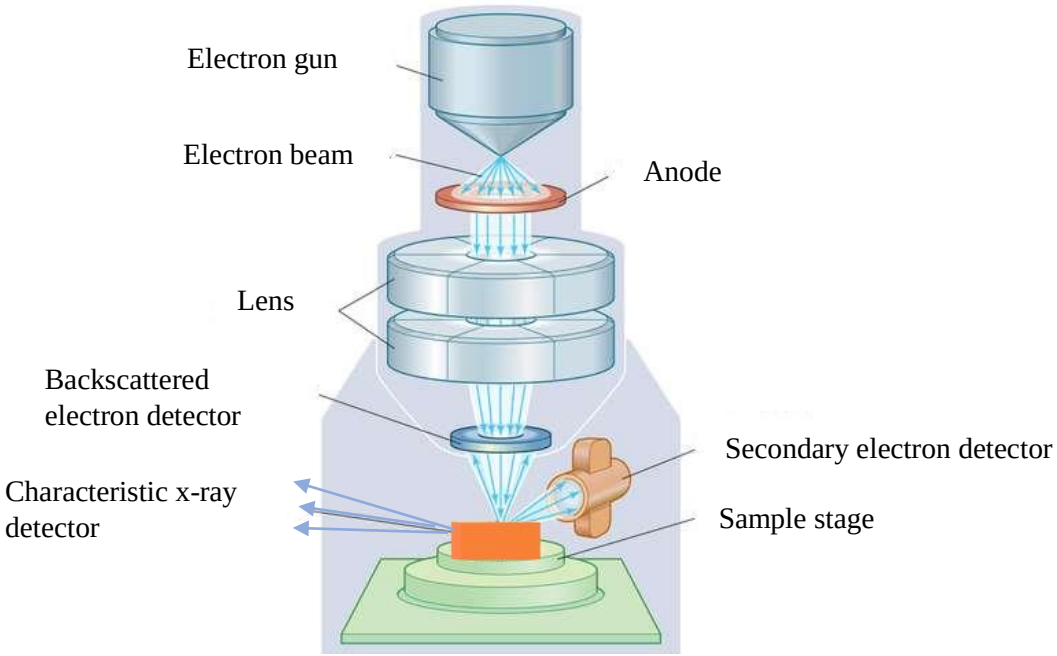


Figure 31: Schematic of an Electron Probe Micro-analyser and its main components *[99]*.

1. Electron gun which produces an electron beam and accelerates down the column.
2. A series of electromagnetic lenses assist to focus and control the size/diameter of the beam.
3. Detectors collect the signal from the different interactions of electrons with the sample. These signals are converted into digital images which are then displayed on the monitor [101].

3.3.2. Powder X-Ray diffraction

To investigate the properties of alloys, it is important to identify their crystal structure by performing X-ray diffraction (XRD) measurements. For this work, Powder X-ray diffraction performed at room temperature was used for a detailed analysis of the structure, phase and composition of the samples. In this study, a Bruker D8 diffractometer shown in Figure 32, utilizing Mo radiation with a wavelength of 0.7107 Å was used for XRD as the radiation source.

In powder X-ray diffraction (XRD) the following steps were followed to prepare the sample for diffraction measurements:

- The polycrystalline sample was ground into a fine powder in an agate mortar. Grounding the sample ensures that it has many crystallites that are randomly orientated.
- The powder was transferred to a silicon sample holder, the powder was then pressed down using a glass slide. This is done to ensure the powder is all at the same level to encourage a high degree of diffraction.
- The glass slide was then mounted and irradiated with an X-ray beam while rotating with respect to the detector. Rotating the sample ensures that the sample is scanned through a range of 2θ angles, in this way all possible directions in which the beam can be diffracted are attained [103].

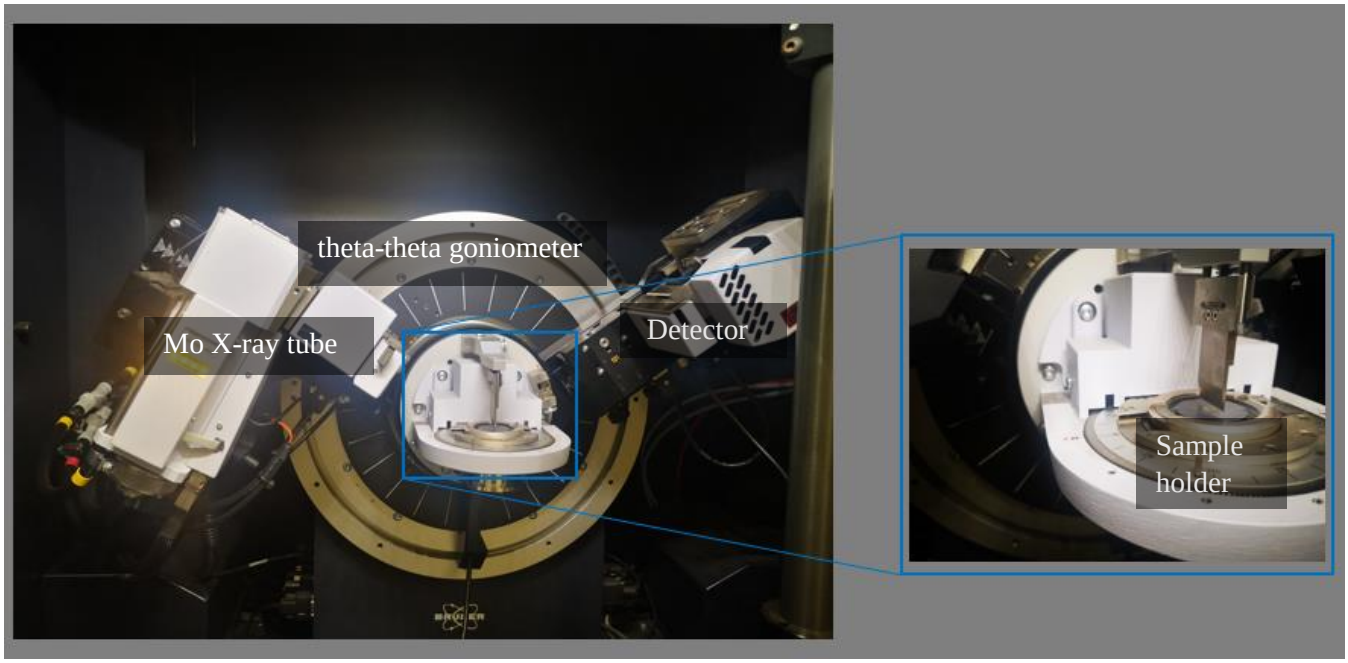


Figure 32: D8-Advance BRUKER diffractometer with its main components.

The diffractometer operates in the Bragg-Brentano geometry where the detector and sample are rotated in such a way that the detector remains at an angle 2θ and the sample surface is kept at an angle θ to the incident beam [104]. The essential components of a diffractometer include:

- X-ray tube where monochromatic X-rays are generated
- Beam optical devices are located between the source and sample and between the sample and detector. These collimate and direct the X-ray beam towards the crystalline sample and also play a role in limiting scattered radiation and reducing background noise [105, 106].
- A sample platform/holder
- An X-ray detector counts the number of X-rays scattered from the sample [105].

All these components are arranged in the following geometry where a beam from an X-ray tube is incident on a sample, then diffracted and passed through a slit to the detector [103].

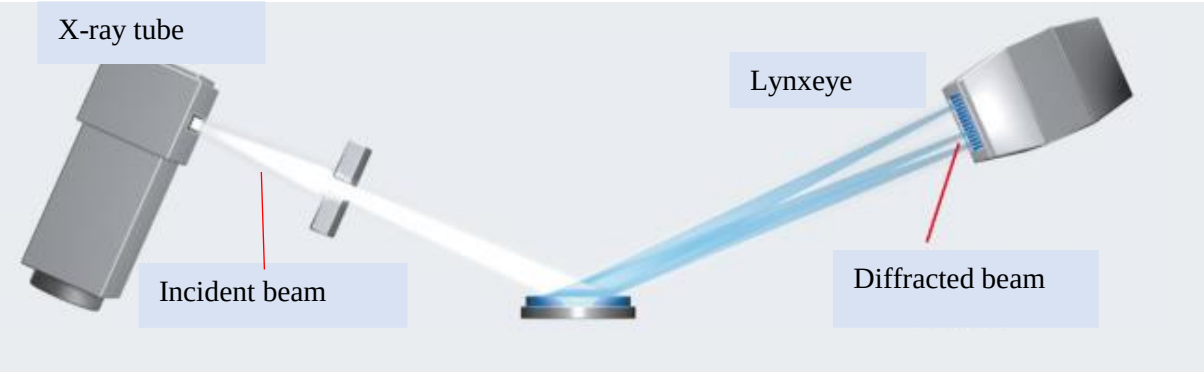


Figure 33: Picture showing the arrangement of the main components of a diffractometer with a Lynxeye detector in the Bragg Brentano configuration *[107]***.**

The diffracted beams strike the detector and the intensity of the diffracted beam as a function of the angle is recorded. The diffraction peaks are produced when monochromatic X-ray beams interfere constructively (i.e. this occurs when the reflections from the parallel planes of atoms are in phase) [47]. Peak intensities are recorded as counts and give us information about the distribution of atoms in the lattice [105, 103]. The peaks appear as a result of the distribution of atoms within the lattice (i.e. the diffraction pattern obtained is the fingerprint of periodic atomic arrangements inside the material) [13]. A typical XRD pattern is shown in the Figure 34.

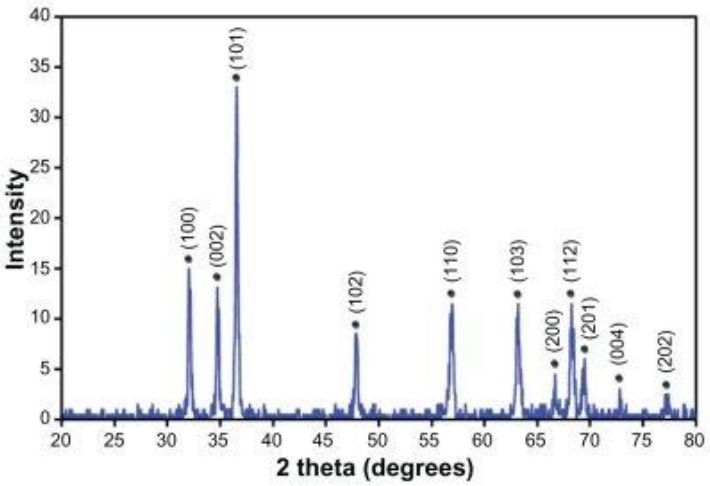


Figure 34: Illustration of a typical diffraction pattern obtained from ZnO nanoparticles, the peaks are indexed with Miller indices *[108]***.**

Rietveld refinement [109, 110] technique can be used for the analysis of neutron as well as X-ray diffraction (XRD) data collected on powder samples of crystalline materials. The

intensity and position of the Bragg reflections obtained in a diffraction experiment can be used to model and determine the details of the crystal structure of the material under consideration. The Rietveld method uses a least-square fit approach to fit the measured profile with a theoretical line profile. A successful refinement obtained on powder diffraction data provides information about crystal class, space group, atomic positions, lattice parameters as well as antisite disorder (if any) of the material.

We have used the FullProf suit package [111] to perform the Rietveld refinements on the powder XRD data of our samples. The program has been mainly developed for Rietveld analysis of powder XRD data as well as nuclear and magnetic scattering obtained in powder neutron diffraction data collected at a constant or variable step in scattering angle 2θ. The program can be also used as a Profile Matching tool where the knowledge of the structure is not essential.

The analyses of the XRD data were performed in two steps. In the first step, we performed a profile matching fit to obtain the crystal class and approximate lattice parameters. In the second step, a complete Rietveld refinement was performed. The lattice parameters obtained in the first step were used as the initial sample parameters in our fits. Instrumental parameters obtained on a standard sample were used as initial instrumental parameters in the refinement.

Several different atomic arrangements allowed by the space group were systematically investigated to narrow down the goodness of the fit and to reach the crystal structure solution.

Preliminary analysis of the powder XRD patterns obtained from the 8 samples was performed to determine which of the samples had formed a crystalline structure. The analysis revealed that compounds $RuFe_3Si$ and $RhFe_3C$ had formed a desired crystalline structure. Therefore a detailed XRD analysis and analysis by Mössbauer spectroscopy, heat capacity measurements, resistivity measurements and magnetoresistance measurements were only performed on these two compounds.

3.3.3. Transmission Mössbauer Spectroscopy

The ground samples were investigated using Transmission ^{57}Fe Mössbauer Spectroscopy at the Wits Mössbauer lab. The experimental setup for Mössbauer spectroscopy consists of mainly a source, a detector and a Mössbauer drive system which oscillates the source. Resonant absorption is observed by the attenuation of gamma radiation passing through the

absorber (sample), this is referred to as the transmission geometry [56].This is a type of geometry arrangement mostly used for powdered samples where the sample is positioned between the source and the detector. The gamma radiation from the source is transmitted through a thin sample into the detector where it is measured [62]. For this study, α-Fe was used as calibration at room temperature. The basic experimental configurations used in Mössbauer spectroscopy are illustrated in Figure 35 below:

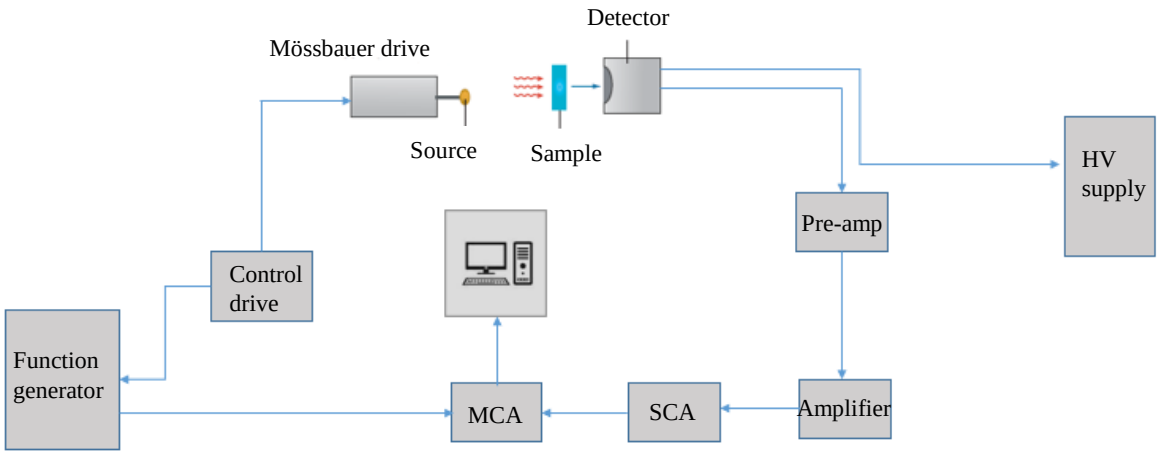


Figure 35: Block diagram of a Mössbauer spectrometer arranged in transmission geometry *[112]*.

The following is a list of Mössbauer spectroscopy components together with their function:

1. Source – a radioactive element that serves as a source for the 14.4 keV gamma radiation required for ^{57}Fe Mössbauer spectroscopy. Radioactive ^{57}Co (with a half-life of 270 days) serves as the gamma radiation source for ^{57}Fe Mössbauer spectroscopy [55]. ^{57}Co decays to an excited state of ^{57}Fe through electron capture, populating the 136 keV nuclear level with nuclear spin $I = \frac{5}{2}$ as shown in Figure 36 [63]. Approximately 9% of the time, the excited nucleus deexcites directly to its ground state by releasing ≈ 137 keV gamma radiation. Otherwise, decay can occur in two stages: firstly the transition from the first excited state to the second excited state by emitting 123 keV gamma ray, then from the second excited state to by emitting a 14.4 keV gamma ray [112].

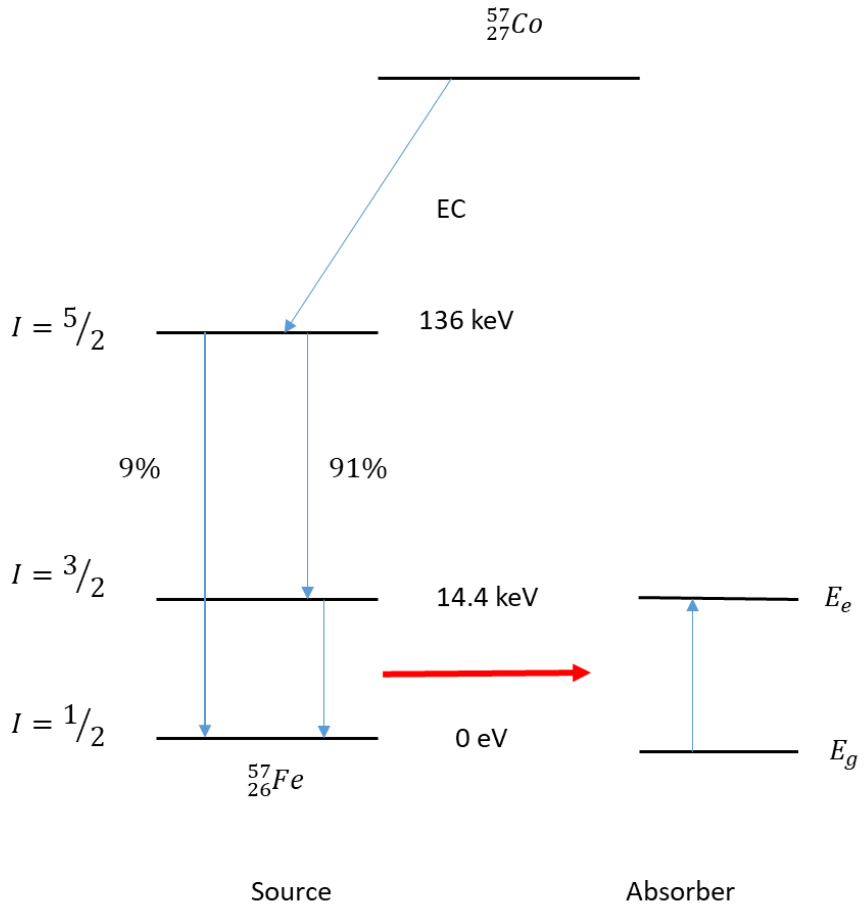


Figure 36: Nuclear decay scheme of ^{57}Fe from ^{57}Co which provides the 14.4 keV gamma radiation necessary for the Mössbauer effect *[113]*.

2. Absorber – sample to be investigated that contains the same Mössbauer nucleus as the source in its ground state [114]. Radiation emitted without recoil is resonantly absorbed by nuclei in the absorber [56].

3. Mössbauer drive – a device that uses an electrical signal to generate mechanical motion of the source relative to the absorber in the direction of the gamma-ray propagation [56]. Moves the source through a range of velocities and oscillates it from -v to +v, producing a Doppler shift on the energy of the radiation released.

4. Waveform generator – used to provide the drive system with a reference signal which determines the waveform [54].

5. Detector – measures the intensity of transmitted rays through the sample.

6. Amplifier – increases the amplitude of the received input signal.

7. SCA – determines whether the height of the input signal between the set limits and if the signal lies outside the set limits, no output signal is given. Otherwise, a pulse is given as an output signal.

8. Counting System – This consists of the pre-amplifier, amplifier, single-channel analyser (SCA) and a multi-channel analyser (MCA). A signal is extracted from the detector by the pre-amplifier, the amplifier then converts it into a signal strong enough for further processing. The signal from the amplifier is fed into the input of SCA where background radiation is rejected and only the signal corresponding to the desired energy is retained [62]. The discriminated signals are then fed into the MCA (operating in Pulse Height Analysis, PHA) mode where they are converted to digital values which are then transferred to a personal computer [56]. The computer generates a spectrum which shows a record of counts *vs* velocity in terms of channel numbers.

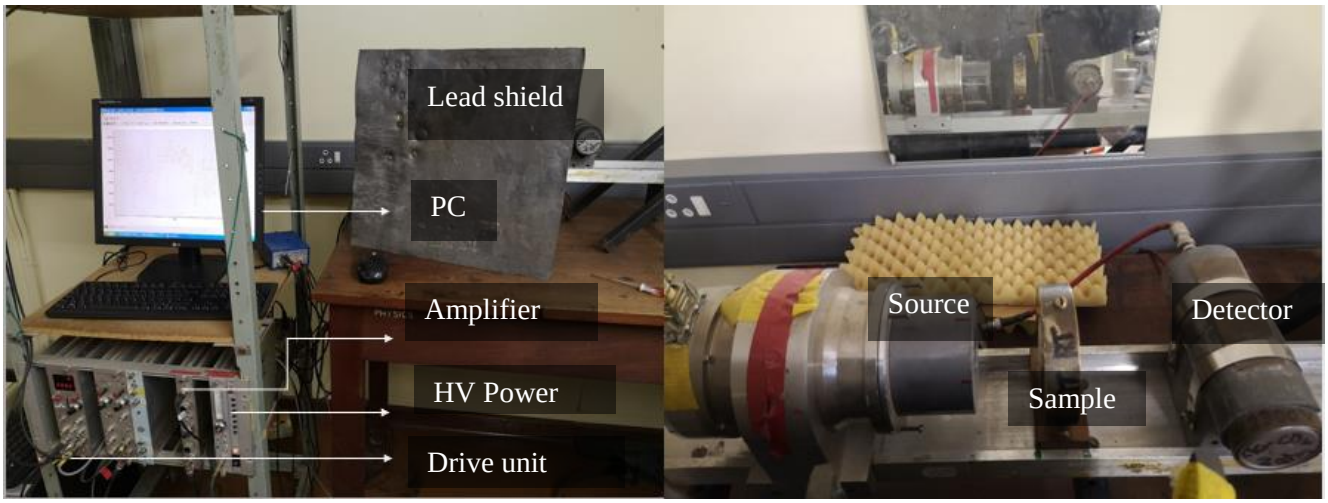


Figure 37: Electronics used in data acquisition (left) and Mössbauer spectroscopy configuration in transmission geometry (right) used for this study

3.3.4. Magnetic and Physical Properties Measurements

The Quantum Design Physical Property Measurement system has different options to measure magnetic, electrical transport and thermal properties. The system allows for measurements in the temperature range from 1.9K to 400K and an applied field strength of up to 9T can be generated. Quantum Design PPMS consists of the following:

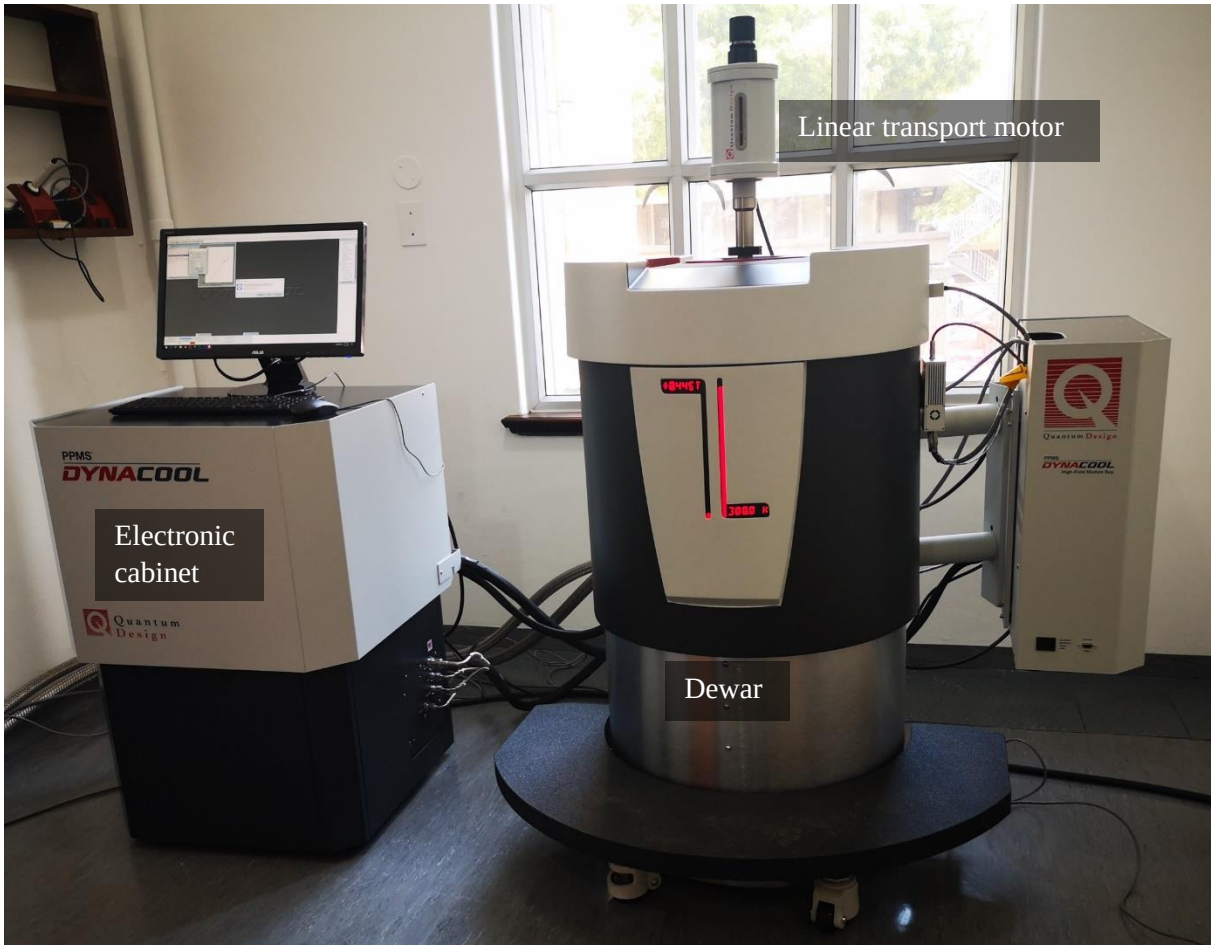


Figure 38: Quantum Design Physical Property Measurement System (PPMS) at Wits University Physics Department.

1. Dewar – this component contains the liquid helium bath and houses the superconducting magnet, the pick-up coils and the sample chamber. Liquid helium is pumped in and cools the magnet and the sample chamber when low-temperature measurements are being carried out.
2. Electromagnet – generated the constant magnetic field used to magnetize the sample.
3. Pick-up coils - electronics used to measure the induced voltage, V_{coil}.
4. VSM linear motor transport – used to vibrate the sample.

3.3.4.1. Magnetic measurements using VSM option

Magnetic measurements were performed on a Quantum Design Physical Property Measurement System (PPMS) using the Vibrating Sample Magnetometer (VMS) technique at Wits university. The sample was cleaned with ethanol to prevent any possible contamination and its mass was measured to be 25.19 mg. During mounting, the sample is placed between two quartz holders, 35mm from the end of the mounting device and secured with teflon tape.



Figure 39: Mounting kit with sample holder.

During the experiment, the sample is placed in a constant applied magnetic field and then set to vibrate sinusoidally [115]. The working theory of the VSM magnetometer is based on Faradays Law which states that induced voltage around a coil is equal to the rate of change of the magnetic flux through an area enclosed by the loop. The changing magnetic flux induces a time-dependent voltage in the coil given by the following expression where Φ is the flux of the coil, z is the position of the sample with respect to the coil, C is the coupling constant, m is the magnetic moment of the sample, A is the amplitude, f is the frequency of oscillation and t is the time [116] :

$$V_{coil} = \frac{d\Phi}{dt} = \left(\frac{d\Phi}{dz}\right)\left(\frac{dz}{dt}\right) = 2\pi CmA\, sin(2\pi ft) \tag{3.1}$$

Rearranging the formula above, the magnetic moment of the sample is proportional to the induced voltage and takes the following form:

$$m = \frac{V_{coil}}{2\pi CmA\, sin(2\pi ft)} \tag{3.2}$$

Ultimately, we can measure the magnetic moment of the sample as a function of different parameters, these include; time *m(t)*, temperature *m(T)* and magnetic field *m(H)* and quantities such as the critical temperature and magnetic saturation can be determined [117]. A schematic for the VSM is shown in Figure 40:

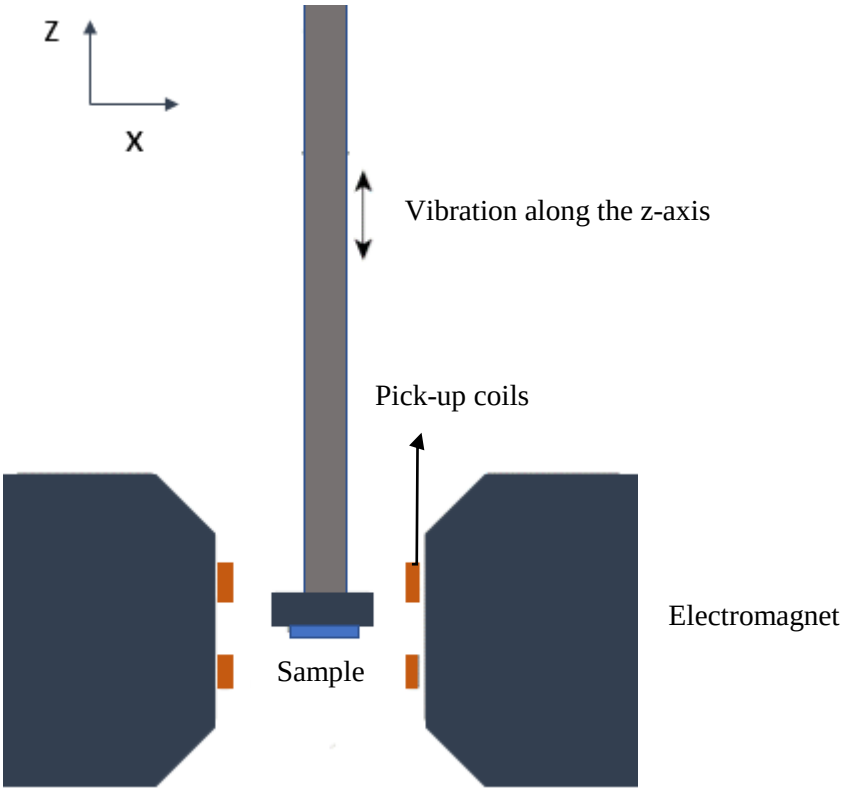


Figure 40: A simplified schematic of a (VSM) *[118]*.

3.3.4.2. Resistivity and Magnetoresistance measurements

Resistivity measurements were conducted on the $RuFe_3Si$ and $RhFe_3C$ samples. The samples were firstly cleaned with ethanol to prepare for electrical contact. For this research, we measured resistivity using the four-probe method with four platinum wires with a diameter of 50µm and length of 1.5cm. A two-component epoxy was used to secure the wires on the surface of the sample with the aid of a microscope, this was later cured at 120° for 15 minutes. This method greatly reduces the contribution of the joints to the resistance that is measured, in this way, it is possible to measure the current and voltage of the sample to a high degree of certainty and thus we can calculate its resistance using Ohms law.

In preparation for sample mounting, the gold-plated base on the sample puck was lined with GE varnish and covered with cigarette paper. The sample was glued on the puck to prevent detachment during measurements then wires were soldered on corresponding channels on the puck which has four leads I^+, I^-, through which current flows and V^+, V^- across which voltage is measured. The electrical connections were tested using a digital multimeter where resistance between two connections was measured and recorded before the sample was inserted into the chamber.

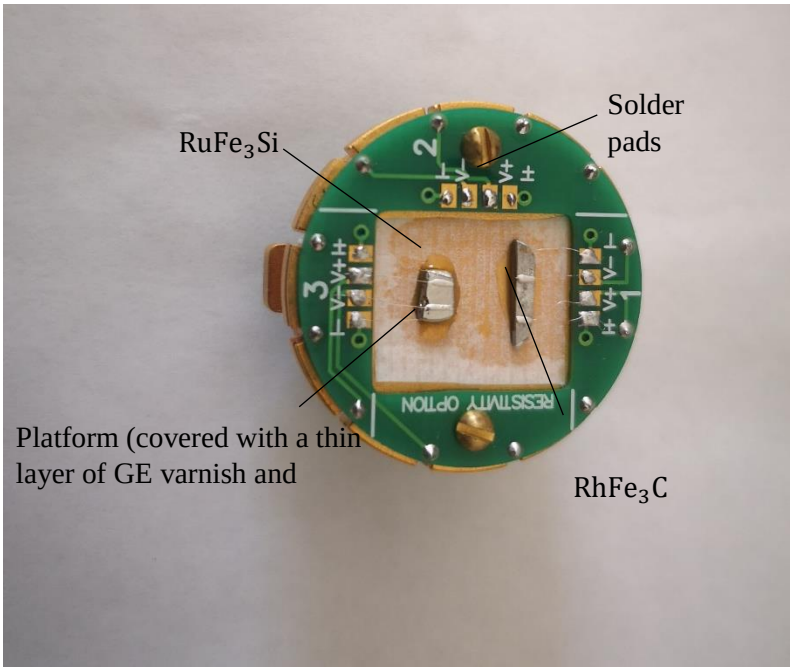


Figure 41: Top view of a resistivity sample puck showing samples mounted for four-wire resistance measurement. RhFe$_3$C is connected to channel 1 and RuFe$_3$Si is connected to channel 3.

DC-resistivity measurements were taken in the temperature range 2 K – 300 K, The electrical resistivity was determined by measuring the potential drop across the length of the sample by passing a known square-wave current through it. The voltage drop across the sample was measured by allowing current to flow from I^+ to I^- and the reading was taken as V_1. The current is then reversed, and the reading is taken as V_2. The voltage drop across the sample is given by $V_{\text{sample}} = \frac{(V_1+V_2)}{2}$. The resistivity is then calculated using:

$$V_{\text{sample}} = \rho \frac{IL}{A} \tag{3.3}$$

where ρ is the resistivity, I is the current flowing through the sample, L is the length between the voltage contact and A is the cross sectional area of the sample.

giving more accurate readings [119]. Readings were taken at zero field and again at 1T. These were used for magnetoresistance measurements which measure the change in resistivity of the samples when a field is applied. Attempts were made to obtain measurements at higher field, each time the wires would detach from the solder pads.

3.3.4.3. Heat capacity measurements

The $RuFe_3Si$ and $RhFe_3C$ samples each weighing 14.7 mg and 16.84 mg respectively, were cleaned with benzene with the aid of an ultra-sonic cleaner to remove any dirt before mounting them on the puck.

Sample mounting station

The sample mounting station uses a pipe connected to a vacuum pump to stabilize the sample platform while mounting. When the arm is in the hold position (see Figure 42), the vacuum pipe grips the sample platform downwards, securing the puck firmly in place. This prevents any damage to the thin connecting wires. The sample is mount on the platform with the aid of Apiezon N-grease (used for room temperature measurements) to hold it in place.

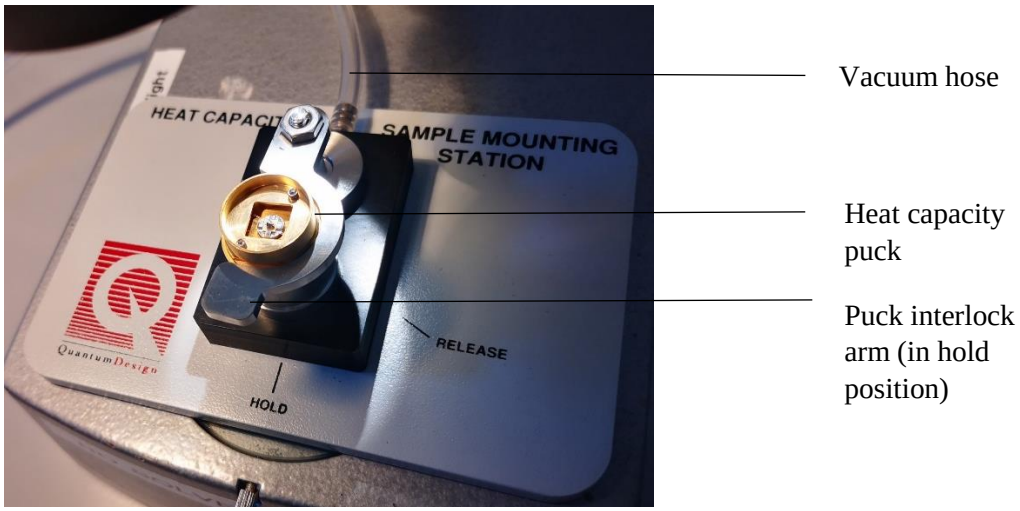


Figure 42: Picture of the heat capacity sample mounting station

The platform on which the sample is placed is orientated in a way that the heater and thermometer are positioned at the bottom. The platform is suspended on eight wires, which provide electrical connection to the heater and thermometer and provide mechanical support to the platform.

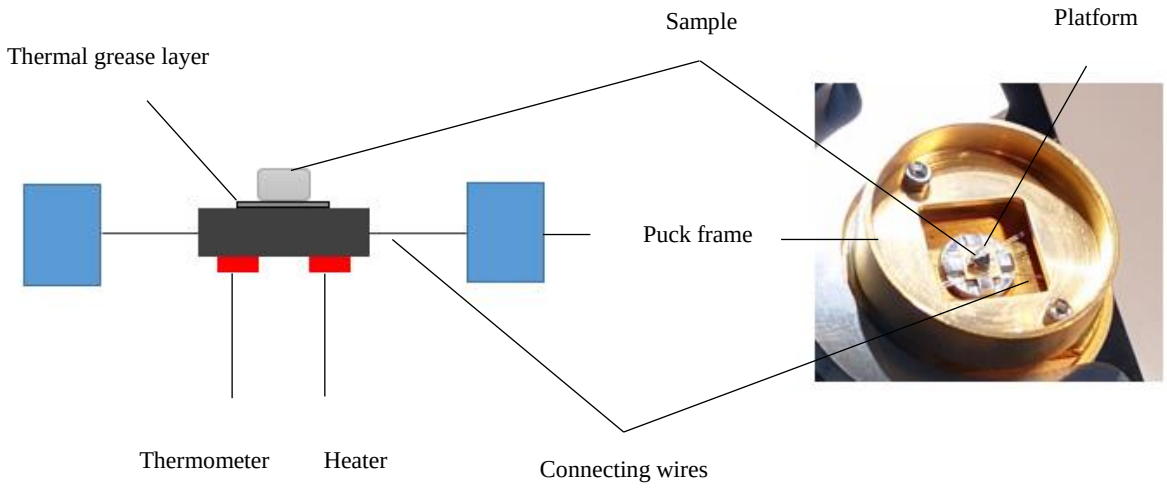


Figure 43: Illustration of a heat capacity sample puck with the sample mounted on the platform *[120]*.

Once the mounting is complete, the puck is installed in the extraction tool and inserted in the chamber, followed by the contact baffle (Figure 44). The contact baffle aids in achieving a uniform thermal environment for the puck and also has a charcoal holder installed which assists in achieving a high vacuum state in the chamber. The complete heat capacity experiment requires two separate measurements, firstly the addenda measurement (heat capacity measurement of the platform and grease only) and secondly measurements with the sample mount on the platform. This is done to separate the sample's heat capacity contribution from the total heat capacity measured hence to ensure validity, no alterations should be done on the platform after the addenda measurements have been done.



Figure 44: Picture of a contact baffle assembly.

Chapter 4

Results, Analysis and Discussion

4.1. Introduction

The results obtained from each experiment described in the previous chapter are presented and discussed in this chapter.

1. The elemental compositions of the compounds were examined using Wavelength Dispersive Spectroscopy (WDS) and the room temperature powder XRD data were analyzed and interpreted through Rietveld analysis performed using FullProf suite [121]
2. All room temperature transmission Mössbauer spectroscopy measurements were analyzed relative to α-Fe. A spectrum with well-defined sextet absorption peaks was obtained for both samples. Vinda D, which is an Add-In on Microsoft Excel was utilized for data fitting and also the presentation of spectra obtained from Mössbauer measurements [122]. The spectral analysis allows for the determination of the hyperfine parameters which provides information about the electronic, structural and chemical properties of Fe atoms of the sample [14].
3. The temperature and magnetic field dependent four-probe electrical transport measurements were carried out using the DC-transport option of Physical Property Measurement System (PPMS) of Quantum Design Inc. USA. The magnetic properties of the samples were investigated using the regular as well as high-temperature VSM option of the PPMS. The heat capacity measurements were also performed using the PPMS.

4.2. Chemical compositional, structural, magnetic, thermal and electrical transport properties of $RuFe_3Si$

The following section is focused on results and discussion of the investigations performed on the cubic metallic compound $RuFe_3Si$. The study commenced with structural determination from XRD data analysis followed by compositional analysis using WDS, magnetization, thermal and electronic measurements and their interpretations.

4.2.1. Chemical Composition

Wavelength-dispersive spectroscopy measurements were performed on a polished surface of the sample to determine the elemental composition of the compound. The results show that the compound is homogeneous (see Figure 45), no additional phases or unreacted constituent elements. Quantitative analysis was performed on multiple spots on the sample surface and the results were averaged to determine the elemental composition based on the atomic percentage of each element relative to the other elements in the sample. The observed averaged elemental ratio corresponds to a stoichiometry of $RuFe_3Si$, which is similar to the nominal elemental ratio used in the sample synthesis. Figure 45 shows the backscattered electron image of $RuFe_3Si$ collected during the WDS measurements. The image shows a nearly uniform and contrast-free sample top surface, which is an indicator for good sample homogeneity. A few small pits present in the image could be a results of small pieces of the material that eroded off during polishing.

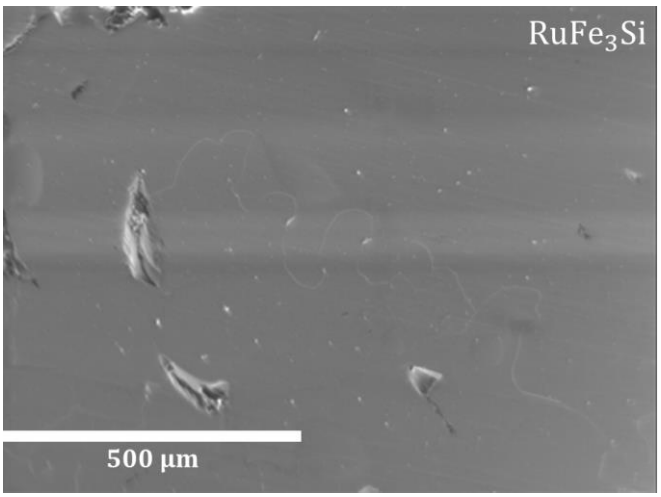


Figure 45: Backscattered electron images of $RuFe_3Si$ showing the topography from the polished surface with a scale magnification of 500 µm taken with a beam acceleration voltage of 15 kV.

4.2.2. Structural Properties

Figure 46 shows the room temperature powder XRD data of $RuFe_3Si$ together with the Rietveld refinement profile, the difference profile and the Bragg positions. The analysis shows the formation of a single-phase compound with no detectable impurities. The results show that the compound crystallizes in a cubic structure with $Fm\bar{3}m$ (225) space group symmetry with a cubic lattice parameter a = 5.7787(2) Å and Z = 4. Two peaks indicated by asterisks (*) at 12.2° and 24.5° are allowed Bragg reflections (111) and (222), respectively, and are of low intensities (<1.2%) compared to the highest intensity (220) peak. These peaks likely originate from a slight anti-site disorder present in the compound. The parameter values obtained from the Rietveld refinement and the site occupancies are presented in Table 6. The chemical unit cell of $RuFe_3Si$ is shown in Figure 47 below where the atomic arrangements and positions are marked in the figure.

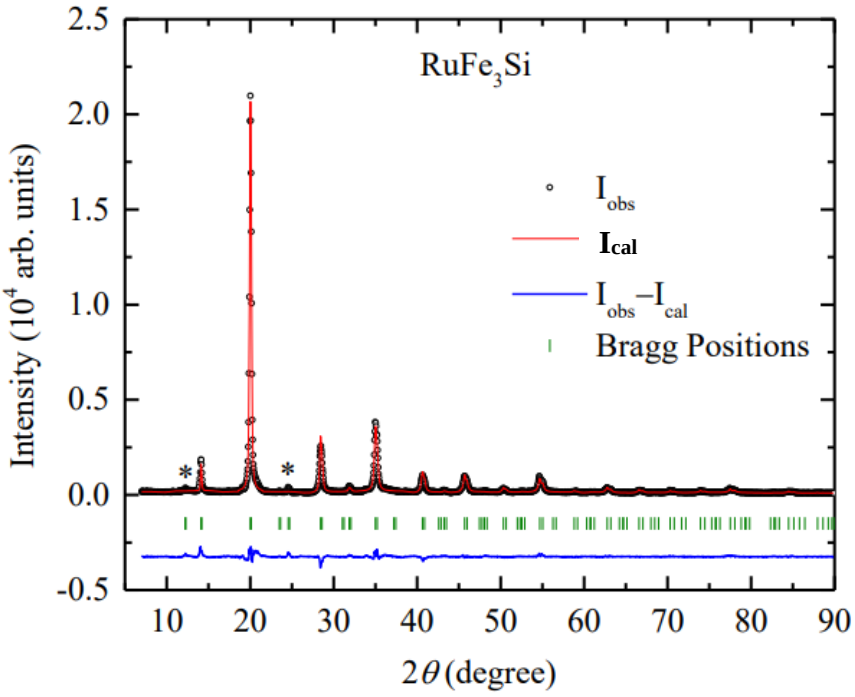


Figure 46: Room temperature powder X-ray diffraction data collected using a Mo source. The solid red curve is the Rietveld refinement profile, the blue curve is the difference profile between the experimental data and the calculated intensities and the green vertical bars mark the Bragg positions. The two asterisks indicate the peaks that likely originate from a slight anti-site disorder present in the compound.

The Rietveld results suggests that there are three distinct Fe sites present in the structure (Table 6). The Wyckoff sites 4*a* and 4*b* are fully occupied by Fe atoms whilst the 8*c* site is

shared between Fe and Ru atoms, each with 50% site occupancy. Si occupies the partially filled 24*d* site with an occupancy fraction of 1/6th (16.7%). The occupancies obtained from the Rietveld refinement suggest that the novel cubic compound $RuFe_3Si$ crystallizes in a vacant structure. The results also suggest that sister ternary compounds $RuFe_3Si_6$ and $Ru_2Fe_2Si_6$ could exist and crystallize in the cubic structure similar to $RuFe_3Si$.

The results obtained from XRD analysis of $RuFe_3Si$ differ significantly from those reported for Fe_3Si which is known to crystalize in Do_3- type structure where Fe atoms occupy two distinct positions within the unit cell. One of the Fe site has eight Fe atoms as nearest neighbours while the second Fe site has four Fe and four Si atoms as nearest neighbours. The three atoms Si, Fe(I) and Fe(II) occupy positions 4*a*, 4*b* and 8*c* respectively.

Table 6: Atomic positions, and site occupancy summary of $RuFe_3Si$ results obtained from full Rietveld refinement of the XRD data.

Atoms	Labels	Site	*x*	*y*	*z*	Site Occupancy	Chemical Unit cell Contribution.
Fe	Fe1	4*a*	0.00	0.00	0.00	100%	1
Fe	Fe2	4*b*	0.50	0.50	0.50	100%	1
Fe	Fe3	8*c*	0.25	0.25	0.25	50%	1
Ru	Ru	8*c*	0.25	0.25	0.25	50%	1
Si	Si	24*d*	0.00	0.25	0.25	16.7%	1

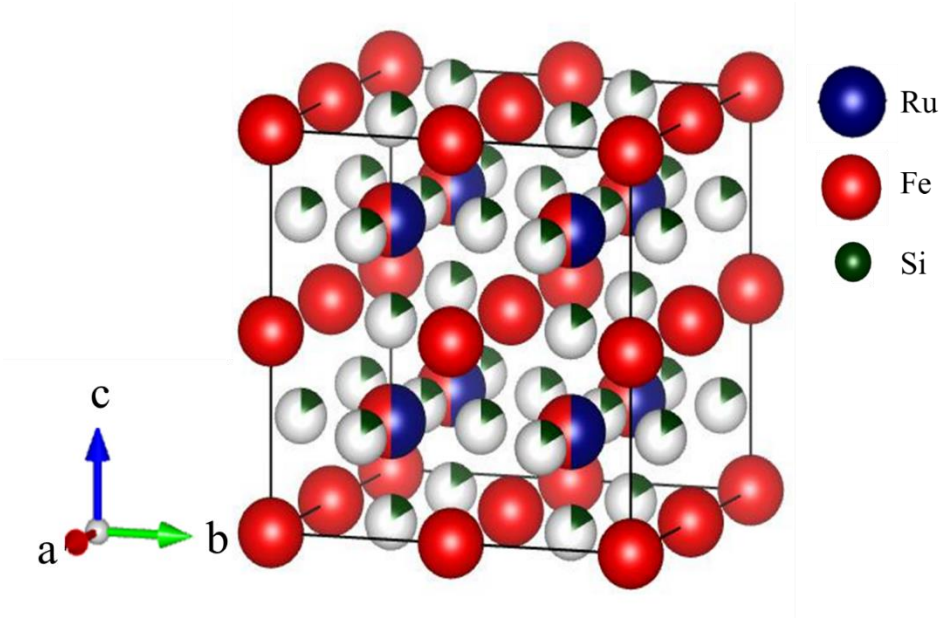


Figure 47: Cubic crystal structure of $RuFe_3Si$. The red and blue spheres indicate a shared occupancy between Fe and Ru, each with 50% site occupancy. Si occupies only 1/6th of its site, the remaining space is indicated in white.

4.2.3. Mössbauer Analysis

A calibration spectrum was measured on α-Fe foil by subsequent fitting of the spectrum, resultant hyperfine parameters were determined as B_{hf} = 32.9 T, δ = 0 mm/s and ΔE = 0 mm/s. The values obtained are in agreement with the hyperfine parameters reported by Shinjo *et al*. for α-Fe: B_{hf} = 33 T, with δ and ΔE both corresponding to 0 mm/s [31].

Transmission Mössbauer spectroscopy was performed at room temperature on a powder $RuFe_3Si$ sample. The data was collected for three days and the resulting spectrum was analysed by fitting different models. The best fit was achieved with four Lorentzian sextets as shown in Figure 48.

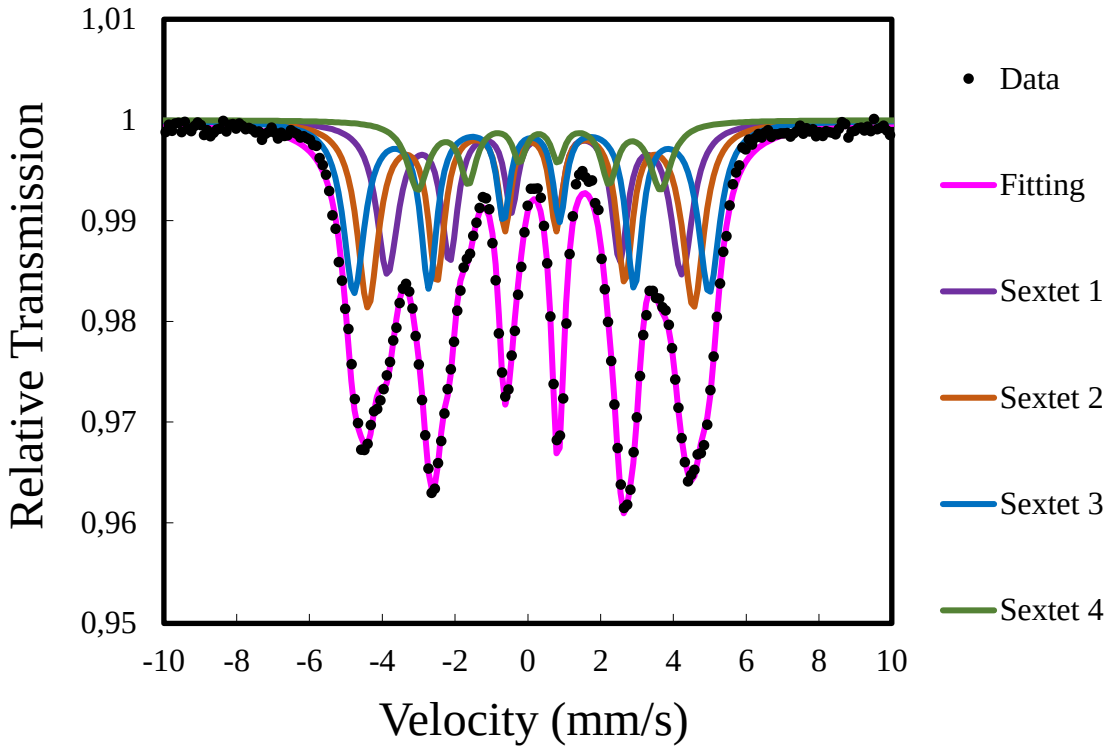


Figure 48: TMS spectra for $RuFe_3Si$ ground powder taken at room temperature.

The observed four sextets (Figure 48) are an indication of four different Fe environments within the $RuFe_3Si$ unit cell as opposed to three equally populated (33% each) sites that one would expect from this compound (Table 6). This anomaly most likely arises from a random placement of Ru and Fe atoms on the 8*c* site of the unit cell, which is occupied by both these atoms in equal proportion. A random placement can possibly lead to different environments for the Fe atoms occupying the 8*c* site in different chemical unit cells. The observed spectrum is dominated by two sextets, 2 and 3, each with a relative area of 31% and two other sextets, 1 and 4, with relative areas of 26% and 12%, respectively. Thus, our Mössbauer data suggests that the Fe atoms on the 8*c* site result in the sextets 1 and 4, while the Fe atoms on the 4*a* and 4*b* sites lead to the observed sextets 2 and 3.

The isomer shift values obtained from the fit were compared against the chart shown in Figure 17 (section 3.2.1.) which shows that isomer shift values and their corresponding oxidation states observed for ^{57}Fe compounds measured at room temperature. The analysis shows that all Fe atoms have a 3+ charge state. The hyperfine parameters extracted from the

fitting and the lattice site assignments are presented in Table 7. The parameters are reported relative to α-Fe.

Table 7: Room temperature hyperfine parameters obtained for the $RuFe_3Si$ powder.

Component	B_{hf} **(T)**	**IS (mm/s)**	ΔE_Q **(mm/s)**	**Relative Area (%)**	**Ionic State**	**Probable Lattice Site**
Sextet 1	25.04(2)	0.187(3)	0	26	Fe^{3+}	8*c*
Sextet 2	27.68(2)	0.077(2)	0	31	Fe^{3+}	4*a*
Sextet 3	30.20(2)	0.101(2)	0	31	Fe^{3+}	4*b*
Sextet 4	20.70(5)	0.303(6)	0.01	12	Fe^{3+}	8*c*

A related compound Fe_3Si that crystallizes in a DO_3-type cubic structure with $Fm\bar{3}m$ (225) space group has only two distinct iron sites [123]. Shinjo *et al*. [29] reported that two iron sites Fe(I) and Fe(II) of this compound have hyperfine fields of 30(1) T and 19(1) T respectively at room temperature. The above-mentioned Fe(I) and Fe(II) sites in Fe_3Si occupy 4*b* and 8*c* lattice sites, and have four and eight nearest-neighbour Fe atoms, respectively [29]. These fields values correspond to sextets 3 and 4 for $RuFe_3Si$ obtained from this study. Thus, here it will be interpreted that in $RuFe_3Si$ the sextet 3 with a relative area of 31% originates most likely from the Fe atoms occupying the 4*b* site while the sextet 4 with a relative area of 12% originates from the Fe atoms occupying the 8*c* lattice site. Sextet 2 with the relative area contribution of 31% can be apparently linked to the Fe atoms at the 4*a* site while the sextet 1 with the relative area of 26% most likely originates from the remaining Fe atoms of the 8*c* lattice site.

4.2.4. Magnetic Properties

The results of temperature (*T*) dependent magnetic susceptibility $\chi \equiv M/H$ measurements, where *M* is the magnetization and *H* is the applied magnetic field, performed on $RuFe_3Si$ between 400 to 890 K at a constant applied field *H* = 100 Oe are shown in Figure 49. The

observed *T*-dependence of the χ data suggests a ferromagnetic (FM) ground state in $RuFe_3Si$. The FM magnetic phase transition was estimated from the point of inflexion in the $\frac{d\chi(T)}{dT}$ *vs T* function shown in the inset of Figure 49 and was determined to be T_C = 873(3) K.

Magnetic measurements were repeated on the same sample this time using the high-temperature VSM option of PPMS with a reachable temperature of 950 K. This was done to ensure that sufficient data was collected above the transition temperature of the compound. The $\chi(T)$ data of $RuFe_3Si$ measured at H = 1000 Oe between 2 to 950 K are shown in Figure 50. As expected, the $\chi(T)$ data shown in Figures 49 and 50 show similar temperature dependences. The smaller $\chi(T)$ values in Figure 50 compared to those in Figure 49 are a manifestation of the higher magnetic field applied in the case of the former compared to the latter. The higher applied magnetic field also has led to a reduction in the T_C. Figure 51 shows the temperature derivative $\frac{d\chi}{dT}$ versus *T* data and derived value of the transition temperature at H = 1000 Oe is T_c = 773(5) K.

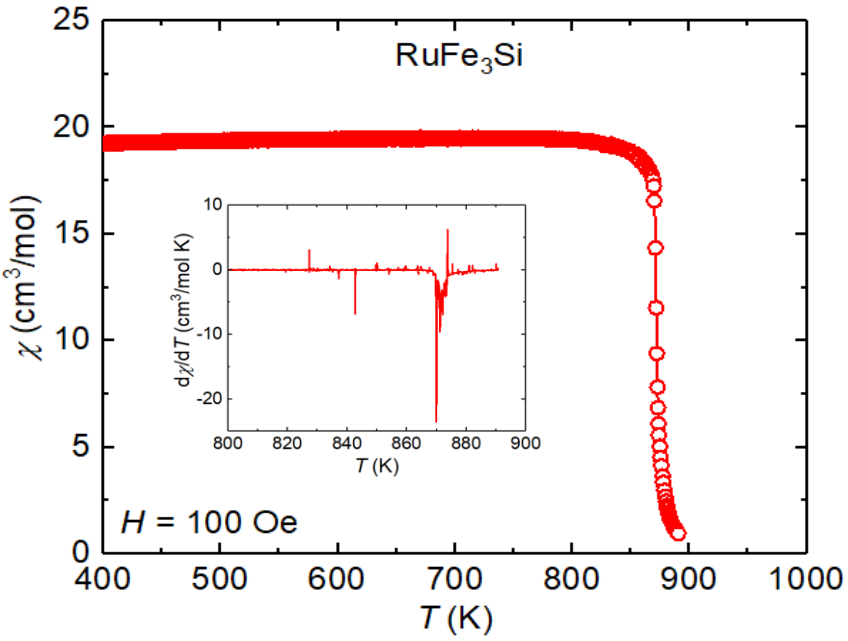


Figure 49: Magnetic susceptibility of $RuFe_3Si$ measured at $H = 100\ Oe$. Inset: first derivative of data showing the temperature at which the magnetic phase transition temperature is observed.

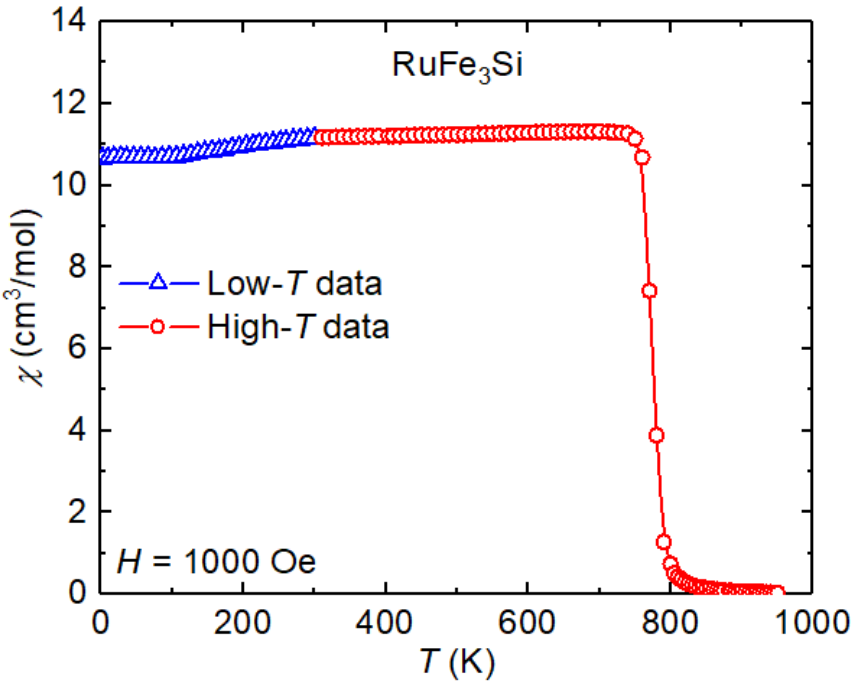


Figure 50: Temperature variation of magnetic susceptibility $\chi(T)$ of $RuFe_3Si$ measured between 2 to 950 K at 1000 Oe. The blue data points (low-T data) were collected using the PPMS at Wits University which does not have the capacity to measure at temperatures above 300 K while the red data points (high-T data) were collected using the PPMS at Iowa State University. Both experiments were performed on the same sample under the same conditions.

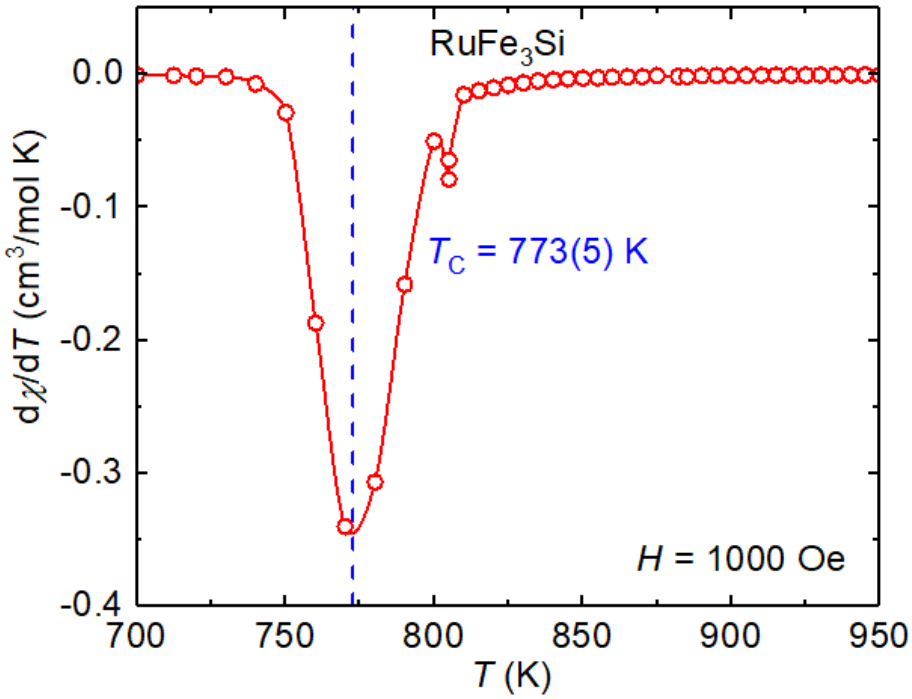


Figure 51: First derivative of susceptibility data where the blue dotted line passing through the minimum value of the curve indicates the phase transition temperature.

In the case of FM materials, an increase in the applied field often results in the reduction of the magnetic susceptibility values as well as the magnetic phase transition temperature. A summary of the results from the two $\chi(T)$ measurements discussed above is shown in Table 8.

Table 8: Variation in the magnetic phase transition temperature T_c of $RuFe_3Si$ with the applied magnetic field.

Field (Oe)	**T_c (K)**
100	873(3)
1000	773(5)

The results discussed so far show that $RuFe_3Si$ has a high FM transition temperature. Similar behaviour was also found for the related cubic compound Fe_3Si, where the FM reported transition temperature falls within the range of 800 to 860 K [30].

The high-temperature (T > 880 K) inverse susceptibility $\chi^{-1}(T)$ values deduced from the $\chi(T)$ data presented in Figure 50 were analyzed using the Curie-Weiss (CW) behaviour described by the following equations:

$$\chi(\mathrm{T}) = \frac{N_{\mathrm{A}}\mu_{\mathrm{eff}}^2}{3k_{\mathrm{B}}(T-\theta)} \tag{4.1a}$$

where N_{A} is Avogadro's number μ_{eff} is the effective magnetic moment, k_{B} is the Boltzmann constant and θ is the Curie temperature. Equation (4.1a) can be written in terms of the Curie constant, C as shown in equation 4.1b.

$$\chi(\mathrm{T}) = \frac{C}{(T-\theta)} \tag{4.1b}$$

Expressing the susceptibility equation in linear form results in:

$$\chi^{-1} = \frac{T}{C} - \frac{\theta}{C} \tag{4.1c}$$

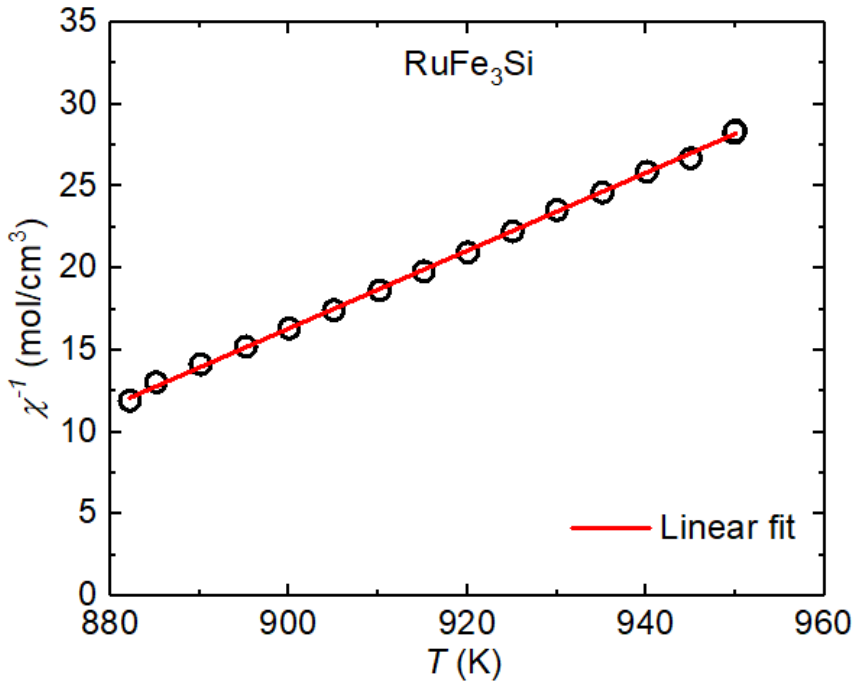


Figure 52: Inverse susceptibility χ^{-1} data at applied magnetic field H = 1000 Oe are plotted as a function of temperature T. The data were fitted using equation (4.1).

The inverse susceptibility data were fitted using the linear function derived from the CW law described in equation.(4.1c). The fit yielded the following values for the parameters: C_{Tot} = 4.20(4) cm^3 K/mol and θ = 828(17) K. The positive sign of the Weiss temperature θ demonstrates the presence of FM interactions within the sample—a fact which also derived from the nature of the $\chi(T)$ data shown in Figures 49 and 50. The estimated value of the

Weiss temperature θ is somewhat larger than the value of T_c obtained above. The ratio $f = \Theta/T_c = 1.07(3) > 1$ is additional evidence for the presence of a long-range FM order in cubic $RuFe_3Si$.

The Curie constant, C can be used to calculate the effective paramagnetic moment μ_{eff} using Equation (4.1a). The calculated value of $\mu_{eff} = 3.4(2)\ \mu_B$/Fe is significantly smaller than $\mu_{eff} = 5.92\ \mu_B$/Fe expected from free Fe^{3+} ions [124] but larger than $\mu_{eff} = 1.8(1)\ \mu_B$/Fe extracted from magnetization experimental data reported by Antoniak *et al*. [125].

Isothermal magnetization M versus H measurements were performed at six different temperatures (Figure 53). The results show an initial increase in M with H followed by a tendency of saturation that occurs at temperature-dependent fields. Plotting lines of best fit through the data points in the saturation region of each isotherm and extrapolating it to $H = 0$ allows one to estimate the saturation moment M_{sat}. The $M(H)$ data at 300 K lead to $M_{sat} = 2.1\ \mu_B$/Fe. This value is in agreement with the 2.17 μ_B/Fe saturation moment reported by Crangle and Goodman [20] for pure iron at room temperature. However, this value is higher than 4.86 μ_B/f.u. ≡ 1.62 μ_B/Fe for Fe_3Si at room temperature [123].

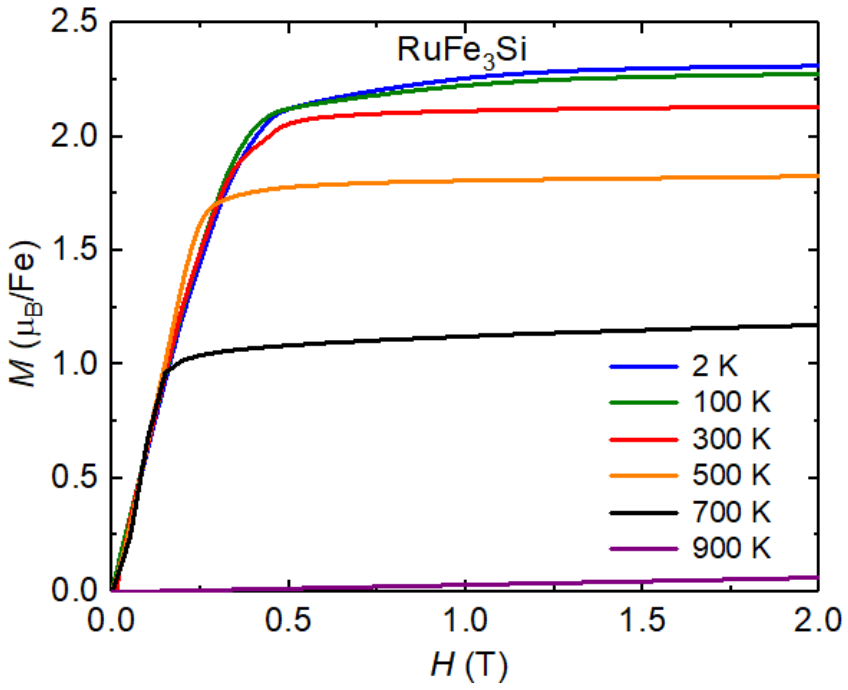


Figure 53: Isothermal magnetization *M* of $RuFe_3Si$ as a function of an applied magnetic field *H* measured at six different temperatures between 2 and 900 K.

As expected, the data collected above the FM ordering temperature T_c show a perfectly linear relationship between the applied field and magnetization. This suggests that the magnetic moments are free to align with the applied field within the material (Figure 54).

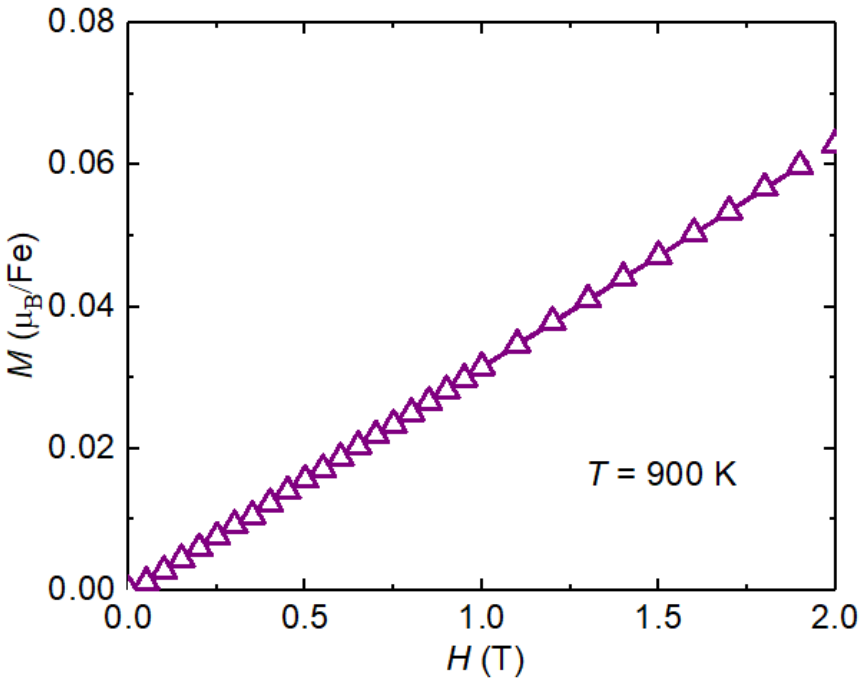


Figure 54: Isothermal magnetization *M* versus applied magnetic field *H* data collected at 900 K showing a linear behaviour.

Figure 55 shows the four-quadrant *M* versus *H* hysteresis plots at temperatures 2 and 300 K. A very narrow hysteresis loop is observed with small values of the coercive field and the remnant magnetization. This demonstrates that $RuFe_3Si$ is a soft ferromagnet, this group of materials are used for electronic applications such as generation, transmission and distribution of electric power [126]. Similar behaviour is observed for Fe_3Si which has small coercive field $H_c \approx 25\ Oe$ [127]. A summary of the data collected at different temperatures is listed in Table 9.

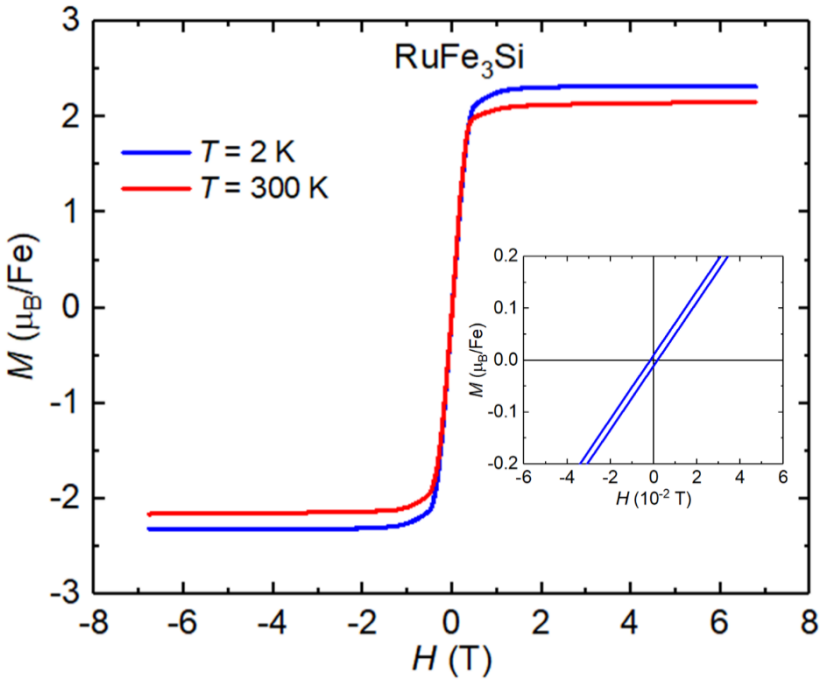


Figure 55: Hysteresis plot of isothermal magnetization, *M* versus applied magnetic field, *H* at T = 2 and 300 K. Inset: an expanded plot at 2 K.

Table 9: Table showing a summary of magnetic parameters obtained from *M*(*H*) experiment performed at different temperatures.

Temperature (K)	Coercive Field, H_c (Oe)	Residual Magnetization M_R (μ_B/Fe)	Saturation Magnetization, M_{sat} (μ_B/Fe)
2	16.26(2)	0.01048	2.3153(6)
100	16.45(3)	0.01056	2.2721(3)
300	16.66(2)	0.01103	2.1296(7)
500	-	-	1.7916(8)
700	-	-	1.0787(9)
900	-	-	$1.1(1) \times 10^{-5}$

The coercive field obtained at three different temperatures were plotted and it was observed that the coercive field increases with decreasing temperature [Figure 56(a)]. This increasing behaviour of coercivity is unusual because at low temperatures, it is expected the magnetic

anisotropy should increase and particles to scatter in the direction of the anisotropic field hence increasing the coercivity.

A trend observed from the analysis of the different isotherms is that M_{sat} decreases with an increase in temperature [Figure 56(b)]. This behaviour is expected for a long-range ordered FM material and occurs because an increase in temperature causes an increase in thermal agitation which opposes the alignment of magnetic dipoles with the applied field, resulting in a decrease in magnetization. The magnetic saturation data points at different temperatures were fitted with a higher-order polynomial of order four. The value of T_C, which is associated with the x-intercept of the curve, was determined to be 890 K. This value is fairly consistent with the phase transition temperature of 873(3) K obtained from the derivative plot of magnetization data collected at H = 100 Oe.

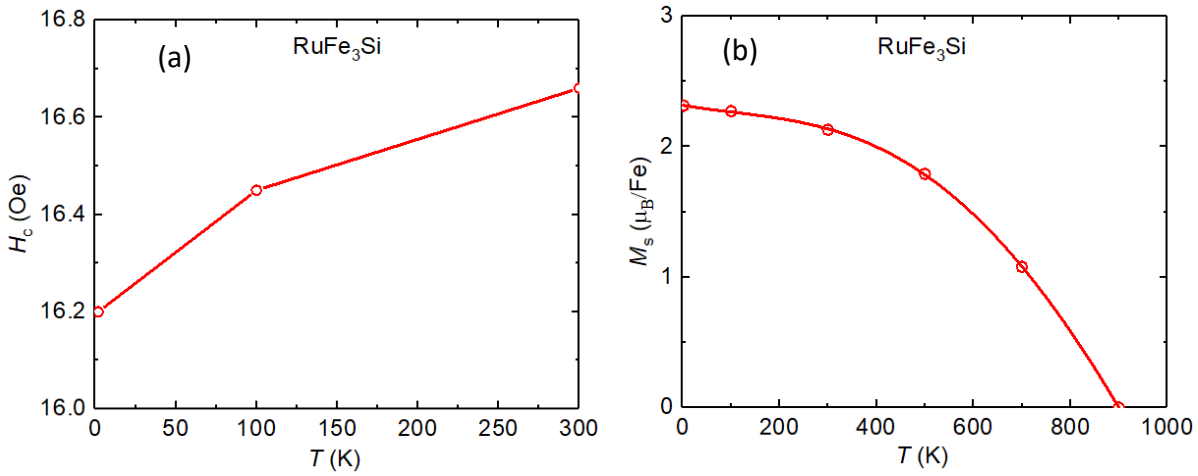


Figure 56: Plots showing the relationship of (a) coercive field H_c and (b) saturation moment M_{sat} as a function of temperature.

4.2.5. Specific Heat

The temperature variation of the specific heat C_p data of $RuFe_3Si$ is shown in Figure 57. We observe that the expected Dulong-Petit value for this compound is achieved with C_p (T) = 3nR = 124.65 J/mol K at room temperature, where n = 5 is the number of atoms per unit formula and R = 8.314 J/mol K is the universal gas constant.

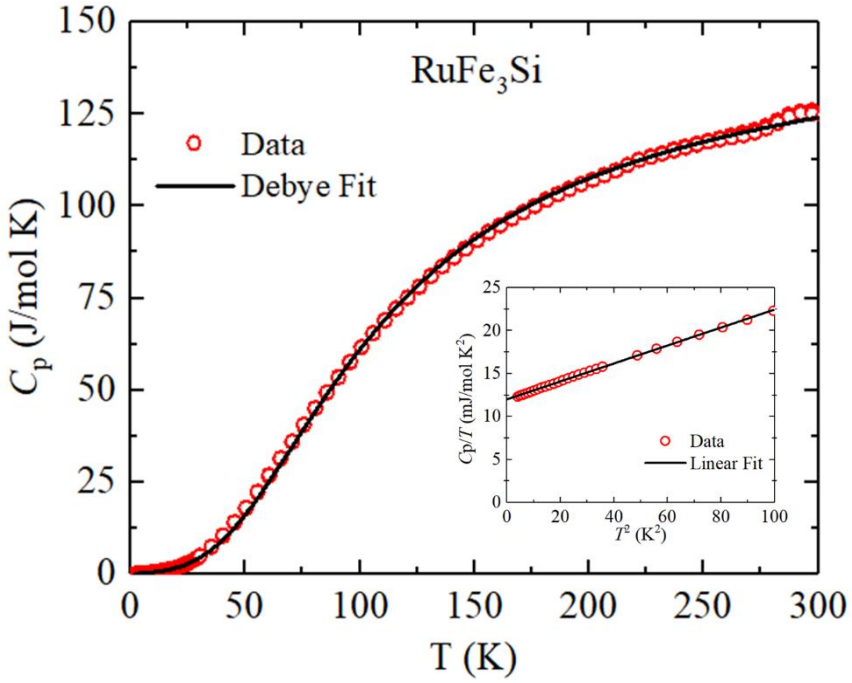


Figure 57: Specific heat C_p versus temperature T data of $RuFe_3Si$ along with the Debye fit (black line). Inset shows a plot of $C_p(T)/T$ versus T^2 plot at low temperature (below 10 K). The red solid line a linear fit.

The specific heat as a function of temperature, $C_p(T)$ between 1.8 to 300 K was fitted with the Debye model of heat capacity with the aid of Padé approximant function which was used to fit the temperature dependence of the heat capacity over the full temperature range. The total heat capacity in the Debye model is given by:

$$C_P(T) = \gamma T + nC_{V\,\mathrm{Debye}}(T) \tag{4.2}$$

$$C_{V\,\mathrm{Debye}}(T) = 9R\left(\frac{T}{\Theta_\mathrm{D}}\right)^3 \int_0^{\Theta_\mathrm{D}/T} \frac{x^4 e^x}{(e^x-1)^2}\,dx \tag{4.3}$$

where n is the number of atoms per formula unit, γ is the Sommerfeld coefficient and R is the universal gas constant. From the fit , the following values were obtained; γ = 35.6(4) mJ/mol K^2 and Θ_D (all T) = 430(1) K.

The low-temperature $C_p(T)$ data is described by the sum of electronic and phononic contributions and obeys the following form:

$$C(\mathrm{T})_{\mathrm{T}\to 0} = C_{\mathrm{el}}(\mathrm{T}) + C_{\mathrm{ph}}(\mathrm{T}) = \gamma \mathrm{T} + \beta \mathrm{T}^3 \qquad (4.4)$$

where the Sommerfeld coefficient γ and constant β of specific heat can be determined by fitting the $C_p(T)/T$ versus T^2 data with a straight line. The inset of Figure 57 shows the $C_p(T)/T$ versus T^2 of $RuFe_3Si$ for $T < 10$ K and the red line is the linear fit. The calculated parameters were: γ = 22.40(2) mJ/mol K^2 and β = 0.278(1) mJ/mol K^4. The estimated β value was used to calculate the Debye temperature at the low-temperature using the expression:

$$\Theta_{\mathrm{D}} = \left[\frac{12\pi^4 nR}{5\beta}\right]^{1/3} \qquad (4.5)$$

this yielded Θ_D (low T) = 327(1) K, which is smaller than the value Θ_D(all T) = 430(1) K estimated from the Debye fit performed over the entire temperature range of our measurement. It is not unusual to obtain different values of Θ_D from the Debye model in equation.(4.3) and from low-temperature exponent approximation in equation.(4.4). However, in this study, the obtained values are significantly different. This observation needs to be explored further.

The electronic density of states at the Fermi level $D(E_F)$ for $RuFe_3Si$ was obtained using the γ value from the Debye fit using the following relation:

$$\gamma = \left(\frac{\pi^2}{3}\right) D(E_{\mathrm{F}}) {k_{\mathrm{B}}}^2 \qquad (4.6)$$

which gives a value of 9.50(2) states/eV fu for both spin directions.

4.2.6. Electrical Resistivity

Electrical resistivity ρ versus T data for $RuFe_3Si$ were collected between 2 and 300 K. The data show an increase in ρ with an increase T, i.e. a positive temperature coefficient of resistivity in the entire temperature range of our measurement. This behaviour is typically observed in metallic samples. Similar behaviour is observed for the related cubic compound Fe_3Si [27]. The data shows a relatively low residual resistivity of ρ_0 = 9.15(1) μΩ cm but it also exhibits a low residual resistivity ratio (RRR) ≡ ρ(300 K)/ρ(2 K) = 1.15, which indicates that a large amount of scattering could be resulting from the defects and grain boundaries present in our polycrystalline material.

The $\rho(T)$ data were fitted using the Bloch-Grüneisen (B-G) model with the aid of Padé approximants as described in a paper by Goetsch *et al.* [128]. which describes the electrical resistivity of a metal due to the scattering of conduction electron by the acoustic lattice vibrations:

$$\rho(T) = \rho_0 + A\left(\frac{T}{\theta_R}\right)^5 \int_0^{\Theta_R/T} \frac{x^5}{(e^x-1)(1-e^{-x})}\,dx, \qquad (4.7)$$

where Θ_R is the Debye temperature obtained from the electrical resistivity of metals, ρ_0 is the residual resistivity and A is the temperature coefficient. A good fit was obtained for the data using equation (4.7) (Figure 58) and the estimated value of Θ_R is 404(1)K, which falls between the values of 327(1) K and 430(1) K obtained from the analysis of the C_p(T) data.

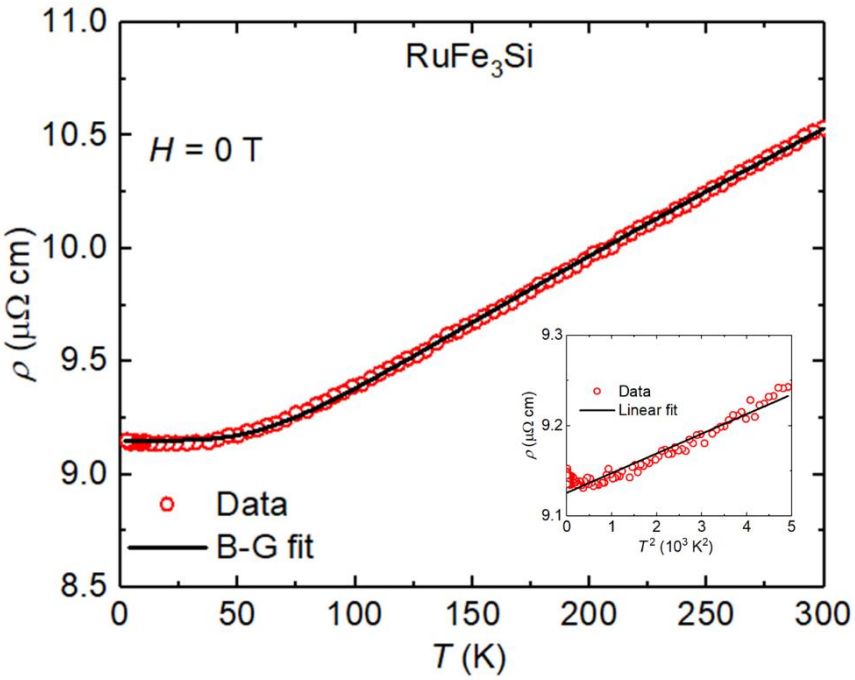


Figure 58: Temperature *T* variation of the electrical resistivity ρ of $RuFe_3Si$ at *H* = 0 T. The black solid curve is the fit by the Bloch-Grüneisen (B-G) model. Inset shows the low-temperature resistivity data with a linear fit.

The fit of $\rho(T)\ vs\ T^2$ takes the following form:

$$\rho(T) = \rho_0 + AT^2 \tag{4.8}$$

which can be used to obtain an estimate of the residual resistivity, $\rho_0 = 9.15(1)\ \mu\Omega.\text{cm}$ and the magnitude of $A = 2.18(5) \times 10^{-5} \mu\Omega\ \text{cm/K}^2$ which can be used to calculate the value of the Kadowaki-Woods relation together with the magnitude of γ obtained from the electronic contribution to heat capacity:

$$R_{KW} = \frac{A}{\gamma^2} \tag{4.9}$$

which gives a value of $R_{\text{KW}} = 0.043(1)\ \mu\Omega\ \text{cm mol}^2\ \text{J}^{-2}\ \text{K}^2$. The position of $RuFe_3Si$ on the Kadowaki-Woods plot is indicated with a red dot in Figure 59 located below the transition metal line. This indicates that the electronic correlations of $RuFe_3Si$ are smaller than those observed in transition metals.

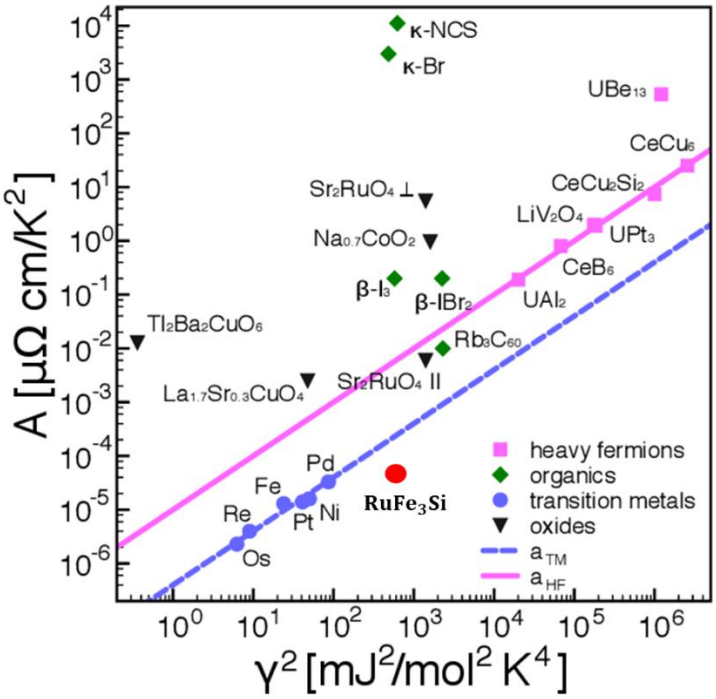


Figure 59: The standard Kadowaki-Woods plot. The position of $RuFe_3Si$ is indicated by a red dot *[129]*.

4.2.7. Magnetoresistance

A field of 1T was applied to study the behaviour of the electrical resistivity of $RuFe_3Si$ under the influence of an applied field. The results were plotted along with the zero-field data (Figure 60) show no significant changes between the two. This suggests that low magnetic fields do not affect the electrical transport behaviour of this material below its FM ordering temperature. The temperature dependence of magnetoresistance $\left(MR = \frac{\rho(H=1)-\rho(H=0)}{\rho(H=0)}\right)$ expressed as a percentage was calculated and the results indicate a very small positive magnetoresistance.

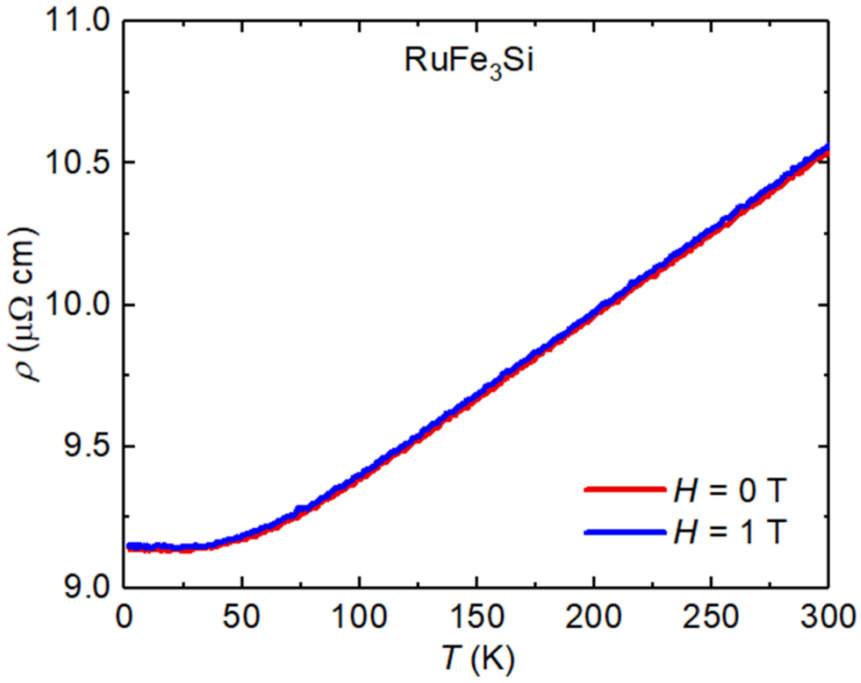


Figure 60: Temperature T dependence of electrical resistivity ρ at H = 0 T and H = 1 T.

4.3. Chemical compositional, structural, magnetic, thermal and electrical transport properties of $RhFe_3C$

The following section is focused on a discussion of the investigations performed on the cubic metallic compound $RhFe_3C$. The study started with structural determination from XRD data analysis followed by compositional analysis using WDS, magnetization, thermal and electronic measurements and their interpretations.

4.3.1. Chemical Composition

Wavelength-dispersive spectroscopy results show that the compound is practically homogeneous with no additional binary or ternary phases. The backscattered electron image (Figure 61) shows that the sample contains a homogenous phase comprising of elements Rh, Fe and C (light grey). The dark patches contain high levels of carbon. Quantitative analysis was performed on multiple spots on the polished surface and the results were averaged to determine the elemental composition based on the atomic percentage of each element related to the other elements in the sample. It was determined that within the resolution limit the phase nearly corresponds to a composition of stoichiometry $RhFe_3C$ with some unreacted carbon present as an impurity phase.

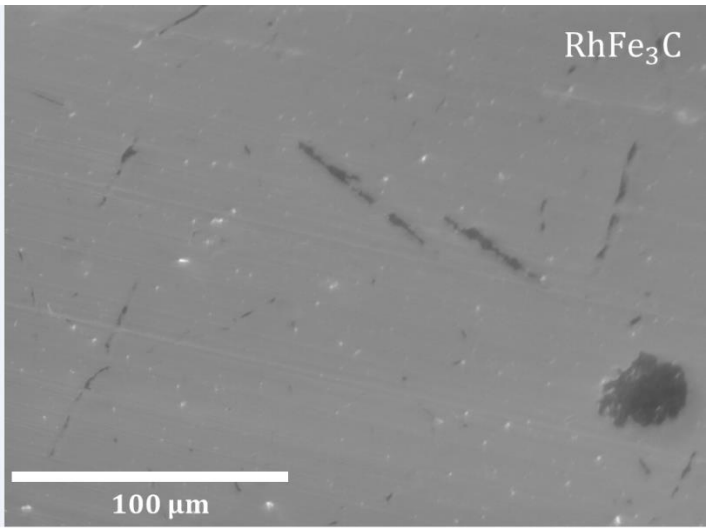


Figure 61: Backscattered electron images of $RhFe_3C$ showing the topography from the polished surface with a scale magnification of 100 µm taken with a beam acceleration voltage of 15 kV. The dark areas and needle-like structures and patches observed contain unreacted carbon.

4.3.2. Structural Properties

Figure 62 shows the XRD pattern of $RhFe_3C$ obtained at room temperature together with the Rietveld refinement profile, the difference profile and allowed Bragg positions. The analysis shows the formation of ternary $RhFe_3C$ that crystalizes in a cubic structure $Fm\bar{3}m$ (225) space group symmetry with a lattice parameter a = 5.8929(5) Å and Z = 4. The results also indicate the presence of a small amount of unreacted carbon.

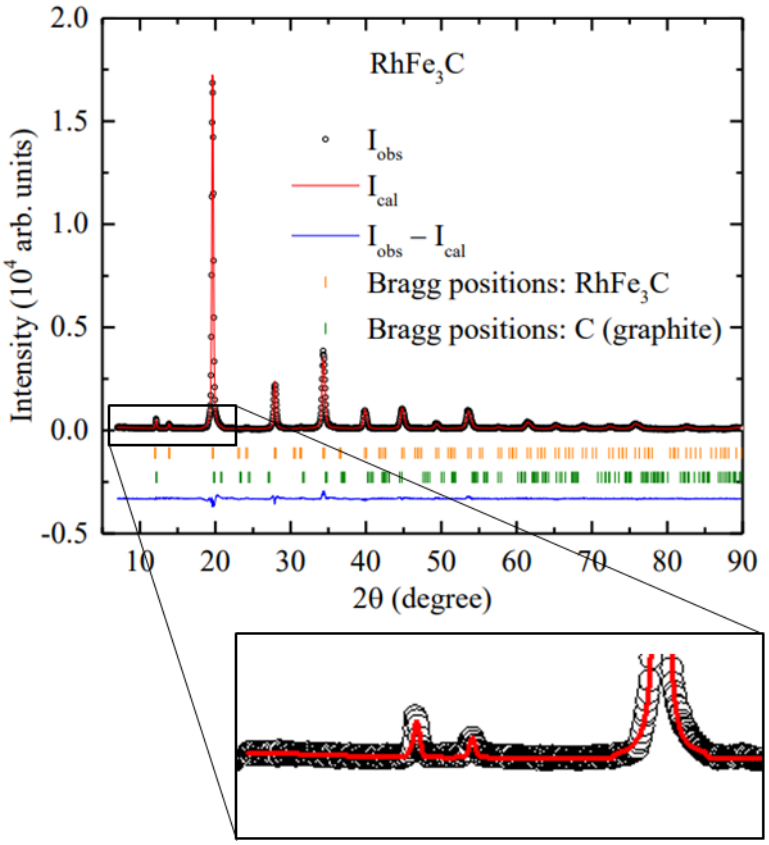


Figure 62: Room temperature Powder X-ray diffraction data of $RhFe_3C$ collected using Mo source. Two-phase Rietveld refinement, difference profiles and Bragg positions for $RhFe_3C$ (orange) as well as for unreacted carbon (green) are shown. The magnified section of the diffraction pattern clearly shows data and fitting around the carbon peak.

The parameters obtained from Rietveld refinement and site occupancies are listed in Table 10. Figure 63 shows the chemical unit cell of $RhFe_3C$ where the atomic arrangement and the position of each atom are shown. The analysis performed shows that there are three different Fe sites. Wyckoff site 4*b* is fully occupied by Fe atoms while sites 4*a* and 8*c* are shared between Fe and Rh atoms. The carbon atoms occupy $1/6^{th}$ of the 24*d* site.

Table 10: Atomic positions and site occupancies obtained from Rietveld refinement of the room temperature powder XRD data of $RhFe_3C$.

No.	Atom	Labels	Site	*x*	*y*	*Z*	Site Occupancy	Unit cell Contribution.
1	Fe	Fe1	4*a*	0.00	0.00	0.00	75%	0.75

2	Fe	Fe2	4*b*	0.50	0.50	0.50	100%	1
3	Fe	Fe3	8*c*	0.25	0.25	0.25	62.5%	1.25
4	Rh	Rh1	8*c*	0.25	0.25	0.25	37.5%	0.75
5	Rh	Rh2	4*a*	0.00	0.00	0.00	25%	0.25
6	C	C	24*d*	0.00	0.25	0.25	16.7%	1

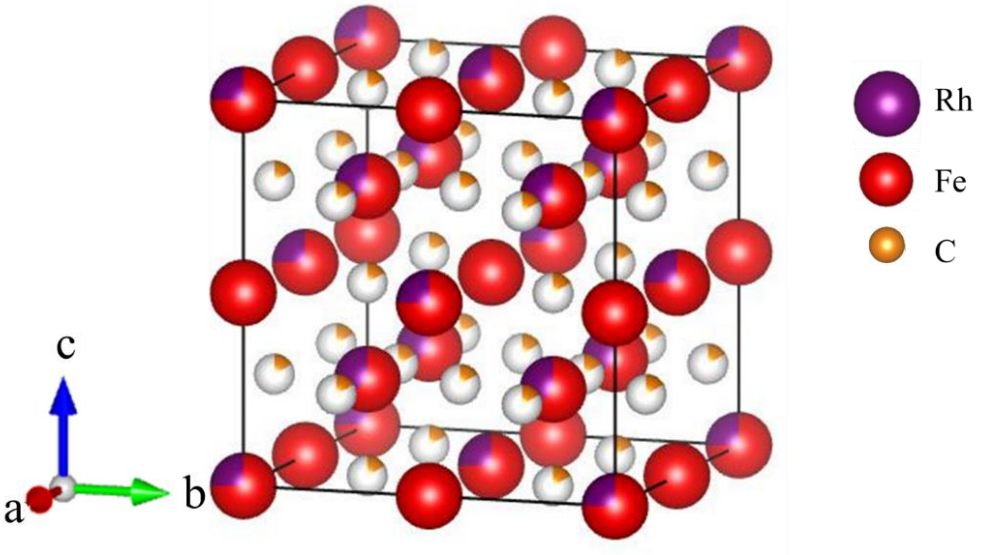


Figure 63: Cubic crystal structure of $RhFe_3C$. The purple and red spheres indicate a shared site between Fe and Rh. C occupies 1/6th of the 24*d* site.

The results obtained differ significantly from the related compound Fe_3C which crystalizes in an orthorhombic structure with space group Pnma. The Fe atoms are located at two different sites in this compound [24].

4.3.3. Mössbauer Analysis

The Mössbauer spectrum of $RhFe_3C$ obtained at room temperature is shown in Figure 64 and the parameters are summarized in Table 11. The best fit of the experimental data and the model was achieved by fitting three sextets and a singlet.

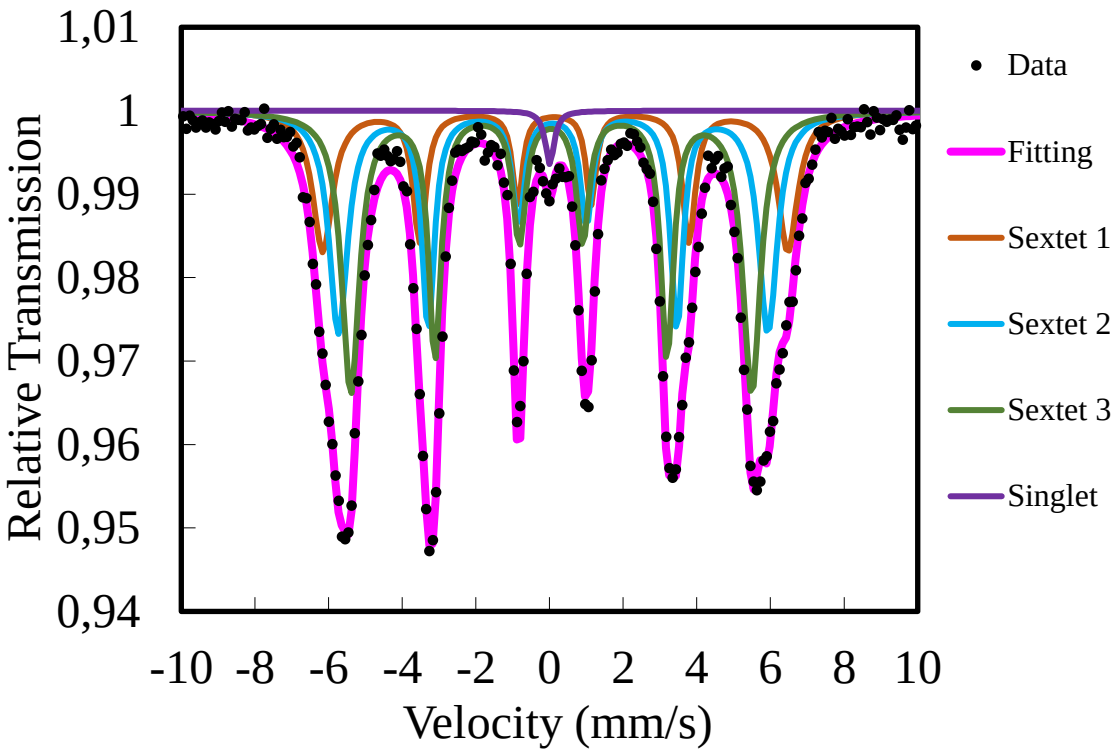


Figure 64: Transmission Mössbauer spectroscopy spectrum of $RhFe_3C$ powder measured at room temperature.

The three sextets used to fit the Mössbauer data give an indication for three possible iron sites within the structure of $RhFe_3C$. Sextet 3 with a B_{hf} = 33.75 T isomer shift and quadrupole splitting values ~ 0 mm/s has hyperfine parameters similar to those observed in α-Fe (i.e. B_{hf} = 32.9 T, δ = 0 mm/s and ΔE = 0 mm/s). The singlet component that was fitted makes up a very small percentage of the relative area and could have arisen from the small impurities within the sample.

The oxidation state of the iron atoms was determined though the comparison of isomer shift values against those shown in Figure 17, this shows that the iron atoms have a 3+ charge state. The probable lattice site of the three Fe atoms was determined by comparing data from our Mössbauer analysis more specifically the relative area of each component with the unit cell contribution of each atom obtained from powder XRD data.

Sextet 1 has a relative area of ~23 % which is less that the expected area of ~33 % (from one of three Fe atoms occupying the unit cell). From our powder XRD data, this would correspond to Fe atoms occupying the 4*a* site (with 0.75 site occupancy). Sextet 2 with a relative area of ~34 % corresponds to Fe atoms occupying 4*b* site which occupies 100 % of its site while sextet 3 which occupies a larger relative area is attributed to Fe atoms occupying the 8*c* site which has a unit cell contribution of 1.25.

Table 11: Room temperature hyperfine parameters for the compound $RhFe_3C$.

Component	B_{hf} (T)	IS (mm/s)	ΔE_Q (mm/s)	Relative area (%)	Assignments	Probable lattice site
Sextet 1	39.12(5)	0.144(5)	0.03(1)	22.97(8)	Fe^{3+}	4*a*
Sextet 2	36.12(3)	0.090(3)	0.02(1)	34.72(9)	Fe^{3+}	4*b*
Sextet 3	33.72(2)	0.043(3)	0.003(1)	41.29(9)	Fe^{3+}	8*c*
Singlet	-	0.007(2)	-	1.01(3)	-	-

The hyperfine parameters obtained from the fit seem to differ significantly from those obtained for the related binary compound Fe_3C. $RhFe_3C$ has three different iron sites each characterised by a high magnetic hyperfine field, whereas Fe_3C is known to have two iron sites with low magnetic hyperfine fields (H = 20.5 T and H = 20.7 T) at room temperature [24]. This difference was expected and originates from the different crystal symmetries of the two compounds.

4.3.4. Magnetic Properties

Figure 65 shows the temperature dependence of the magnetic susceptibility $\chi(T) \equiv M/H$ of $RhFe_3C$, where M is magnetization and H is the applied magnetic field, measured in the temperature range of 300 to1000 K in the presence of an applied field of 0.1 T. No phase transition was observed within the above-mentioned temperature range suggesting that the ordering temperature of the compound is >1000 K. Co_2based Heusler compounds exhibit the highest Curie temperature with $T_C = 1100 \pm 20$ K being reported for Co_2FeSi [130]. High Curie temperatures, magnetic moments are desirable for spintronic applications where one needs to prevent a reduction of the magnetic properties by thermal effects.

Previous studies performed on $RhFe_3N$ show that the compound has a Curie temperature of 505(25) K which is significantly lower than what we would expect for $RhFe_3C$ [16]. Another

related binary compound Fe_3C is reported to have a ferromagnetic Curie temperature in the range of 459 to 483 K [24, 26].

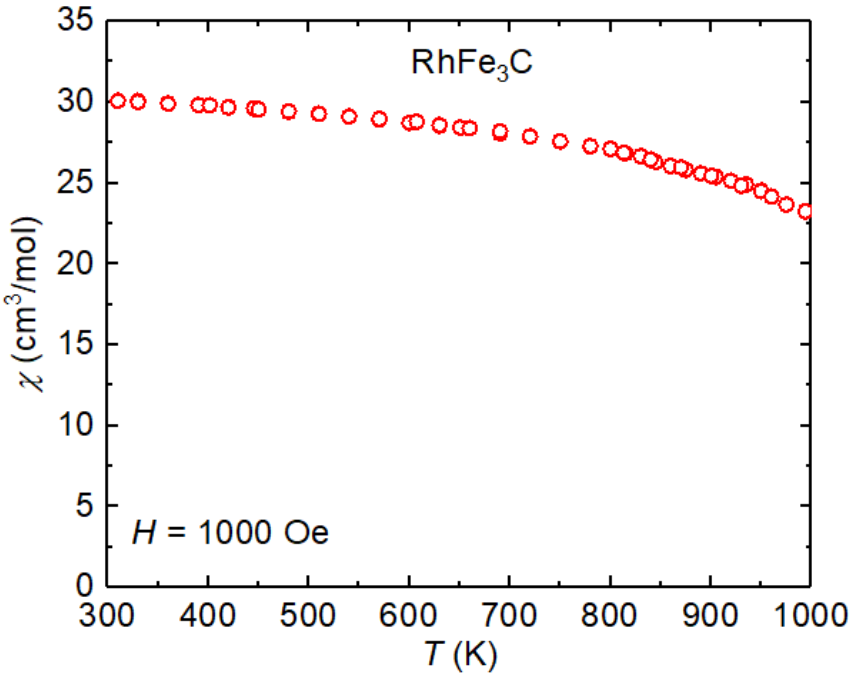


Figure 65: Magnetic susceptibility χ(*T*) of $RhFe_3C$ measured in a field-cooled mode at 0.1 T.

Figure 66 shows the field dependence of magnetic isotherms at three different temperatures. It is observed that as the magnetic field is increased, the magnetization also increases and saturates at ≈ 2.5 T. The saturation magnetization of $RhFe_3C$ decreases with an increase in temperature as expected. The saturation moment recorded at three temperatures ranges from 2 μ_B/Fe to 2.6 μ_B/Fe (Figure 67). This is in perfect agreement with the saturation moment of pure Fe which is reported to be 2.17 μ_B/Fe [20]. $RhFe_3N$ has a saturation moment of 2.77 μ_B/Fe [16].

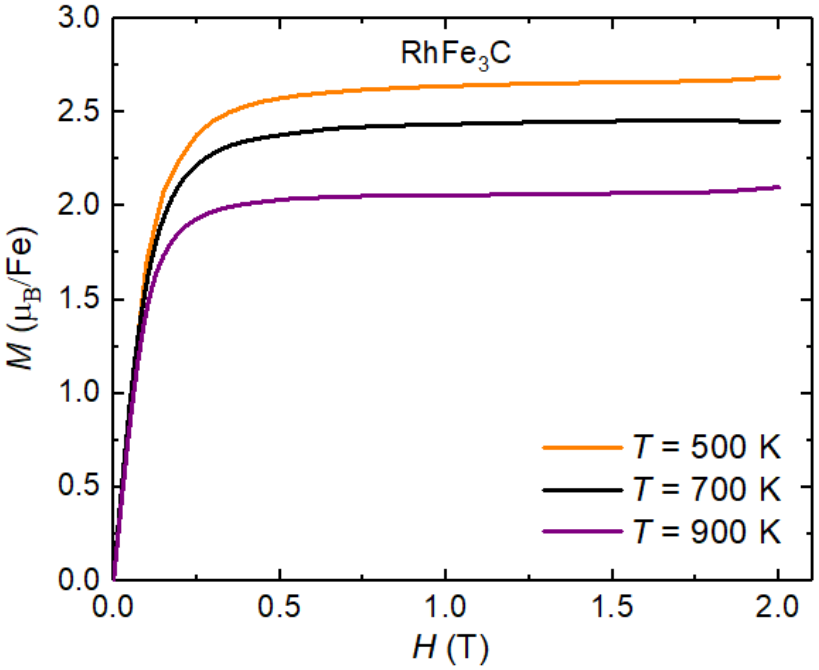


Figure 66: Magnetization versus applied magnetic field of $RhFe_3C$.

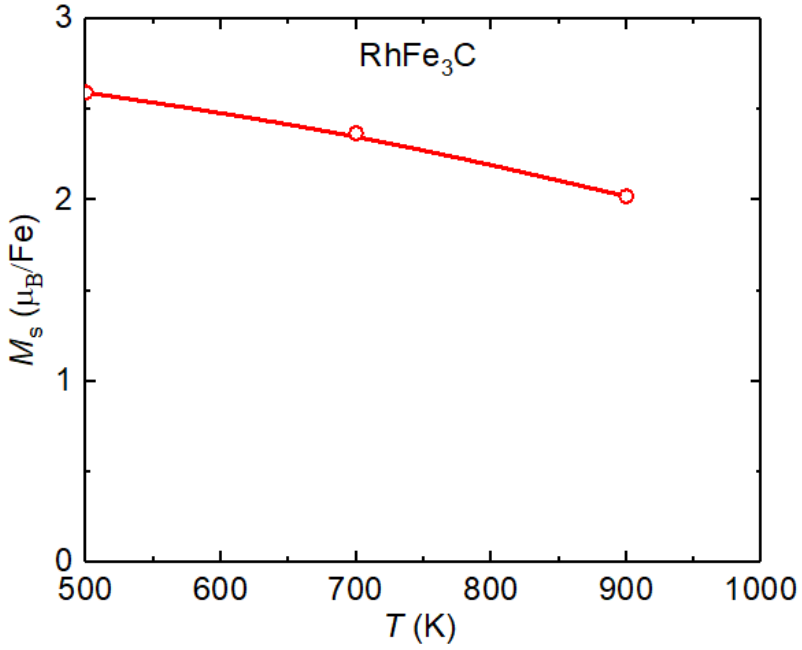


Figure 67: The saturation moment of $RhFe_3C$ as a function of temperature.

4.3.5. Specific Heat

The specific heat C_p of $RhFe_3C$ as a function of temperature T is shown in Figure 68. The data was collected between 2 to 300 K and no phase transitions were observed within this temperature range. The value of C_p as we approach room temperature is ≈ 100 J/mol K which is less than the full Dulong-Petit lattice heat capacity value of $C_p = 3NR = 124.65$ J/mol K, where $N = 5$ is the number of atoms per unit formula and R = 8.314 J/mol K is the universal gas constant.

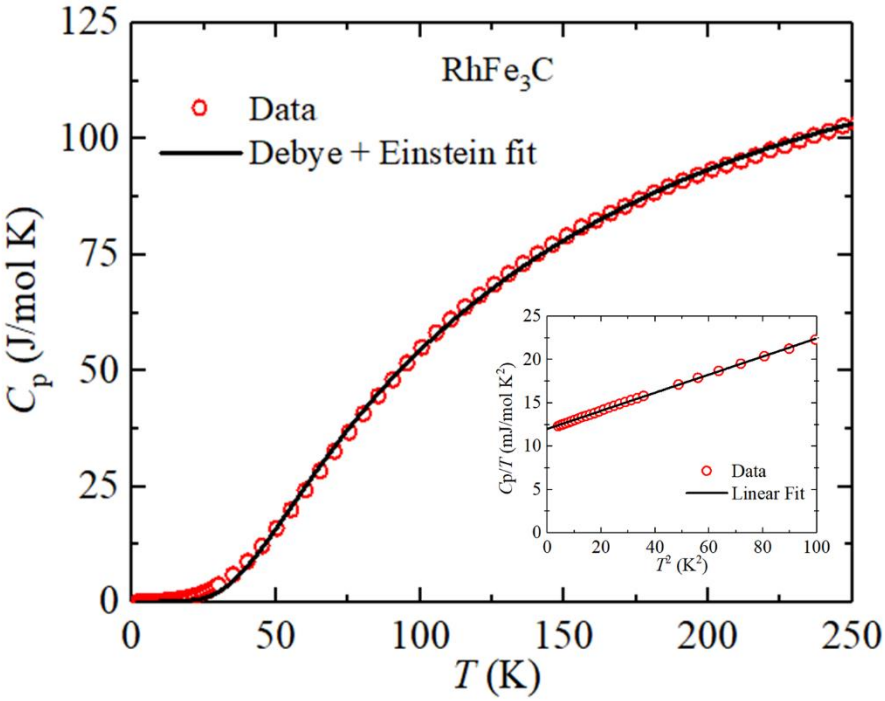


Figure 68: Specific heat data, $C_p(T)$ of $RhFe_3C$ with Debye + Einstein fit (black curve). Inset: plot of $C_p(T)/T$ *vs* at low temperature with a linear fit.

The $C_p(T)$ data over the full temperature range was initially fitted by the Sommerfeld electronic heat capacity together with the Debye model, this resulted in a poor fit with the experimental data, especially at high temperatures. Therefore to improve the fit, an Einstein lattice heat capacity term was added to the equation:

$$C_P(T) = \gamma T + (1-\alpha)C_{V\,\mathrm{Debye}} + \alpha\, C_{V\,\mathrm{Einstein}} \qquad (4.10)$$

$$C_{V\ \text{Einstein}}(T) = 3R\left(\frac{\theta_E}{T}\right)^2 \frac{e^{\theta_E/T}}{(e^{\theta_E/T}-1)^2} \tag{4.11}$$

where γ is the Sommerfeld coefficient, α is the fraction representing the Einstein contribution to the total lattice heat capacity and Θ_E is the Einstein temperature. From the fit, the following values were obtained: Θ_D (all T) = 784(14) K and Θ_E (all T) = 237(3) K. To reduce the number of the fitting parameters in our model, γ was treated as a fixed variable and its value was obtained from the analysis of low-T data.

The Sommerfeld coefficient γ and constant β, which is a coefficient associated with low-temperature lattice contributions to heat capacity, are determined experimentally by fitting the low-T data plot of $C_p(T)/T$ versus T^2 with a straight line. The inset (b) of Figure 68 is the plot of $C_p(T)/T$ vs T^2 in the low-temperature region for T < 10 K and the black line is a linear fit performed to extract γ and β. The parameters calculated for $RhFe_3C$ were found to be γ = 12.00(2) mJ/mol K^2 and β = 0.1045(5) mJ/mol K^4. The extracted β value was used to calculate the Debye temperature for the low-temperature range using the expression:

$$\Theta_D = \left[\frac{12\pi^4 nR}{5\beta}\right]^{1/3} \tag{4.12}$$

which yielded Θ_D(low T) = 453(2) K. This value is significantly smaller than Θ_D(all T) = 784(14) K obtained using fitting the Debye model. Both Debye temperature values are higher than Θ_D = 394 K obtained for Fe_3C [23].

The electronic density of states at the Fermi level $D(E_F)$ for $RhFe_3C$ was obtained using the γ value from the Debye fit using the following relation:

$$\gamma = \left(\frac{\pi^2}{3}\right) D(E_F) {k_B}^2 \tag{4.13}$$

which gives a value of 5.09(2) states/eV fu for both spin directions.

4.3.6. Electrical Resistivity

The electrical resistivity ρ of $RhFe_3C$ as a function of temperature T measured between 2 to 300 K is plotted in Figure 69. The data shows that ρ increases with the increase in T, a behaviour that is routinely observed in metallic samples. The value of ρ at 2 K and 300 K is used to calculate the residual resistivity ratio (RRR):

$$RRR \equiv \frac{\rho(300\ K)}{\rho(2\ K)} = 2.72$$

Unlike $RuFe_3Si$ where the Bloch-Grüneisen (BG) model was a good fit to the experimental data, the $\rho(T)$ data of $RhFe_3C$ were approximated with the function $\rho(T) = \rho_0 + AT^2$. The estimated values of the residual resistivity ρ_0 and the coefficient A are 2.169(1) μΩ cm and 4.221(3) $\times 10^{-5}$ μΩ cm/K^2 respectively.

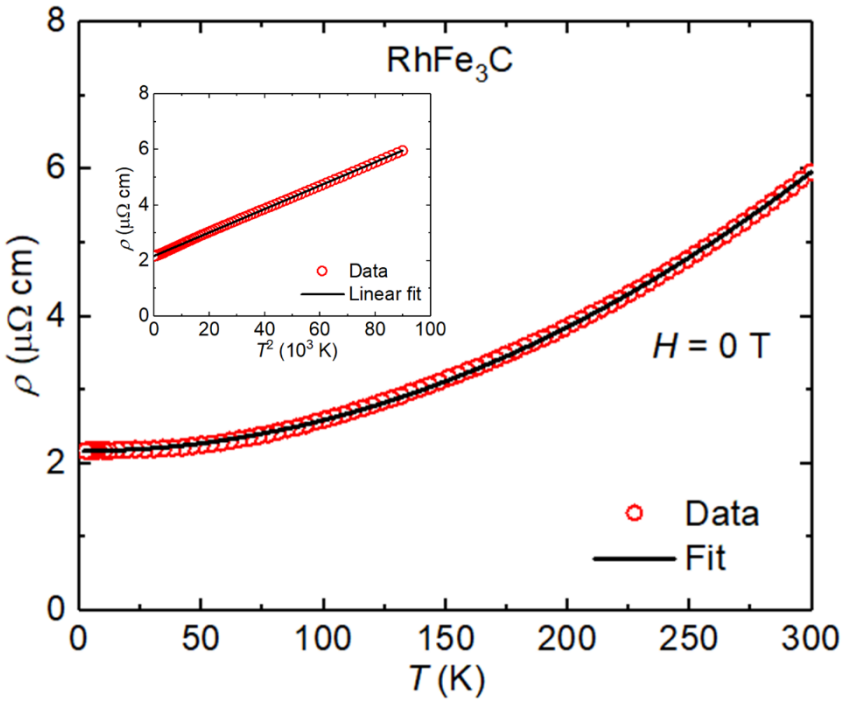


Figure 69: Resistivity ρ as a function of temperature T for 2 K ≤ T ≤ 300 K. the solid black curve is the fit to the experimental data using $\rho(T) = \rho_0 + AT^2$. The inset exhibits ρ as a function of T^2 for 2 K ≤ T ≤ 10 K. The solid black line is a linear fit to the data.

Kadowaki-Woods ratio $R_{KW} = A/\gamma^2$, where A is the coefficient of the T^2 term in the equation $\rho(T) = \rho_0 + AT^2$ and γ is the Sommerfeld coefficient, provides insight into the strength of electronic correlations present in a metallic system. The value of R_{KW} estimated for $RhFe_3C$

is 0.291 μΩ cm mol^2 J^{-2}K^2. As shown below in Figure 70, the $RhFe_3C$ falls close to the trend observed for transition metal compounds, suggesting the presence of moderate electron correlations within the system.

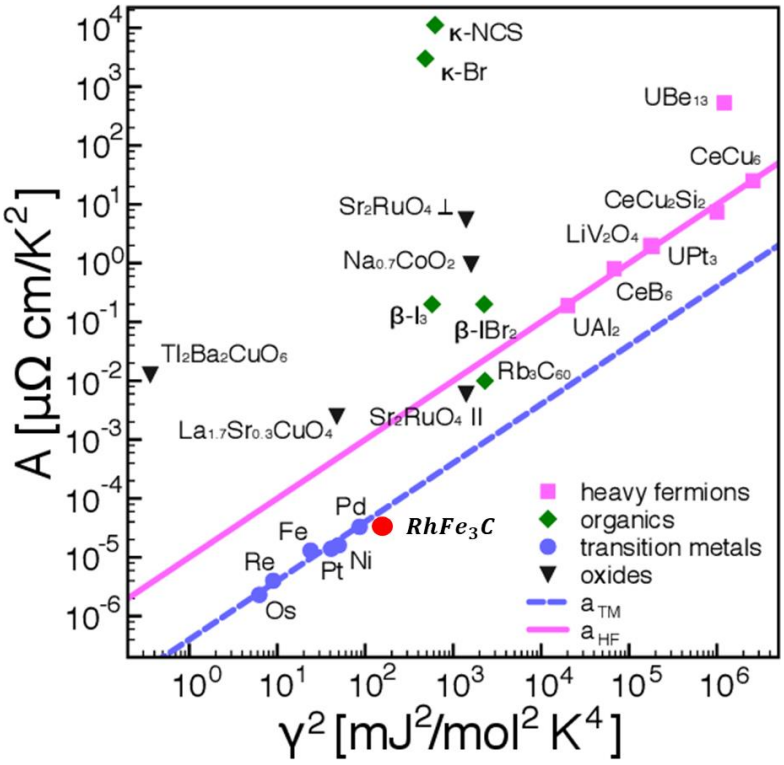


Figure 70: The Kadowaki-Woods plot. The position of $RhFe_3C$ is indicated by a red dot *[129]*.

4.3.7. Magnetoresistance

The temperature dependence of magnetoresistance of $RhFe_3C$ expressed in percentage change in magnitude $\Delta\rho/\rho$ (%), where $\Delta\rho = \rho(H = 1\text{ T}) - \rho(H = 0\text{ T})$, is shown in Figure 71. The compound exhibits a positive $\Delta\rho/\rho$ which decreases with an increase in temperature. Attempts to perform measurements under higher fields >1 T were unsuccessful. Because of the highly magnetic sample, the leads came off when the strength of the applied field exceeded 1 T.

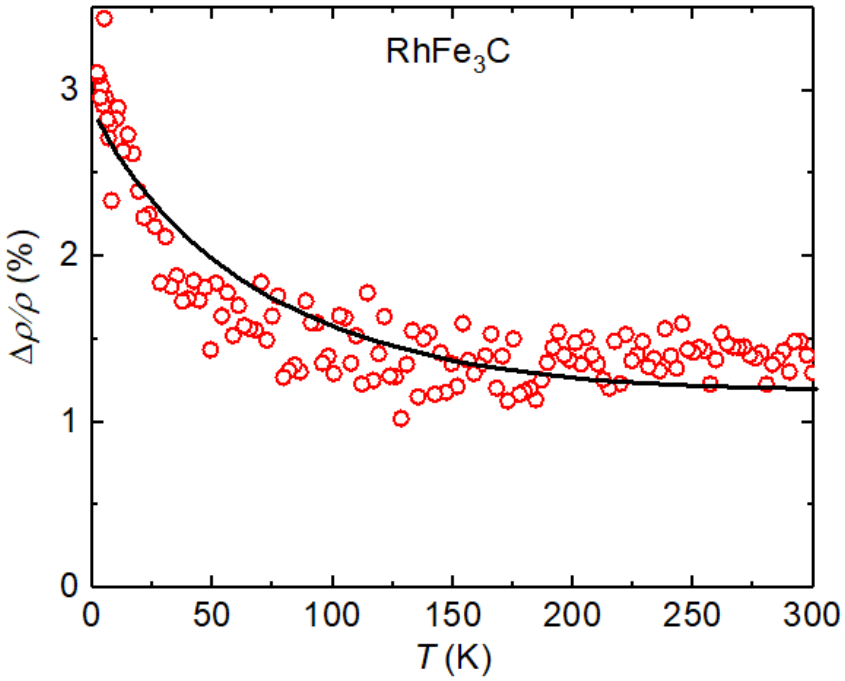


Figure 71: Magnetoresistance $\Delta\rho/\rho$ as a function of temperature T between 2 to 300K.

Chapter 5

5.1. Conclusion and Future Work

The work reports the first investigation of the structural, electronic and magnetic properties of the cubic compounds $RuFe_3Si$ and $RhFe_3C$. The two compounds were successfully synthesized using the arc melting technique and their structural, compositional, magnetic, thermal and electrical transport properties were examined using WDS, XRD, Mössbauer Spectroscopy, heat capacity, resistivity and magnetization measurements as a function of applied magnetic field and temperature. The following conclusions are outlined from this study:

Polycrystalline samples were synthesized using arc melting, the weight loss during synthesis was less than 0.15 %. Results from WDS infers the stoichiometric ratio of the constituent elements Ru:Fe:Si and Rh:Fe:C are 1:3:1 as expected. Backscattered electron images collected over the polished surfaces of $RuFe_3Si$ revealed a homogeneous structure with no detectable impurities. In the case of $RhFe_3C$ traces of unreacted carbon along with the main phase were observed.

Results obtained from powder XRD measurements confirmed that the two compounds crystalize in cubic structures belonging to the $Fm\bar{3}m$ (225) space group. Mössbauer results show that Fe atoms occupy four different sites in the $RuFe_3Si$ chemical unit cell all with a charge state 3+. $RhFe_3C$ also has three different iron sites within its chemical unit cell with high magnetic hyperfine fields. One of the Fe sites exhibits hyperfine parameters similar to those of α-Fe.

The magnetic susceptibility data collected for $RuFe_3Si$ at H = 100 Oe suggests a high Curie temperature of 873(3) K. The inverse susceptibility data follows the Curie-Weiss law at high temperature. The calculated Weiss temperature was positive which indicates interactions associated with a ferromagnetic nature. Isothermal magnetization measurements performed on $RuFe_3Si$ shows that the material has a narrow hysteresis loop with and a small coercive field which is indicative of a soft ferromagnetic material. Magnetic susceptibility data of $RhFe_3C$ was measured within the temperature range 300 to 950 K and no magnetic transition was observed within this range. This indicates that the compound has a Curie temperature greater than 950 K, suggesting the presence of a strong magnetic interaction present within

the material. The other compounds known to exhibit this property includes Co-based Heusler alloys. These are prime candidates for use in spintronic applications.

Heat capacity and resistivity measurements were performed from 2 to 300 K. The electrical resistivity measurements conducted on both the materials show a positive temperature coefficient of resistance as well as finite resistivity values at the lowest temperature 2 K of the measurements undertaken. This implies that these compounds have metallic ground states. Temperature-dependent heat capacity and resistivity data collected on $RuFe_3Si$ were analyzed using the Debye and Bloch-Grüneisen model, respectively, with the aid of Padé approximants. The Debye temperature, Θ_D (all T) = 430(1) K was determined by fitting the $C_p(T)$ data using the Debye model. The fitting of $\rho(T)$ data using the Bloch-Grüneisen model resulted in the transport Debye temperature Θ_R of 404(1) K. Both these values are in reasonable agreement suggesting that the overall Debye temperature of $RuFe_3Si$ is > 400 K. The Kadowaki-Woods ratio of $RuFe_3Si$ has the value $0.043(1)\ \mu\Omega\ \text{cm mol}^2\ \text{J}^{-2}\ \text{K}^2$ and is located below the transition metal line on the Kadowaki-Woods plot while $RhFe_3C$ has a Kadowaki-Woods ratio of 0.291 $\mu\Omega$ cm mol^2 $J^{-2}K^2$ which puts it close to the transition metals trend. The information obtained seem to suggest that the electronic correlations of $RuFe_3Si$ are smaller than those observed in transition metals and $RhFe_3C$ has a moderate electron correlation within its system.

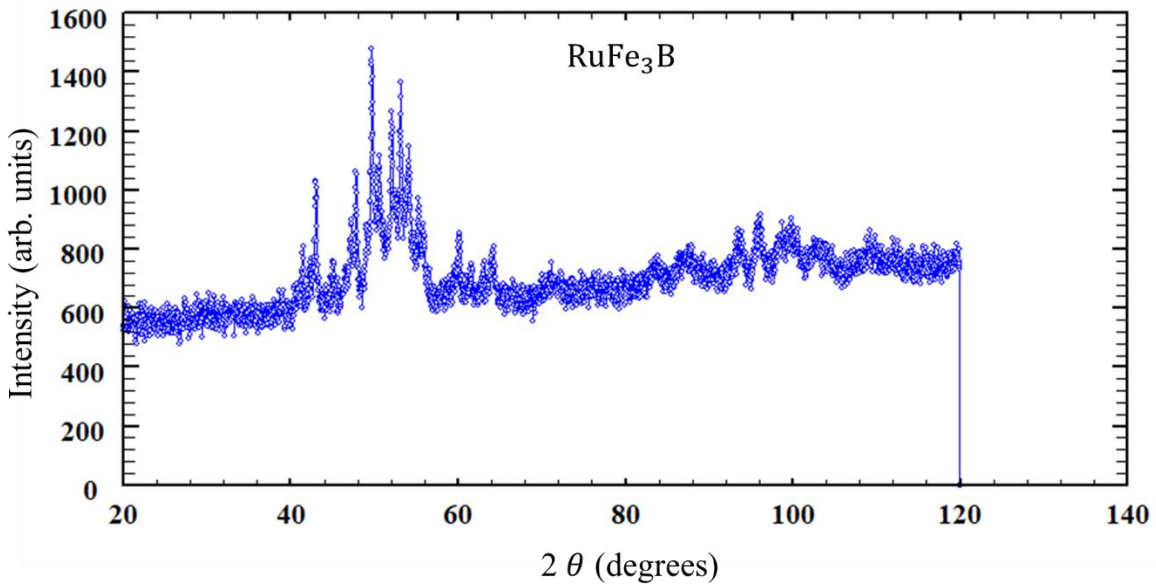
The $C_p(T)$ data of $RhFe_3C$ could not be fitted satisfactorily using the Debye model only. As a result, an Einstein Term was added to the Debye model to fit the data. A good fit to the data was obtained with this modified fit function and the resultant value of Θ_D (all T) was 784(14) K. The fitted value of the Einstein temperature Θ_E (all T) was 237(3) K. This indicates that there is a presesnce of low frequency Ei nstein modes of vibrations within this system. Unlike $RuFe_3Si$, the $\rho(T)$ data of $RhFe_3C$ does not follow the expectations of the Bloch-Grüneisen model and it instead follows a quadratic trend which obeys $\rho(T) = \rho_0 + AT^2$.

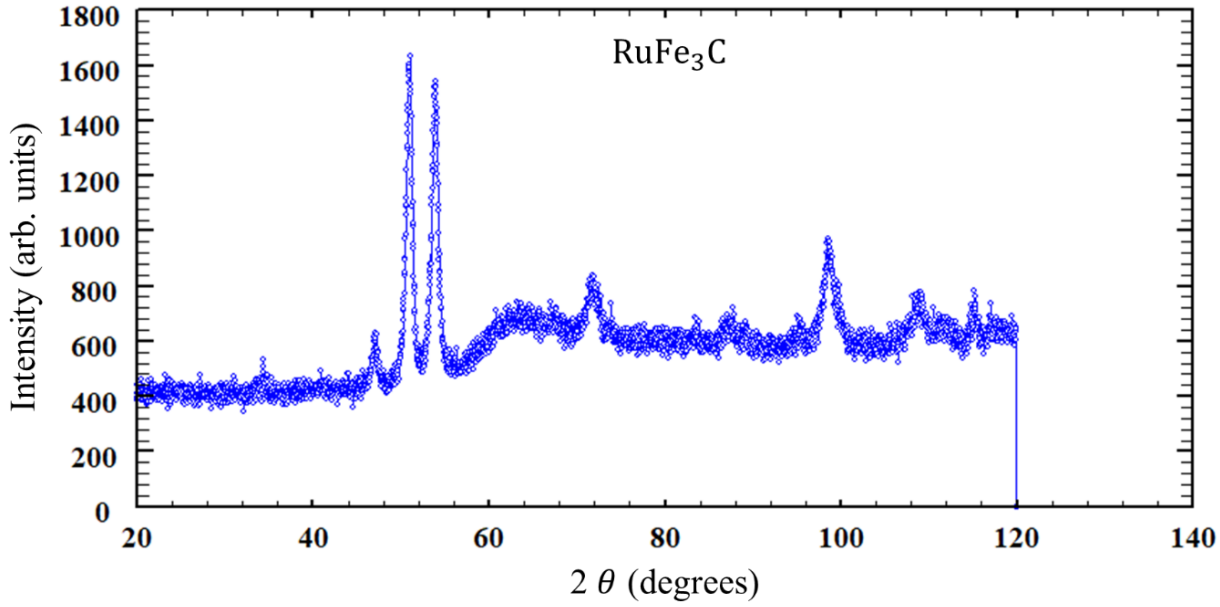
Future work scope includes attempting to synthesize single-phase $RhFe_3C$, this will be extended to the other materials included in the series (see appendix). Synthesis of single crystals of compounds $RuFe_3Si$ and $RhFe_3C$ is to be carried out to eliminate impurities within their polycrystalline structure and get a clearer picture of the intrinsic properties of these materials. The XRD results suggest that ternary compounds $RuFe_3Si_6$ and $Ru_2Fe_2Si_6$ could exist and crystallize in a cubic structure similar to $RuFe_3Si$. Measurements performed for this dissertation can be extended to the two sister compounds as well. Higher temperature

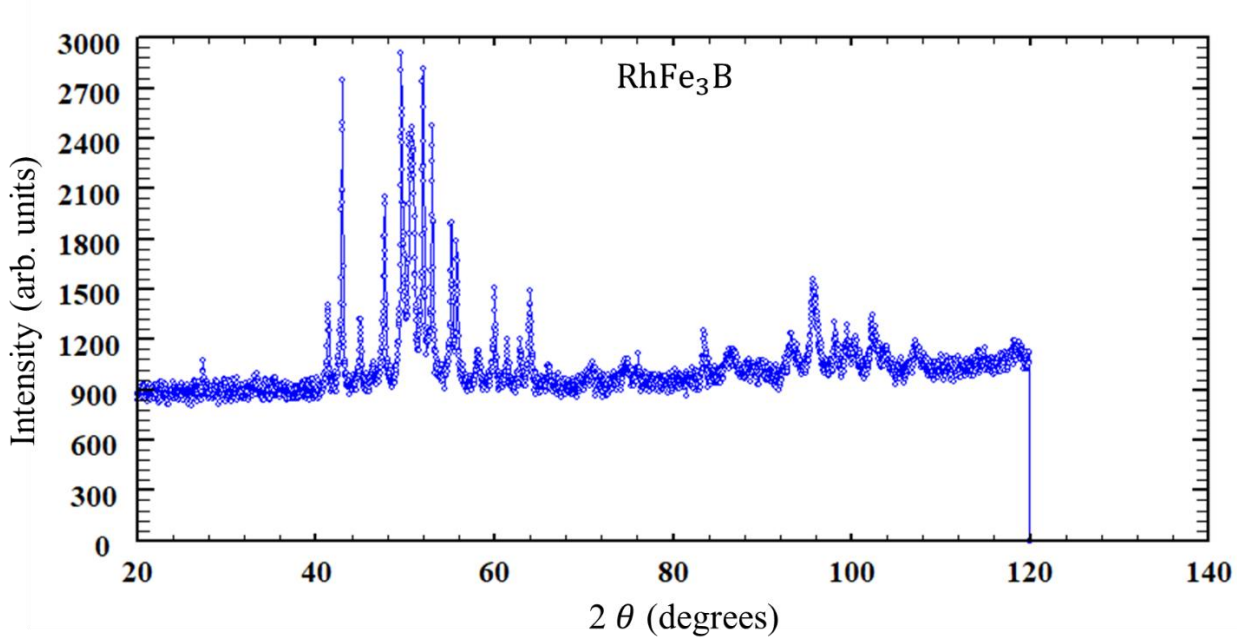
magnetic measurements need to be performed to further investigate the behaviour of the materials at regions around its Curie temperature.

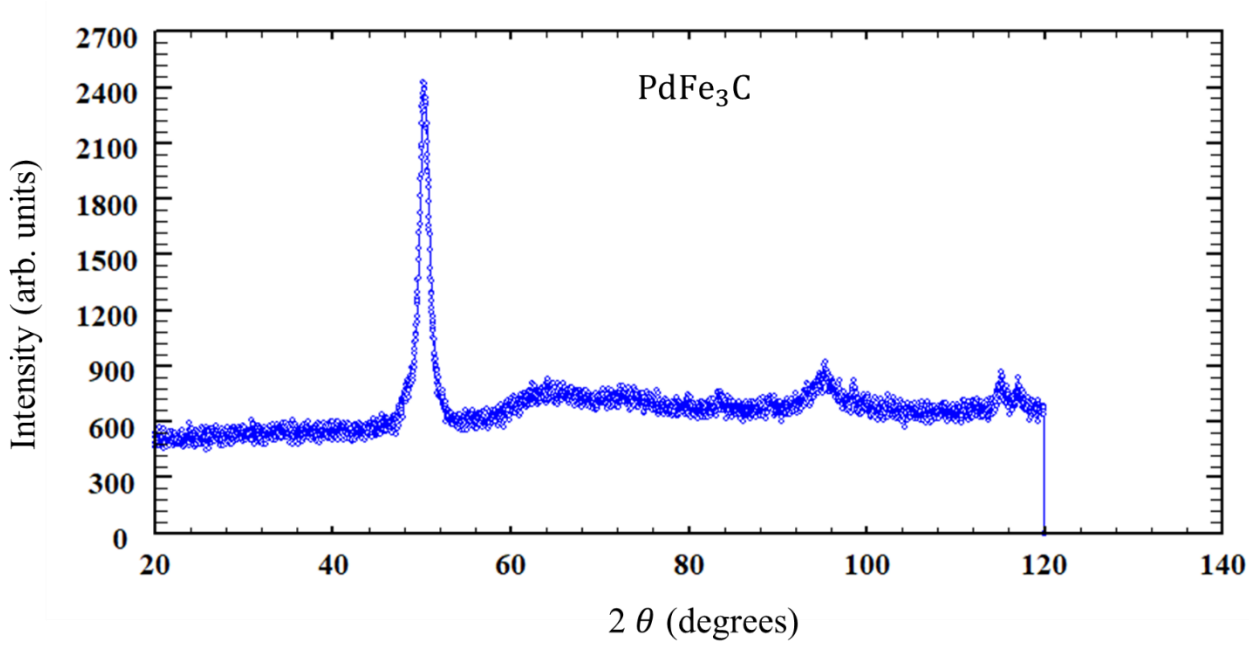
5.2. Appendix A: XRD Profiles

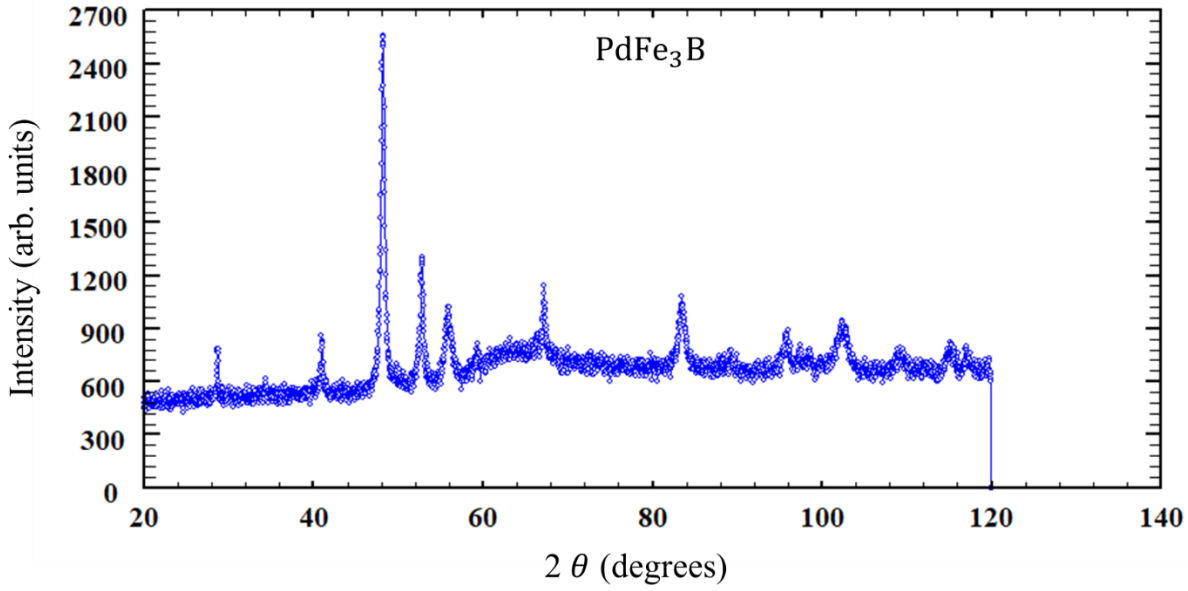
The following figures are the XRD profiles of the compounds that were proposed for this study but were found not to form the desired crystal structure after analysis using powder XRD.

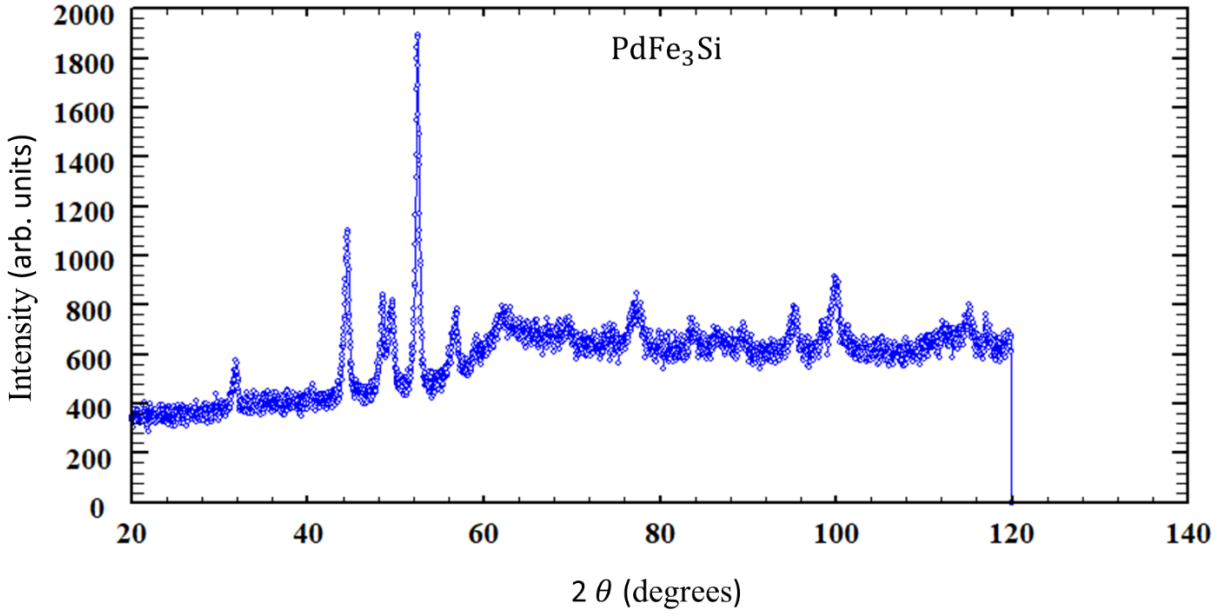





RhFe3B
Intensity (arb. units)
3000
2700
2400
2100
1800
1500
1200
900
600
300
0
20
40
60
80
100
120
140
2 θ (degrees)


PdFe3C
Intensity (arb. units)
2700
2400
2100
1800
1500
1200
900
600
300
0
20
40
60
80
100
120
140
2 θ (degrees)


PdFe3B
Intensity (arb. units)
2700
2400
2100
1800
1500
1200
900
600
300
0
20
40
60
80
100
120
140
2 θ (degrees)


PdFe3Si
Intensity (arb. units)
2000
1800
1600
1400
1200
1000
800
600
400
200
0
20
40
60
80
100
120
140
2 θ (degrees)

5.3. References

[1] K. Frohna and S. D. Stranks, "Hybrid perovskites for device applications," in *Handbook of Organic Materials for Electronic and Photonic Devices*, Woodhead Publishing, 2019, pp. 211-256.

[2] E. Dagotto, T. Hotta and A. Moreo, "Colossal Magnetoresistant Materials: the key role of phase separation," *Physics Reports*, vol. 344, pp. 1-153, 2001.

[3] "Britannica, The Editors of Encyclopaedia," 22 December 2020. [Online]. Available: https://www.britannica.com/science/iron-chemical-element. [Accessed 3 January 2022].

[4] J. Puetz, S. Heusing and M. A. Aegerter, "Characterization of Electrical Properties," in *Handbook of Sol-Gel Science and Technology*, Germany, Kluwer Academic Publishers, 2004, pp. 457-480.

[5] V. Kartha, "Spintronics and Spintronic Devices," PhD Thesis, University of Kerala, 2011.

[6] I. Zutic, J. Fabian and S. Das Sarma, "Spintronics: Fundamentals and Applications," *Reviews of Modern Physics*, vol. 76, pp. 323-410, 2004.

[7] A. Snair, Y. Venkateswara and K. G. Suresh, "Study of Heusler Alloys For Spintronic Application," *Journal of Mechanical and Production Engineering*, vol. 4, pp. 126-131, 2016.

[8] A. Tikkanen, "Encyclopedia Britannica," 17 June 2017. [Online]. Available: https://www.britannica.com/technology/magnetic-recording. [Accessed 09 February 2020].

[9] H. Coufal, L. Dhar and D. Mee, "Materials for Magnetic Data Storage: The Ongoing Quest for Superior Magnetic Materials," *MRS Bulletin*, vol. 31, pp. 374-378, 2006.

[10] Q. Zhang, G. Huang and S. Li, "Mechanical Properties of DO_3 Based on First

Principles," *Crystals,* vol. 10, pp. 488, 2020.

[11] J. S. Blakemore, Solid State Physics, New York: Cambridge University Press, 1985.

[12] Libre Texts August 2020. [Online]. Available: https://chem.libretexts.org/Bookshelves/General_Chemistry/Book%3A_Chemistry_(Averill_and_Eldredge)/12%3A_Solids/12.1%3A_Crystalline_and_Amorphous_Solids. [Accessed 19 08 2020].

[13] B. Andrei A, U. Elena Gabriela and H. Y. Aboul-Enein, "X-Ray Diffraction: Instrumentation and Applications," *Critical Reviews in Analytical Chemistry,* vol. 45, pp. 289-299, 2015.

[14] L. Xing-Wu, S. Zhao, M. Yu, P. Qing, D. Albert K. and H. Chun-Fang, "Mössbauer Spectroscopy of Iron Carbides: From Prediction to Experimental Confirmation," *Scientific Reports,* vol. 6, pp. 26184, 2016.

[15] K. H. J. Buschow, Concise Encylopedia of Magnetic and Superconducting Materials, Netherlands: Elsevier, 2005.

[16] A. Houben, P. Muller, J. von Appen, H. Leuken, R. Niewa and R. Dronskowski, "Synthesis, Crystal Structure and Magnetic Properties of Semihard Itinerant Ferromagnet $RhFe_3N$," *Angewandte Chemie,* vol. 44, pp. 7212-7215, 2005.

[17] T. Takahashi, J. Burghaus, D. Music, R. Dronskowski and j. Schneider, "Elastic properties of γ′-Fe_4N probed by nano-identification and ab-initio calculation," *Acta Materialia,* vol. 60, pp. 2054-2060, 01 March 2012.

[18] A. Houben, V. Sepelak, K. Becker and R. Dronskowski, "Itinerant Ferromagnet $RhFe_3N$: Advanced Synthesis and Fe Mössbauer Analysis," *Chemistry of Materials,* vol. 21, pp. 784-788, 2009.

[19] T. Kaneko and T. Kanomata, Magnetic Properties of d-Elements, Alloys and Compounds Under Pressure, Berlin: Springer , 2014.

[20] J. Crangle and G. Goodman, "The Magnetization of Pure Iron and Nickel," *Proceedings of the Royal Society of London. Series A, Mathematical and Physical*

Sciences, vol. 321, pp. 477-491, 1971.

[21] P. D. Desai, "Thermodynamic Properties of Iron and Silicon," *Journal of Physical and Chemical Reference Data,* vol. 15, pp. 967-983, 1986.

[22] H. I. Faraoun, Y. D. Zhang, C. Esling and H. Aourang, "Crystalline, electronic, and magnetic structures of Fe_3C ,Fe_5C2 ,Fe_2C and from first principle calculation," Journal of Applied Physics, 2006.

[23] J. Haglund, G. Grimvall and T. Jarlborg, "Electronic structure, x-ray photoemission spectra, and transport properties of Fe_3C (cementite)," *Physical Review B,* vol. 44, pp. 2914-2919, 1991.

[24] M. Ron and Z. Mathalone, "Hyperfine Interactions of ^{57}Fe in Fe_3C," *Physical Review B,* vol. 4, pp. 774-777, 1971.

[25] O. Isnard, V. Pop and K. H. Buschow, "Magnetic properties of $Th_2Fe_{17}C_x$ compounds (x = 0,0.6,0.9,1.1)," *Journal of Applied Physics,* vol. 101, p. 103908, 2007.

[26] H. Bhadeshia, "Cementite," *International Materials Reviews,* vol. 65, pp. 1-27, 2019.

[27] J. Rausch and F. Kayser, "Elastic constants and electrical resistivity of Fe_3Si," *Journal of Applied Physics,* vol. 48, pp. 487-493, 2008.

[28] P. Gustavo A, Z. Pedro Mendoza, v. R. Marcela B. Fernandez and S. Francisco H, "Hyperfine field temperature dependence of Fe3Si from Mössbauer thermal scans," *Physica B: Condensed Matter,* vol. 354, pp. 369-372, 2004.

[29] T. Shinjo and Y. Nakamura, "Magnetic study of Fe_3Si and Fe_5Si_3 by Mössbauer Effect," *Journal of the Physical Society of Japan,* vol. 18, pp. 797-801, 1963.

[30] W. Hines, A. Menotti, J. Budnick, T. Burch, T. Litrenta, V. Niculescu and K. Raj, "Magnetization studies of binary and ternary alloys based on Fe_3Si," *Physical Review B,* vol. 13, pp. 4060-4068, 1976.

[31] Y. F. Liang, S. L. Shang, J. Wang, Y. Ye, J. P. Lin, G. L. Chen and Z. K. Liu, "First-principles calculations of phonon and thermodynamic properties of Fe-Si compounds," *Intermetallics,* vol. 19, pp. 1374-1384, 2011.

[32] C. A. R. Sa de Melo, "Theory of Itinerant Electron Magnetism," *Physics Today,* vol. 55, pp. 54, 2002.

[33] B. Cullity and S. Stock, Elements of X-Ray Diffraction, Notre Dame: Addison Wesley Publishing, 1956.

[34] V. K. Pecharsky and P. Y. Zavalij, Fundamentals of Powder Difraction and Structural Characterization of materials, New York: Springer, 2009.

[35] H. Brian, "ABC's of Electrochemistry-Material Characterization Technique: XRD," Russ College of Engineering and Technology, Ohio, 2011.

[36] A. Omar, Elementary Solid State Physics: Principles and Applications, New York: Addison-Wesley Publishing company, 1993.

[37] M. J. Flohr, "X-Ray Powder Diffraction," U.S Geological Survey, 1997.

[38] H. Stanjek and W. Hausler, "Basics of X-ray Diffraction," Kluwer Academic Publishers, Netherlands, 2004.

[39] T. Haber, M. Oehzelt and R. Resel, "The epitaxial sexiphenyl (001) monolayer on TiO_2 (110): A grazing incidence X-ray diffraction study," *Surface Science,* vol. 600, pp. 4645-4649, 2007.

[40] J. de Cloet, "Extracting the reaction kinetics of the formation of CIGS from in-situ X-ray diffraction measurements," Thesis, University of Twente, 2017.

[41] "LibreTexts," 5 June 2019. [Online]. Available: https://chem.libretexts.org/Bookshelves/Inorganic_Chemistry/Modules_and_Websites_(Inorganic_Chemistry)/Crystallography/X-rays/Structure_Factor. [Accessed 17 February 2020].

[42] "lumen learning," lumen, [Online]. Available: https://courses.lumenlearning.com/physics/chapter/24-2-production-of-electromagnetic-waves/. [Accessed 13 February 2020].

[43] Y. Wasenda, E. Matsubara and K. Shinoda, X-Ray Diffraction Crystallography, New York: Springer, 2011.

[44] A. R. West, Solid State Chemistry and its Applications, United Kingdom: John Wiley and Sons, 2014.

[45] B. Warren, X-ray Diffraction, Mineola, New York: Addison Wesley, 1990.

[46] S. C. Wallwork, "Introduction to the Calculation of Structure Factors," University College Cardiff Press, Wales, 2001.

[47] A. M. Adamska, "Variations of actinide magnetism in uranium-based hydrides and other selected systems," PhD Thesis, Charles University in Prague, 2011.

[48] M. Birkholz, "Thin Film Analysis by X-Ray Scattering," Wiley VCH, Weinheim, 2006.

[49] L. E. Smart, Solid State Chemistry: An Introduction, Taylor & Francis, 2005.

[50] T. Gibb and N. N. Greenwood, Mössbauer Spectroscopy, London: Chapman and Hall, 1971.

[51] E. Nordstrom, "Functional Materials Studied by Mossbauer Spectroscopy," PhD Thesis, Faculty of Science and Technology, Uppsala University, Sweden, 2001.

[52] M. Darby Dyar, "Mössbauer Spectroscopy of Earth and Planetary Materials," *Annual Review of Earth and Planetary Sciences*, vol. 34, pp. 83-125, 2006.

[53] P. Gutlich, R. Link and A. Trautwein, Mössbauer Spectroscopy and Transition Metal Chemistry., Berlin, 1978.

[54] M. Parker, "Coupling Nuclear Induced Phonon Propagation with Conversion Electron Mossbauer Spectroscopy," PhD Thesis, AFIT Scholar, 2015.

[55] P. Gutlich, "Mössbauer Spectroscopy - Principles and Applications," University of Mainz, Lecture Notes, Germany.

[56] R. L. Cohen and G. K. Wertheim, "Introduction to Mossbauer Spectroscopy," in *Experimental Methods in Mössbauer Spectroscopy*, New York, Academic Press, 1974, pp. 307-369.

[57] A. M. E. Alakrmi, "^{57}Fe Mössbauer Spectroscopic Study of the Spin-glass Transitions

in the Mixed Spinel Series MgFeNiTiO," PhD Thesis, 2010.

[58] Y. L. Chen and D. P. Yang, Mössbauer Effect in Lattice Dynamics: Experimental Techniques and Applications, John Wiley & Sons, 2007.

[59] M. Marszalek, "Mössbauer Spectroscopy: Basic Principles and Practical Guide to Exotic Mössbauer Isotopes," in *Spectroscopic Methods for Nanomaterials Characterization*, Elsevier, 2017, pp. 321-367.

[60] V. N. Adoons, "Magnetic Cluster Formation in Al_2O_3," University of KwaZulu-Natal,PhD Thesis, Durban, 2017.

[61] S. M. Qaim, "Recoil-free fractions of the 14.4 keV Mössbauer gamma line of ^{57}Fe in various host lattices," *Journal of Physics: Metal Physics*, vol. 1, pp. 320-327, 1970.

[62] F. Brent and E. K. (Editor), “Mössbauer Spectrometry”, in Characterization of Materials, New York: John Wiley, 2011.

[63] P. Gutlich, "Fifty years of Mössbauer Spectroscopy in Solid State Research - Remarkable Achievements, Future Perspectives," Germany, 2011.

[64] P. Gutlich, C. Schroder and W. Schunemann, "Mössbauer spectroscopy an indispensable tool in solid state research," *Spectrosopy Europe*, vol. 24, pp. 21-31, 2012.

[65] S. Devanarayanan, "Mössbauer Spectroscopy," in *Conference Paper*, University of Kerala, 2000.

[66] W. Dlamini, "^{57}Fe Mössbauer Studies of ^{57}Mn implanted III-Semiconductors InP and InAs.," School of Chemistry and Physics, University of KwaZulu-Natal, PhD Thesis, Durban, 2011.

[67] I. Obodovskiy, Radiation: Fundamentals, Applications, Risks, and Safety, Amsterdam: Elsevier, 2019.

[68] M. Parth, P. Shivani and K. Varun, "Synthesis and Application of Magnetic Nanomaterials for Memory Storage Devices," *International Journal of Advance Research*, vol. 1, 2013.

[69] H. S. Himel, "The Magnetic and Magnetocaloric Properties of Selected $Al_{1.2}Fe_2B_2$ Derivative Intermetallic Systems," Miami University, PhD Thesis, 2020.

[70] I. R. Harris and A. J. William, "Magnetic Materials," Encyclopedia of Life Support Systems: Material Science and Engineering, Birmingham, UK, 2000.

[71] S. V. Kailas, "Magnetic properties," Lecture Notes, Indian Institute of Science, Bangalore, 2004.

[72] A. Dharmavaram, "Magnetic properties of materials," [Online]. Available: https://www.academia.edu/31901935/MAGNETIC_PROPERTIES_OF_MATERIALS. [Accessed 29 June 2021].

[73] B. M. Sondezi, "Physical Properties of Ferromagnetic CeTX Compounds (T = Cu, Au; X = Si, Ge)," University of Johannesburg, PhD Thesis, Johannesburg, 2014.

[74] D. E. Gavrila, "Magnetic Properties of Materials," in *The physical bases of technical magnetism*, Bucharest, Notarom, 2014, pp. 1-22.

[75] J. M. Jules, "Magnetocaloric effect and critical behaviuor near the magnetic phase transition temperature in rare-earth compounds," MSc Dissertation, University of the Western Cape, 2018.

[76] B. O'Driscol, E. Ferre, C. Magee and C. Stevenson, "The Significance of Magnteic Fabric in Layered Mafic-Ultramafic Intrusion," Springer, Netherlands, 2015.

[77] F. Fiorillo, C. Appino and M. Pasquale, Hysteresis in Magnetic Materials, vol. 3, Italy: Elsevier, 2006, pp. 1-190.

[78] J. Karlsson and O. Söderström, "Review of Magnetic Materials Along With a Study of the Magnetic Stability and Solidity of Y_{40}," Thesis, Uppsala University, 2012.

[79] "www.tpub.com," [Online]. Available: http://chemical-biological.tpub.com/TM-1-1500-335-23/css/TM-1-1500-335-23_208.htm. [Accessed 07 August 2020].

[80] N. A. Spaldin, "Magnetic Materials: Fundamentals and Applications," *Physics Today*, vol. 56, pp. 62, 2011.

[81] E. Gopal, Specific heats at low temperatures, Bangalore: Planum Press, 1966.

[82] S. Kasap, J. Malek and R. Svododa, "Thermal Properties and Thermal Analysis: Fundamentals, Experimental Techniques and Applications.," in *Handbook of Electronic and Photonic Materials*, Canada, Springer, 2017, pp. 421-447.

[83] V. J. Juan and P. N. Quested, "Thermophysiscal properties," in *ASM Handbook*, Ohio, ASM international, 2008, pp. 468-481.

[84] M. Blackman, "The theory of the specific heat of solids," *Reports on Progress in Physics*, vol. 8, pp. 11-30, 1941.

[85] M. Waqas, A. Muhammad Sabieh and Z. Wasif, "Experimental determination of heat capacities and their correlation with theoretical predictions," *American Journal of Physics*, vol. 79, pp. 1099-1103, 2011.

[86] V. Varadarajan, "Specific heat capacity measurements on strongly correlated electron systems," PhD Thesis, University of Kentuky, 2009.

[87] C. Roder, S. Einfeldt, S. Figge and D. Hommel, "Temperature dependence of the thermal expansion of GaN," *Physical Review B*, vol. 72, pp. 085218, 2005.

[88] N. Phillips and R. Fisher, "Specific Heat of $YBa_2Cu_3O_7$," *Journal of Superconductivity and Novel Materials*, vol. 7, pp. 251-255, 1994.

[89] J. Missaghian, "Atomic interactions: Thermal, Magnetic and Transport Properties of Pd2TiIn," Thesis, University of California, 2011.

[90] P. Hofmann, Solid State Physics: An Introduction, Denmark: Wiley-VCH, 2015.

[91] W. M. Williams, "Synthesis, Crystal Growth, Magnetic and Transport Properties of Ln-M-X (Ln-Lanthanide, M-Transition Metal, X-IN,GA) Compounds," PhD Thesis, Mississippi Valley State University, 2006.

[92] Y. Shibuya, "The Electrical Resistivity of Cu-Ni Alloys and Mattheissen Rule," The research institute for iron, steel and other metals, Tohoku University, 1954.

[93] W. D. Callister and D. G. Rethwisch, Materials Science and Engineering: An

Introduction, New Jersey: John Wiley and Sons, 2010.

[94] A. Pandey, D. G. Quirinale, W. Jayasekara, A. Sapkota, M. G. Kim, R. S. Dhaka, Y. Lee and T. W. Heitmann, "Crystallogarphic, electronic, thermal and magnetic properties of single-crystal $SrCo_2As_2$," *Physical Review B,* vol. 88, pp. 014526, 2013.

[95] E. H. Sondheimer and A. H. Wilson, "The Theory of the Magneto-Resistance Effects in Metals," *Proceedings of the Royal Society of London. Series A, Mathematical and Physical Sciences,* vol. 190, pp. 435-455, 1948.

[96] "UKAM,com," UKAM Industrial Superhard Tools, 2009. [Online]. Available: https://www.ukam.com/diamond_wiresaw_lab.htm. [Accessed 20 July 2020].

[97] J. K. Snyder, "Analysis of Crystalline Phasesby X-Ray Diffraction Effect of Sample Grinding," PhD Thesis, University of North Dakota, 1992.

[98] S. P. Xhakaza, "Thermal Transport Properies of New Cubic Samarium Intermetallic Compounds," MSc Dissertation, University of Johannesburg, 2019.

[99] S. Bradbury and D. C. Joy, "Scanning electron microscope," 30 October 2019. [Online]. Available: https://www.britannica.com/technology/scanning-electron-microscope. [Accessed 26 October 26].

[100] S. Gajghate, "Introduction to Scanning Electron Microscope," August 2017. [Online]. Available: https://www.researchgate.net/publication/318819221_Introduction_of_Scanning_Electron_Microscope. [Accessed 03 02 2021].

[101] K. S. Subramanian, K. Raja and M. Kannan, "Scanning Electron Microscopy: Principle, Components and Applications," in *Textbook On Fundamentals & Applications Of Nanotechnology*, Daya Publishing House, 2018, pp. 81-92.

[102] Z. J. Istvan, "Scanning electron microscopy (SEM) analysis of tribofilms enhanced by fullerene-like nanoparticles," PhD Thesis, Stockholm University, Sweden, 2012.

[103] H. Y. Aboul-Enein, "X-Ray Diffraction: Instrumentation and Analysis," Taylor & Francis, London, 2015.

[104] C. L. Fleck, "Magnetism in Complex Cobaltates $Y_{(1=x)}Sr_{(x)}CoO_{(3-d)}$ ($0.7<x<0.95$) and $Ca_{(3)}Co_{(2)}O_{(6)}$," PhD Thesis, University of Warwick, 2011.

[105] D. Banerjee, "X-Ray Diffraction," July 2006. [Online]. Available: https://www.iitk.ac.in/che/pdf/resources/XRD-reading-material.pdf, [Accessed 17 March 2021].

[106] L. J. Poppe, V. F. Paskevich, J. C. Hathaway and D. S. Blackwood, "A Laboratory Manual for X-Ray Powder Diffraction," *US Geological Survey Open File Report*, vol. 1, 2001.

[107] "Bruker," Bruker corporation, 2020. [Online]. Available: https://www.bruker.com/terms-of-use.html. [Accessed 31 08 2020].

[108] K. A. Zak, R. Razali, W. Abd Majid and M. Darroudi, "Research Gate," July 2011. [Online]. Available: https://www.researchgate.net/figure/The-X-ray-diffraction-pattern-of-the-zinc-oxide-nanoparticles-prepared-by-the_fig3_215963338. [Accessed 17 February 2020].

[109] H. Rietveld, "Line profiles of neutron powder-diffraction peaks for structure refinement," *Acta Crystallographica*, vol. 22, pp. 151-152, 1967.

[110] H. Rietveld, "A profile refinement method for nuclear and magnetic structures," *Journal of Applied Crystallography*, vol. 2, pp. 65-71, 1969.

[111] J. Rodriguez-Carvajal, "Recent Advances in Magnetic Stucture Determination by Neutron Powder Diffraction," *Physica B: Condensed Matter*, vol. 192, pp. 55-69, 1993.

[112] D. M. Darby, A. David G, S. Martha. W, G. Christopher A and S. Elizabeth C, "Mossbauer Spectroscopy of Earth and Planetary Materials," Annual Review of Earth and Planetary Sciences, 2006.

[113] G. Principi, "The Mössbauer Effect," *Metals*, vol. 10, pp. 992, 2020.

[114] D. Freude, "Mössbauer Spectroscopy," in *Spectroscopy for Physicists*, August 2007. [Online]. Available: https://home.uni-leipzig.de/energy/freuse.html. [Accessed 25 June 2021].

[115] A. A. Boochakravarthy, "Study of Doped Magnetic Systems," MSc Dissertation, Arizona State University, 2018.

[116] Z. Hang, "Magnetic Characterization of Powder Samples from the Magnetocaloric compound Series $Mn_{5-x}Fe_xSi_3$," PhD Thesis, FH Aachen University of Applied Sciences, 2016.

[117] M. Healey, "Topology of the Magnetic Domains of a Co/Pt Multilayer with 16Å Cobalt Layers," PhD Thesis, Brigham Young University, 2016.

[118] A. H. S. Syed, "Vibrating Sample Magnetometery: Analysis and Construction," PhD Thesis, Department of Physics, Syed Babar Ali School of Science and Engineering, LUMS, 2013.

[119] Quantum Design Physical Property Measurement System, "Resistivity Option User's Manual," August 1999. [Online]. Available: https://web.njit.edu/~tyson/PPMS_Documents/PPMS_Manual/1076-100%20Rev.%20A0%20Resistivity.pdf. [Accessed 25 June 2020].

[120] Quantum Design Physical Property Measurement System, "Heat Capacity Option User's Manual," January 2004. [Online]. Available: https://www.mrl.ucsb.edu/sites/default/files/mrl_docs/instruments/hcapPPMS.pdf. [Accessed 25 June 2020].

[121] Y.-H. Ahn, B. Lee and K. Shin, "Structural Identification of Binary Tetrahydrofuran O_2 and 3-Hydroxytetrahydrofuran + O_2 Clathrate Hydrates by Rietveld Analysis with Direct Space Method," *Crystals,* vol. 8, pp. 328, 2018.

[122] H. P. Gunnlaugsson, "Spreadsheet Based Analysis of Mössbauer Spectra," *Hyperfine Interations,* vol. 237, pp. 79, 2016.

[123] D. Satula, "Structural and magnetic properties of Fe-Cr-Al alloys with DO_3-type structure," *Journal of Magnetism and Magnetic Materials,* vol. 169, pp. 240-252, 1997.

[124] A. Vasiliev, O. Volkova, I. Presniakov, A. Baranov and G. Demazeau, "Thermodynamic properties and neutron diffraction studies of silver ferrite $AgFeO_2$," *Journal of Physics: Condensed Matter,* vol. 22, pp. 16007, 2009.

[125] C. Antoniak, H. Herper, Y. Zhang, A. Warland, T. Kachel, F. Stromberg and B. Krumme, "Induced magnetism on silicon in Fe_3Si quasi-Heusler compound," *Physical Review B,* vol. 85, pp. 214432, 2012.

[126] D. Jiles, "Soft magnetic materials," in *Introduction to Magnetism and Magnetic Materials*, New York , Chapman and Hall Publishers, 2015, pp. 321-352.

[127] S. Dubiel and J. Zukrowski, "Site-resolved hyperfine and lattice dynamical properties of a singlecrystal Fe_3Si," *Journal of Alloys and Compounds,* vol. 817, pp. 152756, 2020.

[128] R. J. Goetsch, V. K. Anand, A. Pandey and D. C. Johnston, "Structural, thermal, magnetic and electronic transport properties of the $LaNi(Ge_{1-x}P_x)$ system," *Physical Review B,* vol. 85, pp. 054517, 2012.

[129] A. C. Jacko, J. O. Fjaerestad and B. J. Powell, "A unified explanation of the Kadowaki–Woods ratio in strongly correlated metals," *Nature Physics*, vol. 5, pp. 422-425, 2009.

[130] S. Wurmehl, G. H. Fecher and H. C. Kandpal, "Investigation of Co_2FeSi : The Heusler compound with highest Curie temperature," *Applied Physics Letters,* vol. 88, pp. 032503, 2006.

[131] D. J. Wagner, 2002. [Online]. Available: https://www.rpi.edu/dept/phys/ScIT/InformationStorage/magres/magnetism_b.html. [Accessed 16 09 2020].